Spring 1990

Ground-level atmospheric neutron flux measurements in the 10-170 MeV range

Renu Saxena
University of New Hampshire, Durham

Order Number 9027437

Ground-level atmospheric neutron flux measurements in the 10–170 MeV range

Saxena, Renu, Ph.D.

University of New Hampshire, 1990

U·M·I
300 N. Zeeb Rd.
Ann Arbor, MI 48106

GROUND LEVEL ATMOSPHERIC NEUTRON FLUX MEASUREMENTS IN THE 10-170 MEV RANGE

BY

RENU SAXENA

B.Sc., Delhi University, India, 1976

MS., Moscow State University, USSR, 1982

DISSERTATION

Submitted to the University of New Hampshire

in Partial Fulfillment of

the Requirements for the Degree of

Doctor of Philosophy

in

Physics

May, 1990

This dissertation has been examined and approved.

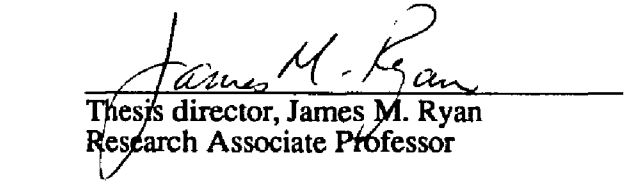

Thesis director, James M. Ryan
Research Associate Professor

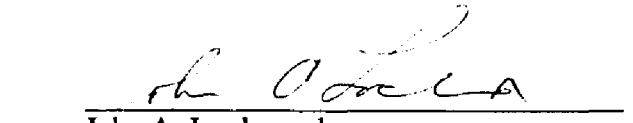

John A. Lockwood
Professor of Physics

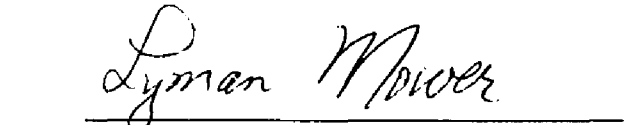

Lyman Mower
Professor of Physics

John R. Calarco
Professor of Physics

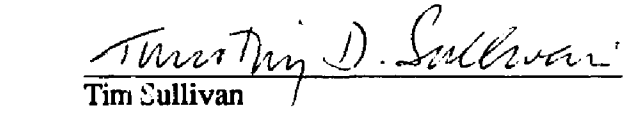

Tim Sullivan
Advisor Scientist, IBM Corporation.

March 26, 1990
Date

This thesis is dedicated to my parents Balkrishan Saxena and the late Sarla Saxena, who strongly believed in women's education and devoted their lives to it.

ACKNOWLEDGEMENTS

I would like to thank my thesis advisor Jim Ryan, for his infinite patience, kindness, and his ability to keep my spirits alive during all these years spent at UNH. His invaluable help towards the completion of this thesis and advice throughout the project is greatly appreciated. This experiment wouldn't have been possible without Jim Kish and Dave Schrier of Spectra Research Inc., who engineered and constructed the telescope. They always had time and patience to answer my dumb questions. Many hours spent by Jim Kish in fine tuning the telescope made my work much easier. Software developed by Dave Schrier for data acquisition and analysis proved to be invaluable. The pleasant company of Tim O'Gorman and Tim Sullivan from IBM corporation during the Indiana and Colorado trips made our stay quiet enjoyable. Subsequent discussions with them helped me a great deal in my work. I express my special thanks to Tim O'Gorman for providing me with his Monte Carlo simulation code. The telescope wouldn't have survived the ordeal of transportation to our different observation sites without the inventiveness of Stan Ellis.

I sincerely thank my thesis committee members Prof. Lockwood, Prof. Mower , Prof. Calarco, and Dr. Sullivan for being kind enough to look at my thesis at very short notice, and for their many helpful suggestions and corrections.

I would like to express my warmest thanks to Paul Vachon, Rita Freuder, Neil Schönwald, Matt Burke, John Labonte and Carmen Hefter for their help during different stages of my work here. I am extremely grateful to Lyn Preble for those last minute operations on my thesis, without which I could never have finished in time. Warmest thanks to Drs. George Simpson, Daniel Morris, Mark McConnell and Alanna Connors for their help during the course of this project. The cheerful environment at the Physics library

would not have been possible without the presence of Rebecca Marden and Dr. Deborah Watson.

The numerous discussions and arguments with my friends P. Sreekumar, Dipen Bhattacharaya and Mark Popecki made the stay here pleasant and enjoyable. Last but not least, I like to remember Amit Ghosh, who was always there for me.

I am thankful to IBM Corp. for providing the financial support through the Shared University Research Project under IBM(Burlington,VT)/UNH agreements: "A Study to Measure the Energy Spectrum of the Energetic Neutron Background at Sea Level," and "Ground Level Neutron Flux and Gamma Ray Measurements," for the completion of this project.

TABLE OF CONTENTS

List of Tables

List of Figures

ABSTRACT

GROUND LEVEL ATMOSPHERIC NEUTRON FLUX MEASUREMENTS IN THE 10-170 MEV RANGE

by

Renu Saxena

University of New Hampshire, May, 1990

We report the results of ground level neutron measurements in the energy range of 10 - 170 MeV by the neutron double scatter telescope developed at the University of New Hampshire. Measurements were carried out at different altitudes and latitudes for the first time using the same telescope, yielding better correction values for comparison of fluxes measured at different altitudes and latitudes. The mesurements were performed at four different locations in U.S.A: Leadville (3.1 km) and Boulder (1.66 km), Colorado in the rigidity range of 2.97 to 2.90 GV; Mt.Washington (1.85 km) and Durham (24 m), New Hampshire in the rigidity range of 1.43 to 1.61 GV.

The data from the zenith angle range of 15 to 45 degrees and from 10 to 170 MeV have been analysed. The zenith angle dependence of differential neutron flux in the total energy range was found to have a $\cos^n \theta$ dependence with $n = 2.6 \pm 0.2$. The integrated flux over the upper hemisphere shows a flat energy spectrum in the 10 - 60 MeV range and from 60 to 170 MeV falling of as $E^{-\alpha}$ with $\alpha = 0.6 \pm 0.1$. The e-folding depth was found

to be $\lambda = (123 \pm 29)$ g/cm^2 with the neutron count rate at sea level (Durham) being ($0.03 \pm$ 31%). We find that latitude correction applied to upper atmospheric neutrons is larger than that for ground level neutrons. Over the 1.56 GV range of these measurements the flux change after altitude correction is ~ 21%.

We also describe the instrument, the details of the measurements and the methods of analysis.

CHAPTER 1

INTRODUCTION

In 1912 Victor Franz Hess showed that earth is visited not only by distant light of the stars and sun, but also by an ionizing radiation, later called Cosmic Rays by R.A.Milikan in 1926. These primary cosmic rays interact with nuclei of atoms in atmospheric gases and produce a variety of secondary particles including neutrons. These secondary particles further on interact with other nuclei and so on, propagating deeper into the atmosphere. Particles produced in our atmosphere are called *secondary cosmic rays*. Neutrons observed in the atmosphere are mostly a part of secondary cosmic rays.

The flux of atmospheric neutrons varies with altitude and is a function of the neutron's energy and zenith angle. The flux also varies with geomagnetic latitude as described later on in this chapter due to different rigidities of the primary cosmic ray particle. Extensive work has been done to measure the neutron flux as a function of energy and zenith angle in the upper atmosphere (Lockwood et al., 1979; Preszler et al.,1976). At ground level, fast neutron measurements in the energy range of 10 - 100 MeV are few and do not agree with each other (Preszler et al., 1974). A knowledge of the ground level neutron flux is important in the studies of the soft errors of computer chips (Ziegler et al., 1979,1981a,1981b,1981c); in mineral age determination by its isotopic composition (Philips et al., 1986); in background studies for cold fusion (M.Gai et al., 1989); and in the background for gamma ray telescopes and particle detector experiments. The neutron energy spectrum is important in the study of nucleon propagation through the atmosphere and therefore to the response function of neutron monitors used to study the solar modulation of galactic cosmic rays (Preszler et al., 1974) and solar neutrons.

Bierman et al. (1951) proposed that neutrons may be produced by nuclear reactions in the sun, particulary during solar flare events, and some of these reach the earth. Later, Simpson (1963) suggested that anomalous, continuous fluxes of low energy protons (greater than 200 MeV) observed in space were a result of the decay of free neutrons emitted by sun. The flux and energy spectrum of *solar neutrons* to be expected at earth during a solar flare was calculated by Lingenfelter and Ramaty (1967). The solar neutrons were first observed by Chupp *et al.*, (1982,1983) in the energy range 40 MeV to 1.2 GeV.

The probability of observing neutrons from outside the solar system is not very high (Lockwood, 1973). A free neutron is not a stable particle and it decays with a mean life of ~ 898 s to a proton, electron and an antineutrino (Fig. 1-1:*beta decay* of neutron).

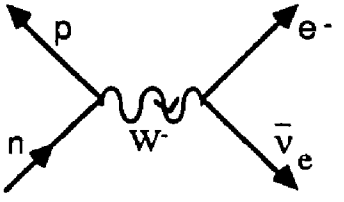

Fig. 1-1 : Neutron Decay

The time dilation of a neutron moving with velocity v relative to an observer is $t/t_0 = \gamma$, where t is the observed time, t_0 the mean life of the neutron in its rest frame, and $\gamma = (1-v^2/c^2)^{-1/2}$. As the sun is only 507 light seconds away, neutrons moving at half the speed of light, i.e. E ~ 132 MeV can reach earth before decaying. Neutrons from the closet star (4.5 light years) however would have to have energies > 10^{14} eV to reach the earth.

As atmospheric neutrons are produced by cosmic ray interaction with the atmosphere, any variations in cosmic ray intensity will also influence the neutron flux. A brief description of composition of particles incident at top of earth's atmosphere, their energy spectrum, and factors influencing their intensity (modulation) is given below.

1.1 Cosmic Rays

1.1.1 Primary Cosmic Rays

At the orbit of the earth primary cosmic rays are composed of ~ 98% nuclei, and ~ 2% electrons and positrons. In the energy range of 10^8 - 10^{10} eV/nucleon, where primary cosmic rays have the highest intensity at earth, the nuclear component consists of ~ 87% protons, ~12% alpha particles and ~ 1% for all the heavier nuclei from carbon to the actinides (Simpson, 1983). The energy spectrum of primary nuclei for $E > 10^{10}$ eV/nucleon follows a power law $J(E) = AE^{-\alpha}$, where J(E) is the differential flux, E the energy per nucleus and α the spectral index. For the energy range $10^{11} < E < 3 \times 10^{15}$ eV, the spectral index is ~ 2.6, and for $3 \times 10^{15} < E < 10^{20}$ eV, $\alpha \sim 3.2$ (Wolfendale, 1973). Nuclear composition of cosmic rays with $E > 10^{15}$ eV is still uncertain, with estimates ranging from pure iron to pure proton (Rochester and Turver, 1981). The electron spectrum at $5 < E < 300$ GeV is also given by a power law with $\alpha \sim 2.6$. The spectra of protons, nuclei and electrons are greatly affected by interplanetary and terrestrial magnetic fields at energies less than 10 GeV/nucleon (electron).

Cosmic rays of energies below ~ 10^{15} eV are believed to be of galactic origin and are confined to propagate in magnetic fields throughout our galaxy. As their motion is randomized by the irregular interstellar fields, such cosmic rays appear to be highly isotropic in the solar neighborhood (Simpson, 1982). Higher energy cosmic rays (above 10^{15} eV) are presumed to be of extragalactic origin as their gyroradii exceeds the scale size for containment in the disk of our galaxy (Burbidge, 1974). Also, the break in energy spectrum of cosmic rays at E ~ 10^{15} eV, where the spectrum becomes steeper, is also attributed to their different origin (Wolfendale, 1973).

The energy density of cosmic rays in our galaxy is ~ 1 eV/cm^3. For comparison, the energy density due to light of all stars in our galaxy near the earth is ~ 0.6 eV/cm^3 (Wolfendale, 1973).

1.1.2 Solar Cosmic Rays

During the active period of the the sun, i.e during solar flares, the sun often emits protons, electrons, and nuclei of very high energy in addition to the low energy plasma streams (solar wind). Such high energy particles are called *Solar Cosmic Rays*_(SCR). Particles with energies upto 20 GeV (flare of Feb.23,1956; Toptygin, 1985) have been detected. SCR contain mainly protons and helium nuclei. At E > 10 MeV/nucleon, the ratio of H to He is ~ 30 - 50 and the ratio of H to Nuclei(Z= 6 - 9) is ~ 2000. These ratios vary from flare to flare. This variation indicates different conditions for particle injection, acceleration and escape from generation regions into interplanetary space (Toptygin, 1985). The energy spectra of SCR can often be fit by power laws in energy ($E^{-\alpha}$) or in rigidity ($R^{-\beta}$). The electron spectra for $0.03 < E_e < 3.0$ MeV can often be fitted by a power law as well. The absence of one spectral index over the entire energy range can be due to many factors (mechanism of acceleration, energy loss, escape into the interplanetary space) affecting the spectrum formation of energetic solar particles.

1.1.3 Modulation of Galactic Cosmic Rays

The flux of galactic cosmic rays measured at the earth's orbit and consequently the flux of ground level neutrons experiences continuous variations of both a regular and stochastic character. These variations are a result of galactic, solar and terrestrial factors. Here, only solar and terrestrial effects are considered.

A. Solar Modulation

The solar modulation of galactic cosmic rays is greatest below a few hundred MeV due to their interaction with plasma streams, which are ejected from the sun and carry frozen-in magnetic fields in the form of regular (large-scale) fields and random magnetic inhomogeneities. Galactic cosmic ray particles meet these streams and are swept away by the interplanetary magnetic fields. Hence, the intensity of galactic particles inside the helio-

magnetosphere becomes smaller than in the galaxy. Solar modulation is divided into different types according to the time scale of the variations :

1) 11-year period variation associated with the 11-year cycle of solar activity and a 22-year variation related to solar magnetic polarity cycle;

2) 27-day periodicities related to solar rotation ;

3) Transient variation of a few days (Forbush decreases) ;

4) 24-hour variations related to rotation of the earth ;

5) Short-term variations(interplanetary scintillations)

Most of the earlier time variation studies were conducted using ground based instruments such as a neutron monitor or meson telescope. Hence, by measuring variations in the secondary cosmic rays, the variations in primary cosmic rays were inferred. The first observation of temporal changes in cosmic radiation at earth was made by Forbush (1938). He observed a sudden decrease in intensity (~ 5% for ground level neutrons) of cosmic ray radiation in about a day, the intensity then recovered back slowly in 5-7 days to its original level. Such decreases are now referred to as Forbush decreases. These decreases occur at random, with a tendency to be more frequent and to have larger amplitude during the increasing and maximum phase of the 11-year sunspot cycle. They occur when some magnetohydrodynamic disturbances (most probably shocks) travel near the Earth and sweep away cosmic rays for short time. Sporadic Forbush decreases are related to the occurrence of solar flares.

The cosmic ray intensity observed at the earth and in the earth's vicinity outside the magnetosphere exhibits a somewhat regular eleven year variation, approximately in antiphase with solar activity. Since the growth in the number of sunspots is accompanied by an increase in the number of high speed streams in interplanetary space, and consequently by an increase in the disturbances of the interplanetary magnetic field, it is assumed that this causes the 11-year cycle (Toptygin, 1985). The 11 year periodicity has also been observed in ^{14}C data at earth (Burchuladze et al.,1980). ^{14}C is produced when a

thermal neutron is absorbed by a ^{14}N atom. As secondary neutrons are produced by interaction of primary cosmic rays with the atmosphere, changes in the intensity of primary cosmic rays affect the intensity of the secondary products, i.e ^{14}C production. There is a decrease in its abundance during high solar activity. [Between 1645-1715 A.D., Maunder's Minimum, ^{14}C values were greater. During this time the 11-year solar cycle was weak, if present at all, but the 20-22 year cosmic ray modulation was present (Galli et al., 1987)].

B. Geomagnetic effect

The earth's magnetic field acts as a magnetic spectrometer for the cosmic rays, selecting them by rigidity. The rigidity R of a particle is defined as follows :

$$R = \frac{pc}{|ze|}$$

where, p is the particle's momentum in eV/c, z its charge and e is the charge of an electron. Rigidity is measured in volts. Particles of the same rigidity (R) have the same gyroradii (r) in a given magnetic field B :

$$r = \frac{R}{Bc}$$

The charged particle describes a helical trajectory around an earth's magnetic line of force. For certain directions and rigidities below a certain limit, the particle will follow a path which does not reach the atmosphere. Thus, part of the cosmic ray rigidity spectrum is cut off, and the limiting rigidity, called the *cutoff rigidity* R_c, is determined by the direction of observation and the position of the point of observation in the earth's magnetic field. For vertically incident particles, the *cutoff rigidity* R_c, at geomagnetic latitude, λ, is given by (Jory, 1956)

$$R(\lambda) = 14.9 \cos^4\lambda(1 + 0.018 \sin\lambda)^2 \ \text{GV} .$$

From this it can be seen that R_c increases towards the equator. R_c is not a fixed quantity for a given position, but varies due to secular changes in the magnetic field of the earth and also during magnetic storms.

There is an *East-West asymmetry* in the primary cosmic ray intensity, more particles coming from West than from East. This is due to a larger percentage of positive particles (98%) than negative in the cosmic radiation and interaction with magnetic field of Earth.

1.2 Interaction of Cosmic Rays with the Atmosphere

The composition and energy spectrum of cosmic rays changes as they propagate through the atmosphere due to a variety of interactions that take place along the particle's trajectories. Charged particles lose energy by ionization. Energetic hadrons (mostly primary protons) also lose additional energy due to interaction via strong forces with ^{14}N or ^{16}O nuclei in the atmosphere (~ 78% N_2, ~ 21% O_2), and produce a variety of secondary particles. In the early part of this century cosmic rays at ground level of earth were divided into two components; *hard* and *soft* , depending on the penetration power of the cosmic rays in 10 cm of lead. The *soft* component is absorbed near the surface while the *hard* component penetrates deeper. Later studies showed that the *soft* component consists of electrons and gamma rays, while nucleons, pions, muons and heavier particles comprise the *hard* component (Fig. 1-3).

1.2.1 Interaction of Primary Protons with Nuclei

An incident primary proton interacts with the nucleons in the nucleus because its de-Broglie wavelength is small compared to the distance between the nucleons (Longair, 1981). A proton passing through a nitrogen or oxygen nucleus will interact, on the average, with about $(15)^{1/3}$, i.e , 2.5 nucleons. A proton also undergoes multiple scattering inside the nucleus and produces secondary particles as shown in Fig.1-2 :

(i) A proton interacts with a nucleon producing pions of all types π^+,π^-,π°, strange particles and occasionally antinucleons.

(ii) The two nucleons and the pions in the laboratory frame possess a very high forward motion and emerge with high energy. In high energy collisions the pions are concentrated in a narrow cone, the size of which is related to the energy of primary particle.

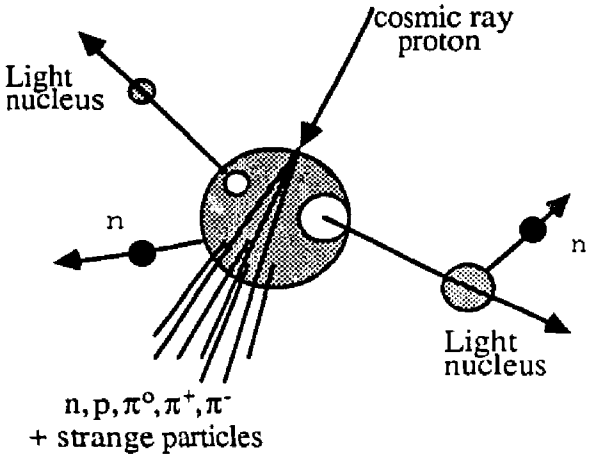

Fig.1-2 : A schematic diagram showing interaction of cosmic ray proton with a nucleus. (From M.S.Longair, *High Energy Astrophysics*, 1981, Cambridge University Press. Used with permission.)

(iii) Each of the secondary particles can initiate another collision inside the nucleus if the initial collision occured close to the front edge of the nucleus. Thus, a mini cascade can be initiated inside the nucleus.

(iv) One or two nucleons only participate in the nuclear reactions with the cosmic ray proton. They are generally removed from the nucleus, leaving it in a highly excited state.

Very often, several nuclear fragments evaporate from the nucleus. These are called *spallation fragments*. As most of the forward momentum is given to the nucleons tearing away from the nucleus, spallation fragments are emitted more or less isotropically in the laboratory frame. Neutrons also evaporate from the nucleus and from the spallation fragments.

The mean free path of a cosmic ray proton in the atmosphere is about 75 g/cm^2, based only on the interaction cross-section. The multiplicity of proton reactions produces a

wide distribution of particle energies and, therefore, the flux of protons falls off more slowly than one would expect from the mean free path (exp(- x/L), where L = 120 g/cm^2). The majority of the heavy nuclei of the primary radiation are fragmented in the first interaction which occurs at a higher altitude than for protons because of much shorter mean free path. For a nucleus with mass number A = 25, the mean free path is ~ 23 g/cm2 (Alkofer and Grieder, 1984).

Secondary nucleon and charged pions of sufficient energy continue to multiply in successive generations of nuclear collisions until the energy per particle drops below 1 GeV, which is the energy required for multiple pion production. This process is called a *nucleonic cascade* and it produces the *hadronic component* of secondary cosmic rays (Fig.1-3). Secondary protons lose energy by ionization and those with energy less than 1 GeV are brought to rest before reaching the earth's surface.

Charged pions are subject to decay (mean life time of 2.6 x 10^{-8} s in the rest frame) or strong interactions. The probability of an interaction depends on the density of the surrounding medium and the pion's energy. Those that decay give rise to muons, which easily penetrate the atmosphere:

$$\pi^+ \longrightarrow \mu^+ + \nu_\mu$$
$$\pi^- \longrightarrow \mu^- + \bar{\nu}_\mu .$$

Muons have a short mean lifetime of 2.2 x 10^{-6} s in the rest frame, but energetic muons survive to sea level due to time dilation and to a small cross section of interaction. These muons also contribute to the *hard component* of cosmic rays at ground level. Muons eventually decay into electrons or positrons with the emission of neutrinos:

$$\mu^+ \longrightarrow e^+ + \nu_e + \bar{\nu}_\mu$$
$$\mu^- \longrightarrow e^- + \bar{\nu}_e + \nu_\mu$$

Neutral pions have a mean lifetime of ~ 1.78×10^{-16} s decaying into two photons, each of energy 67.5 MeV in the pion rest frame:

$$\pi^0 \dashrightarrow 2\gamma \qquad (67.5 \text{ MeV}).$$

These photons can produce electron-positron pairs (besides the ones produced by the decay of muons) that undergo bremsstrahlung, which again produces electron-positron pairs, Compton scatter, and so on, forming the electron-photon electromagnetic cascade in the atmosphere (*soft component* of cosmic rays).

The flux of secondary particles increases with atmospheric depth (as measured from the top of the atmosphere), reaching a maximum at ~100 g/cm^2(~ 20 km from ground level), and then decreasing with depth due to absorption and decay processes. This maximum was first observed by George Pfotzer in 1935, and is called the *Pfotzer maximum*. The exact depth of the Pfotzer maximum depends on particle type and geomagnetic latitude.

1.2.2 Production of Atmospheric Neutrons

Secondary neutrons in the atmosphere are produced as described above by two kinds of reactions (Lockwood, 1973) :

1) Knock-on process,

2) Evaporation process.

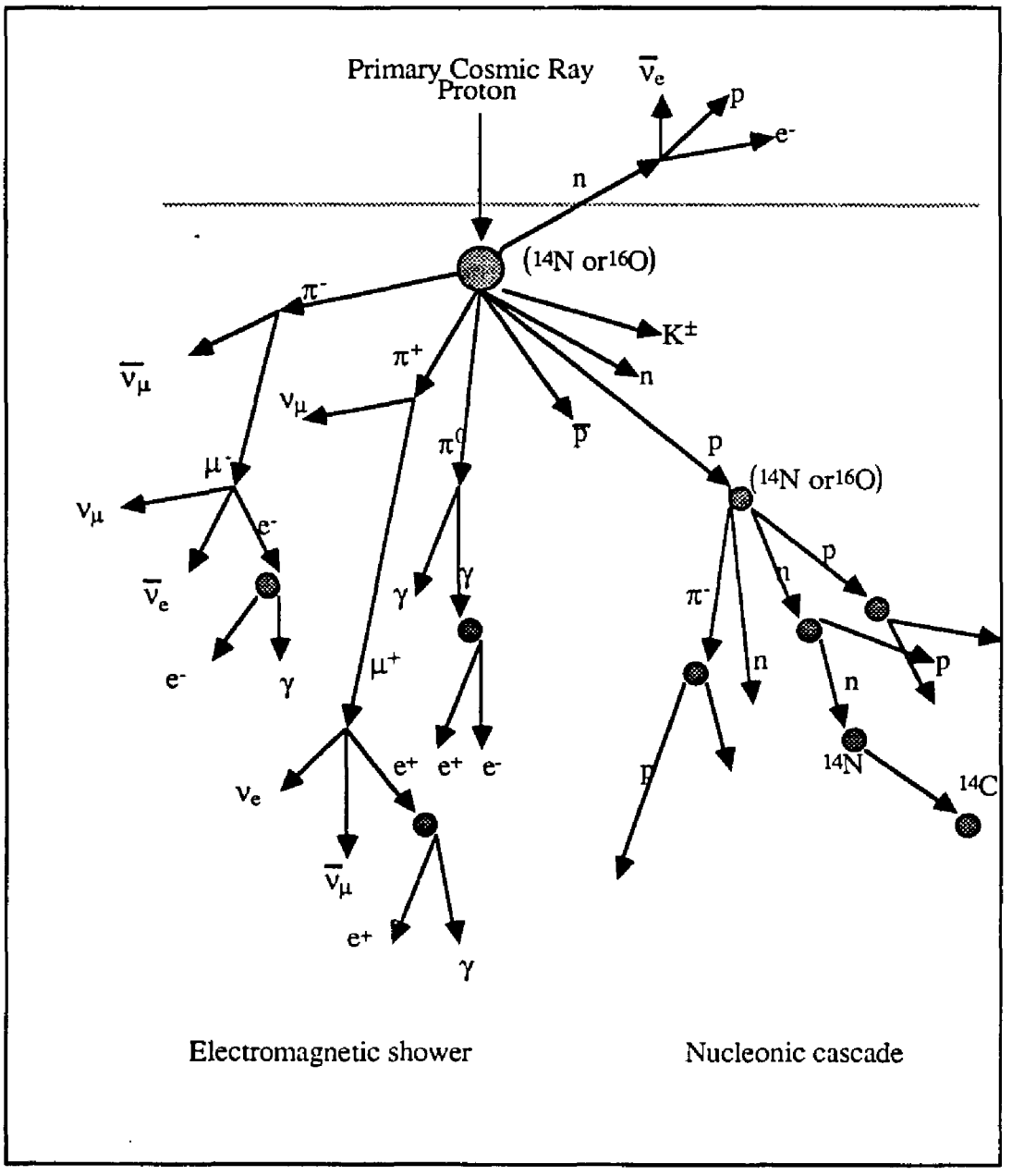

Fig. 1-3 : Interaction of primary cosmic rays with the atmosphere

Knock-on neutrons are produced when the incident hadron has a kinetic energy greater than the binding energy between nucleons in oxygen or nitrogen nuclei (> 10 MeV). The incident particle interacts with only a single nucleon or with a small number of nucleons, thus producing many fast nucleons with energies 10 - 50% of the incident energy, traveling approximately in the same direction as the incident particle. The Knock-on process is the principal source of high energy neutrons (E_n > 10 MeV). The *evaporation process* is the primary source of low energy neutrons, which comprises ~ 90% (Simpson, 1951) of the atmospheric neutron fluxes. When nitrogen or oxygen nuclei are excited to energies above 8 MeV (Hess, 1961), the most probable de-excitation mechanism is by evaporation of neutrons. These evaporated neutrons have a roughly Maxwellian energy distribution peaked at about 1 MeV and have isotropic angular distribution.

The neutrons produced lose their energy by elastic or inelastic scattering with nitrogen or oxygen nuclei until they are eventually lost by one of the following mechanisms (Hess et al., 1961, Lockwood, 1973) :

1) Thermalized neutrons are absorbed by ^{14}N nuclei to form ^{14}C and other isotopes ;
2) Fast albedo neutrons decay into protons and electrons, which then populate the Van Allen radiation belts;
3) Absorption by the earth, since fast neutrons will reach the earth before they decay;
4) High-energy inelastic collisions, involving charge exchange.

1.3 Atmospheric Neutron Measurements

Atmospheric fast neutrons were found for the first time in cosmic radiation when nuclear emulsions covered with paraffin were exposed to cosmic rays in the stratosphere (Rumbaugh and Locher, 1936). In nuclear emulsions the length of the track gives a

measure of the particle energy and the density of the track distinguishes particles of different dE/dx. The number of tracks of a given type gives an indication of the particle flux. Fast neutrons are detected by measuring the recoil proton tracks in the emulsion.

After the discovery of Van Allen Radiation belts around the earth in 1958, the CRAND (Cosmic Ray Albedo Neutron Decay) theory was proposed as the source for trapped charged particles in the belts (Singer, 1958). Albedo fast neutron flux observations in the upper atmosphere supported the CRAND theory (Preszler et al.,1972,1974,1976; Kanbach et al., 1974; Lockwood et al., 1976,1979; Bhatt, 1976,1983,1986; Ait-Ouamer et al., 1988). The reviews of atmospheric neutron measurements by Lockwood (1973) and by White (1973) describe the theory and measurements of albedo neutron flux.

However, ground level neutron flux measurements were not as extensive as the neutron flux measurements in upper atmosphere because of the low flux of neutrons at ground level as compared to the stratosphere, hence the need for long accumulation times. Neutron monitors located at different geographical locations on earth measure the solar modulation of cosmic rays continuously by observing the changes produced in the neutron intensity (Lockwood and Calawa, 1957; Webber and Lockwood, 1988). In a neutron monitor, fast neutrons are slowed down by a moderator and the slow neutrons produced are then detected by a boron-lined proportional counter. However, neutron monitors do not measure the energy spectrum nor the atmospheric flux of neutrons.

One of the first measurements of the ground level energy spectrum of neutrons was made by Hess et al. (1959) using different omnidirectional counters for different energy ranges (thermal to 500 MeV). They observed for the first time the presence of a peak near 1 MeV, which was attributed to the evaporation neutrons. From thermal to 100 keV, the energy spectrum varied as 1/E and from 1 MeV to 500 MeV as $E^{-1.5}$. The spectrum was extended beyond 500 MeV using values calculated on the assumption that above the geomagnetic cutoff the neutron spectral shape at sea level is the same as that of proton spectrum (Hess et al., 1961). The shape of the spectrum is the same at an altitude of

200g/cm^2 as it is at sea-level. The altitude atttenuation coefficent was found to be 155g/cm^2.

Miyake et al. (1957a) used a cloud chamber filled with hydrogen gas to measure neutrons in the energy range of 1 MeV to 15 MeV. They found the differential neutron flux to vary as (1.2±40%) × 10^{-3} × $E^{-1.25\pm0.10}$ cm^{-2} sec^{-1} sr^{-1} MeV^{-1}. The angular distribution was found to be isotropic in this low energy range. To measure neutrons in the 10 MeV to 100 MeV range Miyake et al. (1957b) used a nitrogen-filled high pressure cloud chamber at an altitude of 760 g/cm^2 and latitude of 25^o N. The vertical intensity of neutrons in this energy range was estimated to be (2.4± 40%) ×10^{-3} · $E^{-1.4}$ cm^{-2} s^{-1} sr^{-1} MeV^{-1}. The angular distribution varied as $\cos^n \theta$, with n = 0 for E < 10 MeV and reached n = 5 at 1 GeV.

Tajima et al.(1967) measured ground level neutrons in the energy range from 1 MeV to 10 MeV at 25^{o}N geomagnetic latitude using a liquid scintillator with pulse shape discrimination to select the proton recoils. They also found the neutron energy spectrum to vary with altitude. Their data could be fitted by $0.30 \cdot \exp(-h/217.4) \cdot E^{-(0.77 + h/1000)}$, where h is altitude in g/cm^2. The neutron attenuation length in the atmosphere for any given energy was found to be 158.7 g/cm^2. Their results agree with measurements of Hess after correcting for the latitude factor.

Hughes and Marsden (1966), using neutron monitor data, extended the Hess spectrum above 200 MeV by adjusting the slope until it approached a value of 2.6 at around 10 GeV. This change is a consequence of the fact that the spectral index for protons in the energy range 10-100 GeV at sea level is ~ 2.6 (Brooke and Wolfendale, 1964) instead of 2.15 as taken by Hess et al.(1959). It is expected that at such high energies the proton and neutron spectra will be similar. Hughes and Marsden used a iterative procedure to optimize the shape of the spectrum by obtaining the best fit between the multiplicity spectrum observed with their neutron monitor and that predicted from the chosen spectral

shape. This method is very insensitive for the calculation of spectral index and flux values of atmospheric neutrons.

Ashton et al.(1971) used a plastic scintillator telescope with Cerenkov counters to measure the neutron spectrum of downward moving neutrons in the energy range of 0.4 to 1.2 GeV. The neutron kinetic energy was measured by the charge exchange reaction : n+p --> p + n. Their spectrum corresponds well with the Hughes and Marsden spectrum described above. In the energy range 50 - 1000 GeV, Ashton et al.(1969) found the spectral index to be 2.95 ± 0.10 and the attenuation length of nucleons of average energy 230 GeV in atmosphere to be 127 ± 15 g/cm^2 .

Heidbreder et al. (1971) measured the ground level neutron spectrum from 80 to 300 MeV using double elastic scattering of neutrons in a polyethlene radiator spark chamber detector. Their energy spectrum agrees with that of Hess in shape but the flux is lower by a factor of 3. At 100 MeV the spectrum of Miyake et al. (1957) agrees with this spectrum.

Armstrong et al. (1973) using a Monte Carlo method calculated the ground level neutron spectrum from thermal energies to several GeV. For neutron energies less than 10 MeV and greater than 300 MeV, their spectrum agrees both in shape and value with the spectrum of Hess et al. (1959). In the 10-100 MeV range their spectrum is flatter.

Preszler et al.(1974) measured ground level neutrons in the 10-100 MeV range using a double-scatter neutron telescope. Time of flight was used to discriminate between upward and downward moving events and gammas from neutrons. They obtained a flat spectrum from 10 to 100 MeV and their flux values and spectral shape agreed with theoretical spectrum of Armstrong et al.(1973). They also obtained the angular distribution, which showed a maximum near zenith for downward-moving neutrons . Upward-moving neutrons also have a maximum near the vertical.

The Monte Carlo calculation of Flückiger et al.(1976,1977) of atmospherically produced neutrons in the energy range of 50 MeV - 100 GeV were done for sea-level and

for 650 g/cm^2. The flux and spectral shape agrees with the measurements of Ashton et al.(1971) and with the derived neutron spectrum of Hughes and Marsden (1966) for E > 700 MeV. This confirms the statement that the flux values of Hess et al.(1959) at high energies were overestimated. For E < 700 MeV their spectrum agrees with the spectrum of Heidbreder et al.(1971). For energies greater than 200 MeV, their spectrum agrees with the theoretical spectra of Armstrong et al.(1973) and of Light et al.(1973), but for 50 to 200 MeV, their spectrum is much flatter and lower by a factor of 10. The associated neutron attenuation length in the atmosphere was calculated to be 128 g/cm^2.

Therefore, in the energy range of 10 - 100 MeV, results of different measurements both theoretical and experimental are not in complete agreement. This energy range is crucial for estimating the soft error in computer microchips (Ziegler and Lanford, 1979). The purpose of our studies was to measure the neutron spectrum in the 10 - 170 MeV range both as a function of energy and zenith angle. By using same telescope at different altitudes and latitudes, we can get better values for the neutron attenuation length in the atmosphere and the latitude factor for the ground level neutron flux.

CHAPTER 2

INTERACTION OF NEUTRONS WITH MATTER AND SCINTILLATOR PHYSICS

As a neutron is an uncharged particle, it cannot interact with atomic orbital electrons through coulomb forces. Neutrons readily penetrate the electron cloud and interact with the nucleus through strong forces, which come into play only at a distance ~1 fm from nucleus. For this reason this particle eluded scientists until 1932 when Chadwick proposed a neutral particle of mass similar to a proton to explain the penetrating radiation coming from the bombardment of light elements such as Li, Be and B by alpha particles.

Neutrons are detected by measuring energetic charged particles, e.g., protons and alpha particles, which are products of reactions between the neutron and the nucleus. A general reaction of a neutron with a nucleus ${}^{A}_{z}X$ can be represented as :

$$n + {}^{A}_{z}X \text{ -----> } \left({}^{A+1}_{z}X\right)^{*} \text{ ----> } \left\{ \begin{array}{l} \text{Scattering (elastic or inelastic)} \\ \text{Absorption} \end{array} \right\}$$

where $\left({}^{A+1}_{z}X\right)^{*}$ denotes the compound nucleus in an excited state, which decays either by scattering or by absorption in 10^{-20} to 10^{-12} s. The probability of neutron interaction depends strongly on the neutron's energy. Neutrons with energies less than 0.5 eV are called *slow neutrons*. The energy 0.5 eV is chosen because near this energy there is a abrupt drop in the neutron absorption cross section for ^{113}Cd (Knoll,1989), while at 0.2 eV there is a large resonance of ~ 3000 barns. Thermal neutrons at room temperature have an average energy of 0.025 eV. Neutrons with energies higher than 1 keV are called *fast neutrons* (Marion and Fowler, 1960).

2.1 Slow Neutron Interactions

2.1.1 Elastic Scattering

In *elastic scattering*, the total kinetic energy of the two colliding particles is conserved but redistributed between the scattered neutron and the recoil nucleus. The recoil nucleus can be detected via ionization if the original neutron is sufficiently energetic.

2.1.2 Absorption

The neutron can be absorbed by a nucleus which may then decay along more than one path. Neutron capture by light nuclei often leads to the emission of heavy charged particles. Two of the most important reactions used for detection of slow neutrons are :

$$^{10}B + n \; \text{-->} \left\{ \begin{array}{l} ^{7}Li \quad + \alpha \; + 2.79 \text{ MeV} \\ ^{7}Li^{*} + \alpha \; + 2.31 \text{ MeV} \end{array} \right\}$$

$$^{6}Li + n \; \text{-->} \; ^{3}H \; + \alpha \; + \; 4.78 \text{ MeV.}$$

For neutron absorption on B, 93.7% of the resultant disintegrations go to the excited state $^{7}Li^{*}$, which promptly de-excites by emitting a 0.48 MeV gamma ray. With increasing neutron energy, the probability of this reaction decreases, compared to others. The reaction product energies are strictly determined by the ratio of the masses.

With heavy nuclei most of the excess binding energy (~ 8 MeV) following slow neutron absorption can be emitted as γ radiation (radiative capture), with a new isotope being formed which may be radioactive. If the new isotope is radioactive, it normally decays by the emission of β^{-} or β^{+} rays, often accompanied by additional gamma rays. Absorption of a neutron by very heavy nuclei ($Z > 90$) can lead to fission. Nuclei such as ^{233}U, ^{235}U and ^{239}Pu, undergo fission following thermal neutron capture, while others require fast neutrons of a few MeV energy. The energy release is typically about 160 MeV.

2.2 Fast Neutron Interactions

2.2.1 Elastic Scattering

This is an important reaction for measuring fast neutrons, as recoil nuclei can acquire significant kinetic energy from the scattering process. Neutrons are elastically scattered by all nuclei, but the energy transfer to the recoil nucleus is maximum for hydrogen. Therefore, hydrogen is the most efficient moderator for fast neutrons. This reaction is described in section (2.3.1 below). Neutron monitors have paraffin shielding to slow down the fast neutrons, with the resultant slow neutrons being detected by the ^{10}B reaction described above.

2.2.2 Inelastic Scattering

In inelastic scattering, some of the incident neutron kinetic energy excites the recoil nucleus, which de-excites by emitting gamma rays and/or other particles. This reaction becomes important for fast neutrons. Inelastic scattering plays an important role in high energy neutron shielding but creates unwanted noise in neutron spectrometers. Inelastic scattering of neutrons with carbon nuclei ^{12}C is described in detail in section (2.3.2 below).

2.2.3 Absorption

In the absorption of fast neutrons, as for slow neutrons, the neutron disappears but one or more other particles are produced. Absorption includes both capture and fission reactions. Typical fast neutron absorption reactions are:

$n + {}^{A}_{Z}X \rightarrow {}^{A}_{Z-1}Y + p$	(n,p) reaction - charge exchange
$n + {}^{A}_{Z}X \rightarrow {}^{A-3}_{Z-2}Y + \alpha$	(n,α) reaction - absorption with α-emission
$n + {}^{A}_{Z}X \rightarrow {}^{A-1}_{Z}X + 2n$	(n,2n) reaction - absorption with neutron evaporation
$n + {}^{A}_{Z}X \rightarrow {}^{A+1}_{Z}X + \gamma$	(n,γ) reaction - absorption with γ-de-excitation

$n + {}^{A}_{z}X \rightarrow {}^{A_1}_{z_1}Y_1 + {}^{A_2}_{z_2}Y_2 + n + n + ..$ fission

2.2.4 Spallation

Knock-on nucleons and spallation fragments are produced when high energy fast neutrons interact with the nucleus. Spallation fragments are nuclear fragments evaporated from the nucleus. These fragments are emitted in the frame of the nucleus which is not given much forward momentum in the nuclear collision, virtually all of it having gone into tearing the nucleons apart.Therefore, the spallation fragments are emitted isotropically in the the laboratory frame. Neutrons can evaporate from the residual nucleus and also from spallation fragments (Longair, 1981). This reaction is also described in section (1.2.1).

2.3 Interaction of Neutrons With Organic Scintillator

Organic scintillators are frequently used to measure fast neutrons in the energy range of 10 - 200 MeV. They consist basically of H and C atoms, the proportion of H to C atoms varies from scintillator to scintillator.

2.3.1 Interaction of Neutrons with Protons

Below ~ 300 MeV, the predominant mode of interaction between neutrons and protons is elastic scattering. The capture cross section for a neutron by a proton, forming deuterium, is 0.333 b at thermal energies (Cokinos et al., 1977), while the total cross section at the same energy is ~ 58 b (Mclane *et al.*, 1988). The reaction is described as

$$n + p \rightarrow d + \gamma \qquad (E_\gamma = 2.2 \text{ MeV}).$$

For fast neutrons, the capture cross section falls to ~ 31.6 μb at 14.4 MeV (Cerineo et al., 1961), while the total cross section is ~ 0.7 b. Inelastic scattering can occur if the incident neutron energy is higher than the rest mass of a pion, i.e. ~ 140 MeV. At 30 GeV the cross section for inelastic scattering 35 mb (Bózoki et al., 1962).

A. (n,p) Elastic Scattering

In the laboratory frame, incident neutrons with kinetic energy E_n elastically scatter off a proton at rest through the exchange of a pion. The recoil proton acquires some kinetic energy (E_p) and the neutron recoils at a scatter angle θ with kinetic energy E_n' (Fig. 2.1).

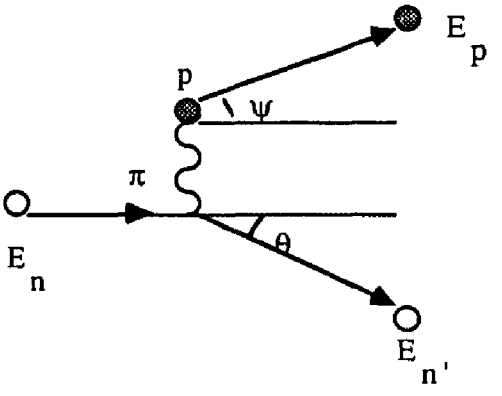

Fig. 2-1 : (n,p) Elastic Scattering.

Relativistic kinematics for (n,p) elastic scattering must be used for high energy neutrons, as at neutron energies of ~ 100 MeV the difference between the nonrelativistic and the relativistic case is ~ 5% .The total kinetic energy of a incident neutron is given as :

$$E_n = E_p + E_{n'} \tag{2.1}$$

and the scatter angles of the neutron and recoil proton are :

$$\tan^2 \theta = \frac{2}{(1+\gamma)}\left(\frac{E_p}{E_{n'}}\right) \tag{2.2}$$

$$\tan^2 \psi = \frac{2}{(1+\gamma)}\left(\frac{E_{n'}}{E_p}\right) \tag{2.3}$$

where, $\gamma = (1-\beta^2)^{-1/2}$. In the relativistic case $(\theta + \psi) < \pi/2$ and only when γ approaches one (i.e nonrelativistic) is the sum of the angles equal to $\pi/2$.

Measuring the energy of the recoil proton (E_p) and the scattered neutron (E_n'), allows one to calculate the incident neutron kinetic energy (E_n) and scatter angles θ and ψ.

The velocity vectors of the incident and scattered neutron define the scattering plane. The recoil proton also lies in the same plane. .

B. Differential cross section for (n,p) scattering

Experimental data for (n,p) scattering show that the angular distribution is isotropic below 14 MeV in center-of-mass system with a parabolic shape at higher energies. At much higher energies a pronounced peak in the backward direction is present, which cannot be understood by an ordinary potential that does not change the nature of the proton and the neutron. It can be explained by an exchange force, where, through the exchange of a charged pion (Fig. 2-2), the forward moving neutron becomes a proton and the recoil proton becomes a neutron. The result after scattering is a backward moving neutron (Fraunfelder and Henley, 1974) (Fig. 2-2).

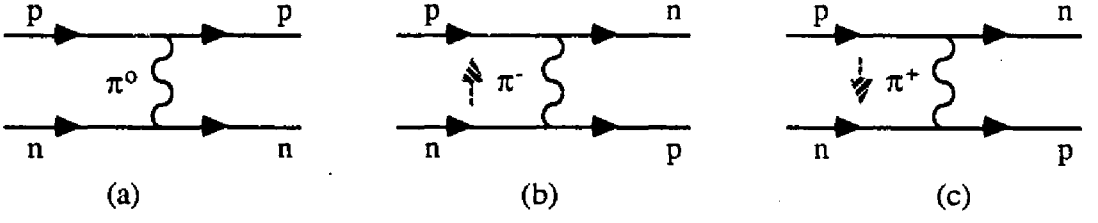

Fig. 2-2: Feynman diagrams illustrating n,p scattering by pion exchange

Existing data of differential (n,p) scattering can be fitted by a sum of five Legendre polynomials (Anghinolfi et al., 1979) :

$$\frac{d\sigma\left(E_n,\theta\right)}{d\Omega} = \sum_{l=0}^{4} A_l P_l\left(\cos\theta_{c.m}\right),$$

where, the $A_{l(}E_n)$ are fitting parameters.

C. Total cross section for (n,p) scattering.

The total scattering cross section at energy E_n is :

$$\sigma_t(E_n) = \int_{\Omega} \frac{d\sigma(E_n,\theta)}{d\Omega} d\Omega$$

where $d\sigma(E_n,\theta)/d\Omega$ is the differential cross section for (n,p) elastic scattering. The total cross section for (n,p) scattering can be described by the semi-empirical formulas of J.Gammel ($E_n < 71$ Mev) and N.Metropolis ($E_n > 71$ Mev), where E_n is in units of MeV, σ in barns for Gammel's formula and mb for Metropolis's formula (Rindi et al., 1970).

(i) Gammel's Formula ($1 < E_n < 71$ Mev)

$$\sigma_t(E_n) = 3\pi[\ 1.206E_n+(-1.86+0.09415E_n+0.0001307E_n^2)^2\ ]^{-1} + \pi[\ 1.206E_n+(0.4223 + 0.13E_n)^2\ ]^{-1}$$

(ii) Metropolis's Formula ($E_n > 71$ Mev)

$$\sigma_t(E_n) = \frac{34.10}{\beta^2} - \frac{82.2}{\beta} + 82.2$$

where $\beta = v/c$.

2.3.2 Interaction of Neutrons with Carbon (^{12}C)

A. Elastic Scattering

In the nonrelativistic case, the scattered energies of a neutron and a recoil nucleus are :

$$E_{n'} = E_n\left(1 - \frac{4A}{(1+A)^2}\cos^2\psi\right) \qquad (2.5)$$

$$E_C = \frac{4A\cos^2\psi}{(1+A)^2} E_n \qquad (2.6)$$

where A is the mass ratio of the target nucleus to the neutron, and ψ is the scattered angle of the recoil nucleus. For (n,C) scattering, A = 12. The maximum energy which can be given to the carbon nucleus occurs during a head-on collision (ψ = 0), for which the energy of the recoiling carbon is $E_C(max) \sim 0.28E_n$. Therefore, the scattered neutron can have energies ranging from E_n to $0.72E_n$.

The differential cross section for (n,C) elastic scattering for $2 < E_n < 10$ MeV is given by the following expression :

$$\frac{d\sigma(E_n)}{d\Omega} = \sum_{l=0}^{4} A_l P_l(\cos\theta_{c.m}) .$$

where,the A_l are experimental fitting parameters (Anghinolfi et al.,1979). Values of the A_l vary as a function of neutron energy due to the presence of resonances. (Below 2 MeV, the cross section is isotropic.)

Above 10 MeV the cross section is described by

$$\frac{d\sigma(E_n)}{d\Omega} = \sum_{l=0}^{4} A_l P_l(\cos\theta_{c.m}) + A_5 \exp[A_6(1 - \cos\theta_{c.m})] .$$

B. Nonelastic Scattering

During nonelastic scattering, part of the incident kinetic energy of a neutron is given to the target nucleus as excitation energy, with the target nucleus de-exciting either by emission of gamma rays and/or other particles. Some of the reaction channels are listed below (Nakayama et al.,1981) :

(i) $^{12}C(n, n'\gamma)^{12}C$ Q = -4.43 MeV (inelastic scatter)

(ii) $^{12}C(n, \alpha)^{9}Be$	Q = -5.71 MeV	(absorption with α emission)
(iii) $^{12}C(n, n'3\alpha)$	Q = -7.28 MeV	(absorption with carbon breakup)
(iv) $^{12}C(n, np)^{11}B$	Q = -15.96 MeV	(spallation)
(v) $^{12}C(n, 2n)^{11}C$	Q = -20.30 MeV	(spallation).

The energy and angular distributions of these channels are discussed in detail by Anghinolfi et al.(1979) and Nakayama et al.(1981). The second channel does not have a scattered neutron and hence does not contribute to the operation of a double scatter telescope, but it is an important channel for a single detector.

2.4 Scintillator Physics

A scintillator is a material in which energy deposited by a charged particle is converted into photons of visible wavelengths. Neutral particles such as neutrons or gamma rays also deposit energy in scintillators, but only by scattering off charged particles, (e.g., protons and electrons) which then generate electron-hole pairs or excited molecules in the scintillator.

Scintillators can be either inorganic or organic. Inorganic scintillators are ionic crystals doped with activator centers. NaI(Tl) is a common inorganic scintillator used in gamma ray spectroscopy where the doping element is Tl. The mechanism of scintillation differs for inorganic and organic scintillators. In inorganic scintillators, electron-hole pairs produced due to ionization diffuse through the lattice and are captured by the impurity centers. Recombination produces an excited center, which emits light upon its return to the ground state. Only a fraction of kinetic energy lost by a charged particle is converted into fluorescent energy, the rest is dissipated nonradiatively in the form of lattice vibrations or heat. The light output of inorganic scintillators is generally larger than that of organic scintillators (e.g., NaI(Tl) (7%) vs. Anthracene (3.5%)), but inorganic scintillators are

usually slower than organic scintillators (~ μs vs. few ns). Some inorganic crystals are also hydroscopic and will deteriorate if exposed to water vapor.

2.4.1 Organic Scintillators

Organic scintillators are either crystal, liquid or plastic. They can be either unitary (consisting of only one fluorescent aromatic compound) or binary.(consisting of solute and a solvent). Light output of all organic scintillators is generally compared to that of Anthracene, which is taken to be 100%.

Anthracene is a pure aromatic crystal, and has a high fluorescence quantum yield, but in a crystal, the ionization quenching coefficient depends on the direction of the ionizing particle relative to the crystallographic axes which gives rise to anisotropic scintillation. In a liquid or polymer, the scintillation response is isotropic, but pure liquid or polymers have poor quantum yields. Better performance is obtained if the organic scintillator used consists of an aromatic solvent (liquid or polymer) and high fluorescent yield solute. Liquid scintillators often have xylene, toluene or mineral oil as a solvent with PPO (2,5-Diphenyl oxazole) as a solute. Polystyrene or polyvinyl toluene are the solvents most often used for plastic scintillators. The efficiency of a scintillator-based detection system is increased by adding a secondary solute (wavelength shifter) at about 1% the concentration of the primary solute. The purpose of wavelength shifter is to lower the self-absorption of the light emission and to produce an output that is well matched to the spectral characteristics of the photomultiplier tube (PMT). POPOP (2,2'-P-Phenylenehis-(5-Phenyloxazole) is the commonly used wavelength shifter.

The passage of a charged particle through a scintillator produces ionization, giving rise to excitation in molecules. A small percentage of these excited molecules de-excite by radiation. The emitted light is not self-absorbed because of the π-electronic structure of the molecules (vibrational molecular levels e.g. S_{21},S_{22} etc.). The energy can be absorbed by exciting the electron into any one of the number of vibrational states of the first singlet

excited state, e.g., S_{10},S_{11},S_{12}. Any state with excess vibrational energy (S_{11},S_{12},..) is not in equilibrium with its neighbors, so it loses that excess vibrational energy in the form of heat dropping to the ground electronic state S_1. Emission (fluorescence) occurs from S_1 to any one of the vibrational states of the ground singlet level e.g. S_{00},S_{01},S_{02} (Fig. 2-3).

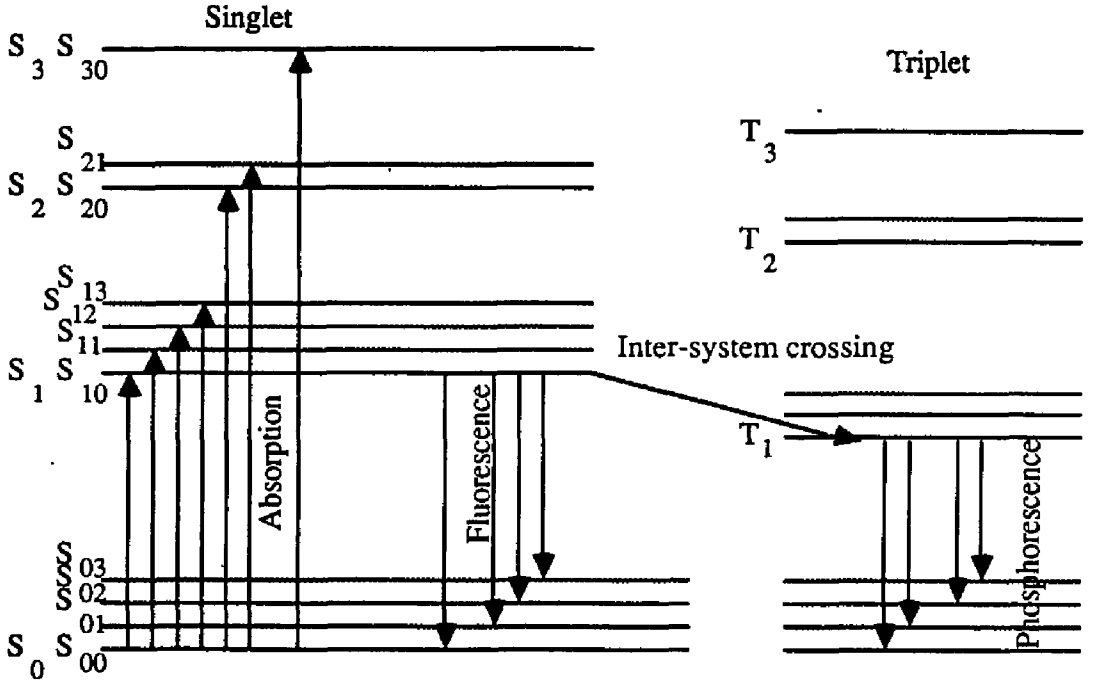

Fig. 2-3 Energy levels of an organic molecule with π−electron structure.(From J.B.Birks, *The Theory and Practice of Scintillation Counting*. Copyright 1964 by Pergamon Press, Ltd. Used with permission.)

There are two components of scintillation decay (Birks,1964), a fast component (1-10 ns) and/or slow component (~1μs). The fast component is produced by the transition from the first singlet excited state to the singlet ground state (fluorescence) with the probability of decay being exponential, $I = I_o e^{-t/\tau}$ (τ = 1-10 ns). Besides singlet states there are triplet states, whose lifetimes are much longer. Some of the energy from singlet excited states can be transferred to the first triplet excited state by nonradiative means. They can de-excite to

ground level triplet state by emitting delayed emission called phosphorescence. The wavelength of phosphorescence is larger than fluorescence because the triplet levels are lower than the singlet levels. From triplet excited states, energy can be transferred back to singlet excited state again by nonradiative means and molecules can de-excite by fluorescence. This constitutes the slow component.

Radiationless de-excitation of molecules is called *quenching*. High ionization density along the trajectory of charged particle leads to quenching from damaged molecules and a consequent lowering of scintillation efficiency (Birks,1964). Ionization quenching decreases the intensity of the fast component (but not the slow component) and therefore gives rise to nonlinear light response for heavy ionizing particles such as p, d and α.

2.4.2 Pulse Shape Discrimination (PSD)

The scintillation pulse as described above consists of a fast and a slow component, with majority of light yield occuring in the fast component. *The fraction of the light appearing in the slow component depends on the nature of the exciting particle.*

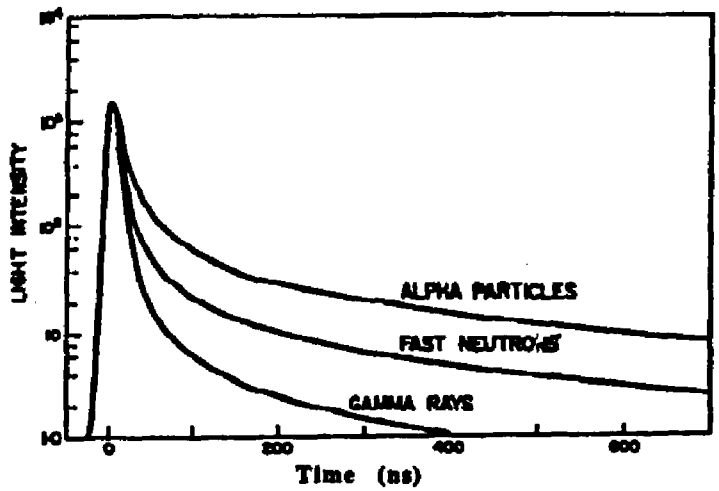

Fig. 2-4: The time dependence of scintillation pulses in stilbene (equal intensity at time zero) when excited by radiations of different types. (From J.B.Birks , *The Theory and Practice of Scintillation Counting* . Copyright 1964 by Pergamon Press Ltd. Used with permission.)

Therefore, the relative intensity of the fast component compared to the slow component exhibits pulse shape discrimination properties (Birks,1964). Figure 2-4 shows the differences observed in stilbene (crystal organic scintillator) for alpha particles, fast neutrons (recoil protons), and gamma rays (fast electrons). Generally pulse of ~ 50 - 100ns duration is used for pulse shape discrimination (PSD).

Only the fast component is dependent on the ionization quenching and not the slow component, therefore, the relative intensity of the fast and slow components will depend on dE/dx. The slow component is dependent on the nature of the particle, as its intensity is different for different particles with the same energy. Therefore, the pulse shape depends both on the nature of the particle and on dE/dx. Dissolved oxygen in the scintillator decreases the intensity of the slow component and hence depreciates the PSD characteristic of the scintillator.

2.4.3 Light Response Function of Scintillators

The light output of scintillators for different particles with same energy varies. The light output is only linear for minimum ionizing particles, in this case electrons, but nonlinear for subrelativistic p, d, α and other heavy ions. The electron equivalent energy (E_e) to which heavier charged particles of energy E_p correspond are given by expressions parametrized by Madey et al. (1978) for the scintillators NE102, NE228 and NE224, and by Cecil et al. (1979) for NE213, by fitting to the experimental data. For energies above 1 MeV_{ee} (electron equivalent energy in MeV),

$$E_e = a_1 E_p - a_2(1 - \exp(-a_3 E_p^{a4})) \qquad (E_e > 1\ MeV_{ee})$$

and below 1 MeV_{ee} (Nakayama,K., 1981):

$$E_e = b_1 E_p + b_2 E_p^{2}, \qquad (Ee < 1\ MeV_{ee})$$

where, E_e and E_p are in units of MeV and the coefficients are dependent on the type of scintillator. For alpha particles, the coefficients for all different types of scintillators are the

same. For heavy ions, the second equation is used for all energies and the coefficients are the same for all energies and for all types of scintillators ($b_1 = 0.017$, $b_2 = 0$).

CHAPTER 3

DESCRIPTION OF THE NEUTRON DOUBLE SCATTER TELESCOPE

The UNH Neutron double scatter telescope (Fig. 3-1) was designed to be used as a ground based telescope, light weight, portable, nontoxic with a self contained electronics and data acquisition system. It was engineered and constructed by Spectra Research Inc. of Portsmouth, N.H.

The telescope consists of two pairs of neutron detectors forming a rectangular array of four modules. The two upper detectors are designated - D1A and D1B and the two lower detectors - D2A and D2B. Each detector is 25.4 cm in diameter and 12.7 cm deep, filled with mineral oil based organic scintillator BC519. The vertical separation of each pair of detectors is 91.44 cm center to center and horizontally 63.5 cm center to center. Each upper detector is fully surrounded on all sides by charged particle shields, which detect the entry of muons and charged particles into the system and also detect the escape of energetic recoil protons from neutron scattering inside the main detector. The lower detectors have charged particle shields at top and bottom to increase the muon rejection efficiency of the telescope and to add a level of redundancy to the detection of escaping recoil protons not completely stopped in upper shields, which look like neutrons as they pass from upper to lower cells. Neutrons scattered in shields cannot be differentiated from the real events if the energy deposited in shields is less than shield software threshold (~40 keV). The telescope is normally operated so that the upper and lower detectors are in delayed coincidence, and charged particle shields in anticoincidence. This mode is called the *neutron mode* of the telescope. The telescope can also be operated in other modes - *muon mode* and *singles*

UNH NEUTRON TELESCOPE

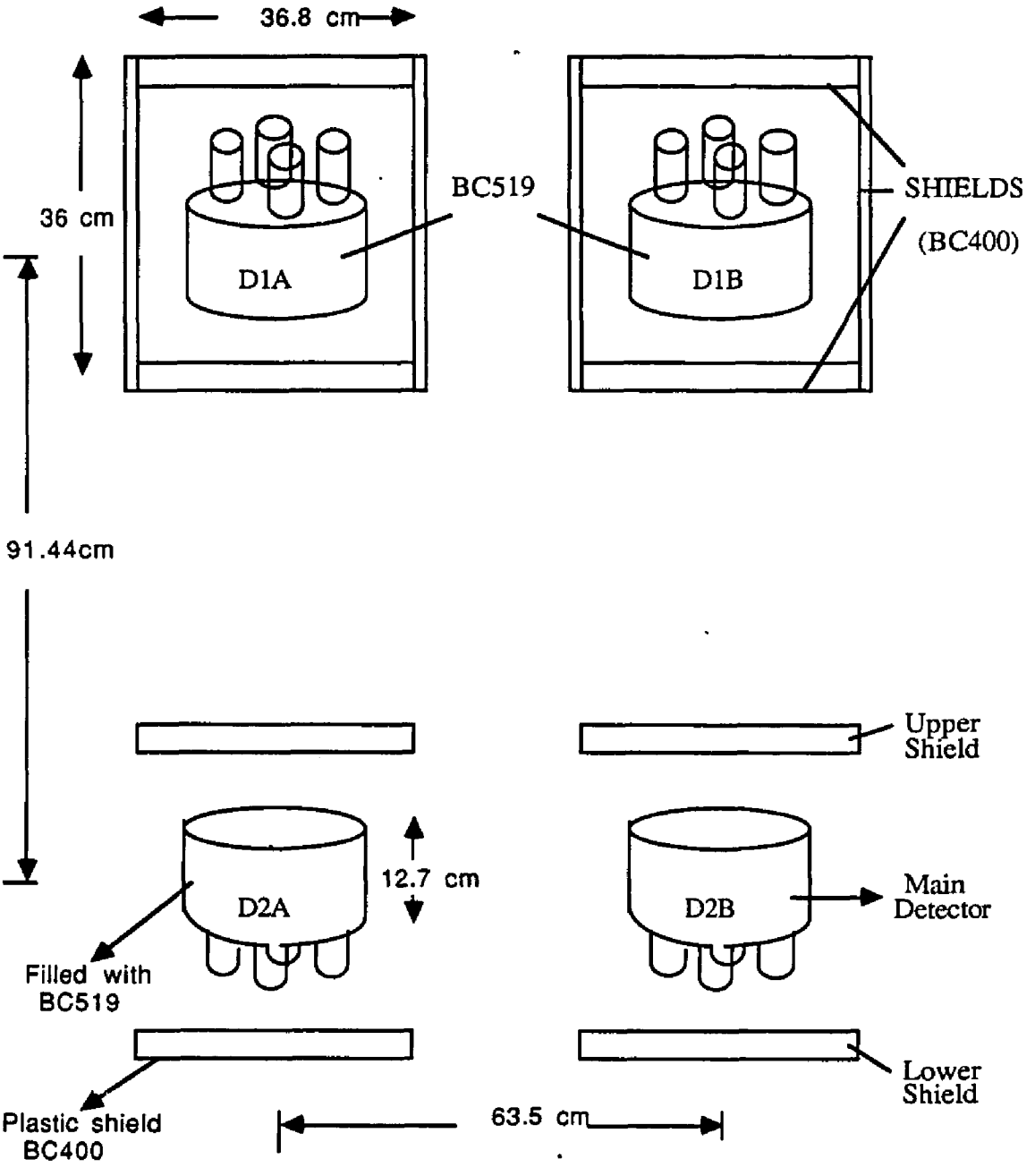

Fig.3-1 : UNH Double Scatter Neutron Telescope

mode , which are described later in detail. Incident neutrons can interact in either of the two upper detectors and then scatter into either of the two lower detectors, thus doubling the effective area of the entire telescope.

The four detectors D1A, D1B, D2A and D2B form four pairs of mini telescopes: two vertical (D1A-D2A and D1B-D2B) and two inclined (D1A-D2B and D1B-D2A). We shall refer to the two vertical pairs of telescopes as A and B, and the two inclined telescopes as AB and BA. Events are digitized and stored on an IBM PC hard disk. Each event is characterized by eight parameters :

(1) master coincidence (MC), i.e , in which of the four mini telescopes the event occurred;

(2) summed energy deposit in the upper detector (D1M);

(3) summed energy deposit in the upper shields (D1S);

(4) pulse shape in the upper detector (D1PSD);

(5) summed energy deposit in the lower detector (D2M);

(6) summed energy deposit in the lower shields (D2S);

(7) pulse shape in the lower detector (D2PSD); and

(8) time of flight between the upper and the lower detector (TOF).

3.1 Principle of Neutron Detection

This telescope utilizes the elastic scattering of neutrons with protons in the upper and lower detectors to measure their incident energy and zenith angle. The incident neutron scatters elastically from a proton in the upper detector, producing a recoil proton of energy E_p with the scattered neutron going off with energy $E_{n'}$ (Fig. 3-2). The scattered neutron may then interact in the lower detector, depositing either its total energy and stopping there or only part of its energy and escaping. Neutron interactions with nuclei other than hydrogen give rise to incorrect values of energy and angle, and are discriminated by

different criteria during analysis. The energy measurements and background reduction methods are described in detail below.

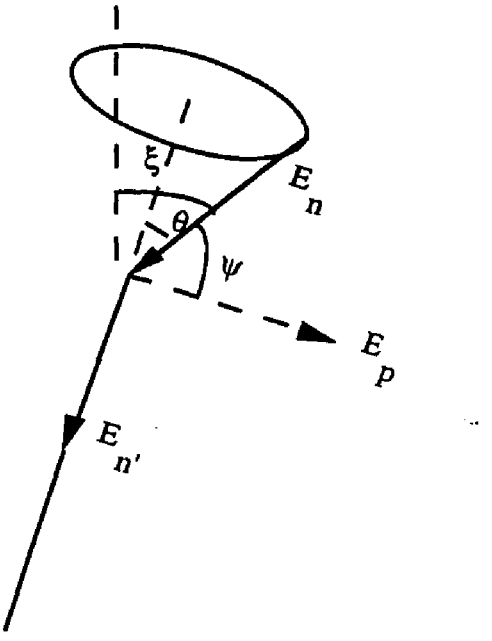

Fig. 3-2 : Principle of Neutron Detection

The relations between scatter angle, energy of proton, energy of scattered neutron and energy of incident neutron are given by following relativistic kinematic relations described in chapter 2 :

$$E_n = E_p + E_{n'}$$

$$\tan^2\theta = \frac{2}{(1+\gamma)}\frac{E_p}{E_{n'}}$$

$$\tan^2\psi = \frac{2}{(1+\gamma)}\frac{E_{n'}}{E_p}$$

where $\gamma = (1-\beta^2)^{-1/2}$, $\beta = v/c$ and v is the velocity of the scattered neutron. For the nonrelativistic case, i.e , $\gamma \rightarrow 1$, $\tan^2\theta = E_p/E_{n'}$. Hence, if we can measure the energy of the recoil proton E_p and the energy of the scattered neutron $E_{n'}$, we can calculate the

incident neutron energy E_n and the scattering angle θ. For small scattering angles, the zenith angle ξ is taken to be on the average the scattering angle θ. If the direction of the recoil proton could be determined, then the azimuthal angle of incident neutron could be found. The scattered neutron and the recoil proton define a plane and the incident neutron has to lie in the same plane for conservation of momentum.

3.1.1 Energy Measurements

The energy of the recoil proton (E_p) in the upper detector is determined from the pulse height and the energy of the scattered neutron ($E_{n'}$) by measuring the time of flight (TOF) between the two detectors.

The recoil proton deposits its energy (E_p) by ionization in the scintillator. Part of this energy is converted into scintillation photons, which are seen by PMTs. In the PMT a current pulse is produced and measured. The height of this pulse depends on the total energy deposited. As the light response for the scintillator is not a linear function of the proton energy, the detector must be calibrated.

The TOF of a scattered neutron is the time difference between the fast pulses in upper and lower detectors. The amplitude of the pulse formed by TAC (time to amplitude converter) is directly proportional to the time difference. The energy of the scattered neutron ($E_{n'}$) is given by :

$$E_{n'} = m_n c^2 \ [(1-\beta^2)^{-1/2} - 1] \qquad (3.1)$$

where, $m_n c^2 = 939.5731$ MeV/c^2 (rest mass of neutron), $\beta = v/c = L / tc$; t = TOF and L is the center to center distance between detectors. For nonrelativistic case, $E_{n'} = m_n v^2/2$, where $v = L/t$.

3.1.2 Background Reduction

In the atmosphere there are other particles such as muons, electrons and gamma rays which are more numerous than neutrons. These particles contribute to the large background to the neutron measurements. To get a good signal to noise ratio, we must minimize this background. Also, the neutron can interact with carbon in the scintillator or with the aluminum walls of the detector and supporting structure of the telescope, producing other charged particles such as neutrons and/or gamma rays. The background is reduced by using the anticoincident charged particle shields, TOF and PSD criteria on events. Besides real double scatter neutron events there are also accidental events present, i.e , two uncorrelated neutrons interacting within the given TOF window. Rate of accidental events can only be estimated, and they cannot be discriminated from the real events.

A. Anticoincident Charged particle shields

Incident neutrons can be differentiated from charged particles (muons in the atmosphere or those generated by the frame of telescope) due to the presence of the anticoincident charged particle shields surrounding the upper detectors from all sides. Relativistic muons deposit energy ~ 2 MeV/cm in the shields. Low energy charged particles will either be stopped in the 1 cm thick shields (see Fig. 3-3) or will deposit some energy, and the event can be rejected because the shields are in anticoincidence with the main detector (hardware threshold ~ 1.5 MeV_{ee}). Gamma rays as well as neutrons have less probability of interaction with the charged particle shields because the shields are quite thin. Therefore, gamma rays are seldom rejected by shields and can give rise to a real event in the detector. Due to a small probability of interaction with the neutrons, the charged particle shields will attenuate the neutron flux by a small amount. Neutrons scattering from the aluminum walls of the detectors and shields cannot be differentiated from the real events as, due to the small thickness of walls (1 mm), the interaction probability is small.

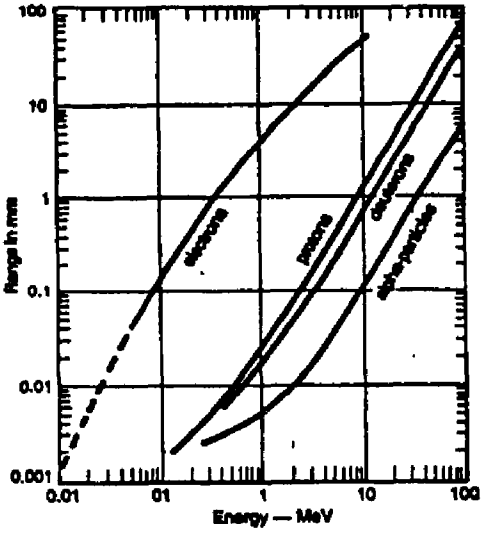

Fig. 3-3 : Range of Particles in Plastic Scintillator BC400

If the recoil proton with energy E_p does not deposit all its energy inside the detector, it will go on to interact in the anticoincident charged particle shields surrounding the detectors, and the event will be rejected.

B. Time of flight (TOF) discrimination

All downward moving gamma-rays of any energy will have the same TOF and can be rejected from the neutrons. Muons being highly relativistic also have the same TOF as gamma rays. Neutrons have different TOF depending on their energy (eq. 3.1). The signal in the upper detector generates a *start* for TOF and signal in lower detector - a delayed *stop*. Therefore, upward moving events can be distinguished from downward moving events. TOF discrimination, therefore, can reject gamma rays (both upward and downward moving) and upward moving neutrons.

C. Pulse shape discrimination (PSD)

Incident gamma rays and also gamma rays generated inside the liquid scintillator by interaction of neutrons can be differentiated from recoil proton signals due to different PSD characteristics. Neutrons produced by the interaction of incident neutrons or gammas with the aluminum wall cannot be differentiated from the real events by the scintillator.

Gamma rays Compton scatter from electrons in the scintillator, and the energetic electrons produce a fast pulse. The recoil proton from (n,p) scattering produces a slower pulse. Neutrons can interact with carbon nuclei in addition to hydrogen in the scintillator and produce particles like deuterons, alphas and/or gamma rays. The pulse produced by heavy charged particles is even slower than the proton pulse (Chapter 2). The proton pulse formed due to (n,p) elastic scattering can be differentiated by PSD from other particles.

3.1.3 Advantages and Disadvantages of UNH Double Scatter Telescope

Coincident requirements between the upper and the lower detector, PSD and TOF criteria, and anticoincidence with charged particle shields give a good signal to noise ratio.

The thickness of the detectors deteriorates TOF resolution. In order to measure high energy neutrons which have a smaller cross section and therefore larger mean-free path length, larger thickness is needed. Hence there is a trade off between measuring high energy neutrons and good TOF resolution.

The large distance between vertical detectors helps the TOF resolution but decreases efficiency of the telescope as the solid angle becomes smaller. The light output and PSD characteristics of BC519 are lower than for NE213, but its efficiency for proton elastic scattering is higher due to higher H:C ratio. It is also nontoxic (mineral oil base) with high flash point, which is a desirable quality if the instrument has to be dismantled and shipped. The charged particle shields slightly attenuate the incident neutron flux but help in giving a good signal to noise ratio by rejecting incident charged particles (mostly muons) and events whose energy is not totally absorbed in the upper detector.

3.2 Mechanical design of the Telescope

The telescope is constructed of aluminium to keep its mass as small as possible. The main detectors and shields are supported by an aluminum frame structure, which can be easily assembled and dismantled.

3.2.1 Main Detector

The main detector is an aluminium cylinder with an inner diameter of 25.4 cm and a depth of 12.7 cm. It is filled with the mineral oil based scintillator BC519 (Table. 3-1). To allow for thermal expansion of liquid, the upper part of main detector has an extra compartment (reservoir of height 1.09 cm) which contains liquid and dry nitrogen At 20°C, the liquid level above the baffle in reservoir is around 3 mm, the rest of the volume being N_2 is available for expansion of the liquid.

The whole cell is purged with nitrogen gas to remove dissolved oxygen in the scintillator and to fill the extra space in the reservoir. Oxygen degrades the PSD and the light output characteristics of the scintillator, so the detector must be air tight.

For optimum light collection, the inner walls of detector are painted white with NE562 reflector paint. This paint does not react with the scintillator.

Each main detector is viewed by four Photomultiplier tubes (PMT), with the face immersed in the scintillator so as to have good light coupling. The PMT's used are EMI D363A (or electronic equivalent EMI 9755B) type with quantum efficiency of ~ 24 % and 52 mm in diameter. The PMT is held inside a aluminium casing by viton O-ring, sealed from the inside by white adhesive (RTV 730), and from outside by black potting of SILGARD 170. The aluminium casing is covered on the outside by "mu metal" to prevent the change in gains of PMT by the earth's magnetic field as the detector is moved from one location to another. (PMT's are very sensitive to the presence of magnetic fields, which upset the delicate focusing conditions in the tube. For this reason, a PMT is usually

surrounded by a high permeability "mu metal" shield). A green light emitting diode (LED) is placed at the center of main detector, to check the gain of the PMTs.

3.2.2 Anticoincidence shields

To detect charged particles (see earlier discussion) the main detectors are surrounded by anticoincident shields. The upper detector is surrounded from all sides by charged particle detectors from top and bottom by diffusion box type shields (upper (US) and lower (LS) shield) and from the sides by four side shields (SS). The lower detector only has diffusion box type shields at the top and bottom (Fig. 3-1).

A. Diffusion box shield

The diffusion box shield is a hollow rectangular aluminium box painted white (by $BaSO_4$) on the inside for good reflection of the scintillations produced in the plastic scintillator BC400 (37.5 × 37.5 × 1 cm), which is clamped at the bottom surface of the box. The characteristics of the scintillator are given in Table 3-1. Two PMT's (not in contact with the scintillator) placed at opposite ends of the box view the scintillations caused by interaction of charged particles with BC400. The bottom diffusion shield is exactly designed as the upper diffusion shield except for its dimensions, which are less (32.4 × 32.4 × 1 cm) so as to have a snug fit with the side shields.

B. Side shields

The plastic scintillator BC400 (35 × 36 × 1 cm) is sandwiched between two aluminium plates. The large flat faces of plastic are highly polished and the edges of plastic are covered by 0.5 mm thick Al mylar tape. From the outer side, the PMT is optically glued to the flat face of plastic scintillator BC400 with the help of silicon adhesive ND711. The aluminium frame for the PMT is put under tension for good contact with the plastic. The four side shields are put around so that they overlap and form a snug housing with the

upper and bottom shields around the main detector. Charged particles incident on the main detector cannot escape without being detected by the shields around the detector.

Table 3-1: Characteristics of the Scintillator

	BC519	BC400
Type	Liquid	Plastic
Light Output (% Anthracene)	60	65
Decay Time, (ns)	4	2.4
Density	0.875	1.032
Wavelength of emission (nm)	425	423
Index of refraction	1.5	1.58
Flash Point (°F)	166 (74 °C)	-
No. of C Atoms per cm^3	3.83×10^{22}	4.74×10^{22}
No. of H Atoms per cm^3	6.62×10^{22}	5.23×10^{22}
Ratio H:C Atoms	1.728	1.103
No. of Electrons per cm^3	29.6×10^{22}	33.7×10^{22}

3.3 Electronics

Each main detector is viewed by four Photomultiplier Tubes (PMTs), the diffusion boxes by two PMTs and each side shield by one PMT.

Photons are incident at the cathode of PMT which emits photoelectrons of ~1 eV. These photoelectrons are accelerated by the high voltage applied to the PMT. A potential is applied at the successive dynodes by the bleeder string at the base of PMT. Electrons impinging on the dynodes generate a number of secondary electrons which are again accelerated by the potential applied at the next dynode. This process is repeated at each subsequent dynode and the secondary electrons from the last dynode are collected at the

anode. Two pulses : (1) A fast negative pulse from the anode (RT ~ 2-4 ns) and (2) a slow positive pulse (RT ~ 50 ns) from the tenth dynode are input to preamplifiers located at the base of PMT. The anode pulse is used for TOF measurements and the dynode pulse for coincidence and timing logic, PSD and pulse height analysis. The anode outputs from the shield PMTs are not used. Block diagram of full circuit is shown in Fig. 3-10.

3.3.1 Time of Flight circuit

The anode signals from each of the four PMT's in the upper main detector are summed together in a high speed amplifier (Upper Fast Summer Box). The output of these summed signals provides a fast signal, indicating a presence of an event in the upper detectors. Similarly, anode signals from the lower detectors are summed together in a Lower Fast Summer Box and provide a fast signal output for the event in the lower detectors. The time difference between the arrival of fast signal from the upper and from the lower detectors determines the TOF for that event.

There is always some degree of uncertainty in the timing signal due to *jitter* or *walk* or both. The main sources of *time jitter* are electronic noise and statistical fluctuations of the detector signals. The walk could be due to a difference in signal amplitudes for pulses arriving at the same time and of the same shape, or for constant amplitude pulses, if changes in pulse shape occur (Knoll, 1989). There are many methods for picking the time arrival of a pulse, e.g leading-edge, zero-crossing, constant-fraction, amplitude and risetime compensation (ARC), etc. We have used the constant-fraction discriminator (CFD) method to pick the time arrival of signal which produces an output (logic pulse) at a time when the leading edge of the pulse has reached a *constant fraction* of the peak pulse amplitude. This point is then independent of pulse amplitude for all pulses of constant shape.

If the amplitude of input fast pulse coming from either the Fast Summer Box is greater than the CFD threshold, the CFD module produces three output logic pulses: one

positive slow logic pulse to gate the cell coincidence modules and two fast timing negative pulses. A pulse from the D1 CFD is used as a "start" signal for the PSD TAC (Time to Amplitude Converter). The other timing signal from the upper CFD (or D1 CFD) is used as a "start" signal for the TOF TAC. The timing output signal from D2 CFD is delayed by a constant amount (52 ns delay) and used as a "stop" for TOF TAC (Fig. 3-4). A delay is necessary so as to measure both upward moving and downward moving events. The principle of the TOF measurements is explained in Fig. 3-5. The TOF TAC produces an output pulse, whose amplitude is a linear function of the time between the "start" and the "stop" pulses. This signal goes to the TOF input of the Track and Hold (T/H) module and is then digitized by the ADC and stored as one of the parameters of a event . The cell coincidence is discussed in Section 3.3.5.

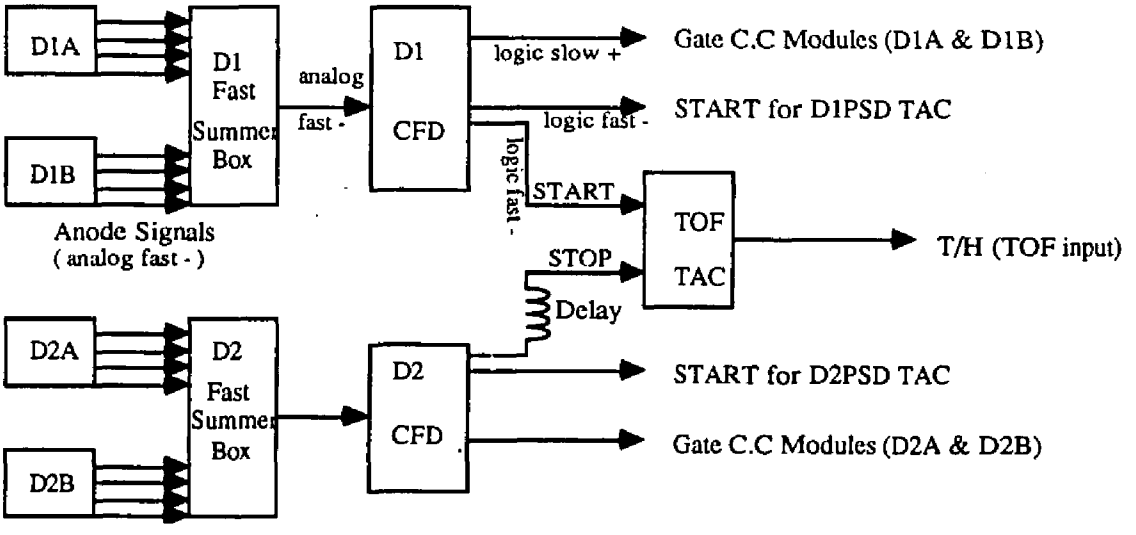

Fig.3-4: Time of Flight (TOF) Block Diagram

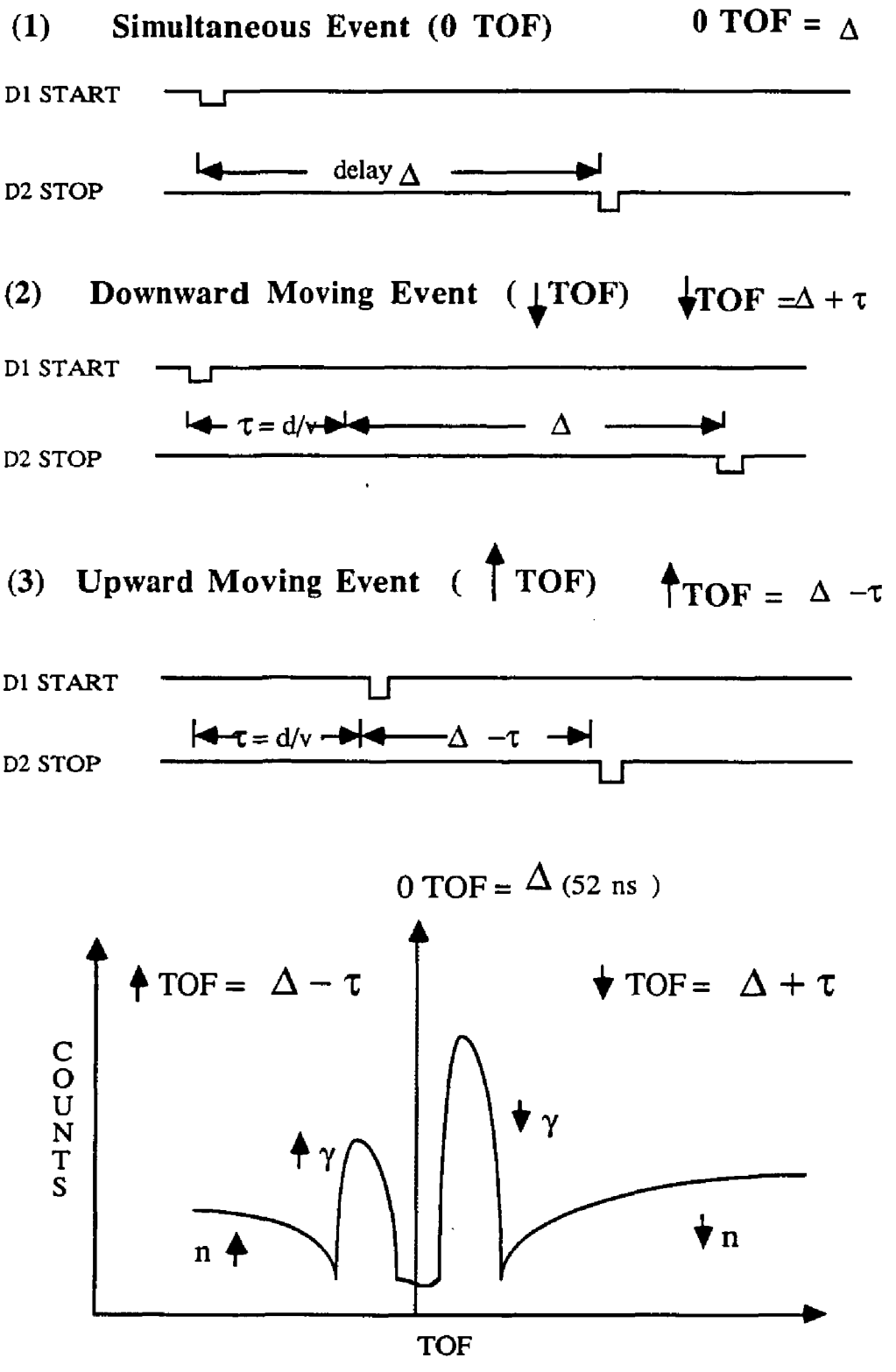

Fig.3-5 : Principle of TOF measurement

3.3.2 Main Pulse Height Measurements (D1M & D2M)

The dynode outputs from the four PMTs of each main detector are summed together and fed to a Dynode Buffer Box which shapes the pulse for proper pulse shape discrimination (PSD). The dynode buffer box produces two medium speed signals: one signal goes to the cell coincidence module, and the other to the Medium Speed Summer Box (Fig. 3-6).

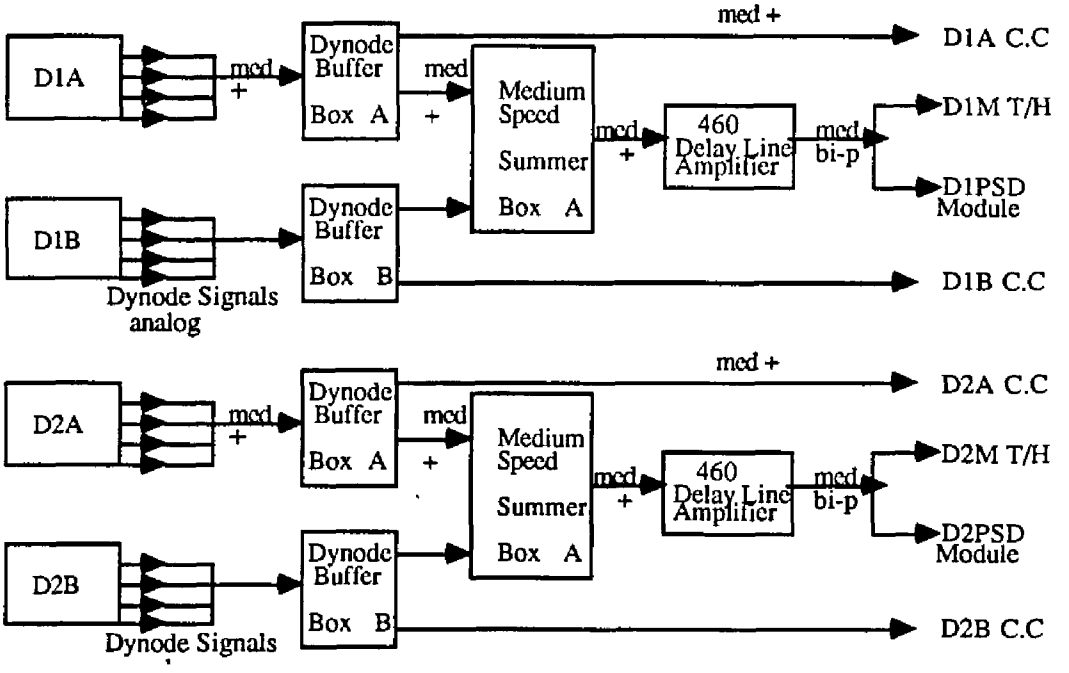

Fig. 3-6 Block Diagram for Main Pulse Height Measurements

Dynode signals from the upper detectors are summed together in the D1 Medium Speed Summer Box and those from the lower detectors in the D2 Medium Speed Summer Box. The same lengths of cable should be used to connect outputs of the Dynode Buffer Box A and the Dynode Buffer Box B to the Medium Speed Summer Box. Any difference in length could affect the PSD signal because of the distributed capacitance in the cable. The Output of the Medium Speed Summer Box is used as input for the Delay Line Amplifier (Ortec

460), which produces a bipolar pulse. This pulse is split into two by a "T", one of it going to the main input of T/H module and the other as a "stop" signal for PSD zero crossing module. The main input signals of T/H (D1 and D2) are digitized and stored as the *Pulse-Height* of the event (D1M and D2M), which is a function of the energy deposited in the main detectors.

3.3.3 Pulse Shape Discrimination (PSD) Circuit

Pulse Shape Discrimination is based on differences in the rise times of pulses produced by different particles, hence it is also a timing measurement like TOF. The PSD of both upper and lower detectors, D1PSD and D2PSD, are measured. The PSD TAC gets a "start" signal from CFD timing signal which is delayed. One of the bipolar pulse from 460 Delay Line Amplifier is sent as an input to PSD zero crossing module, which then sends a "stop" pulse (at the time when bipolar pulse crosses zero) to the PSD TAC.

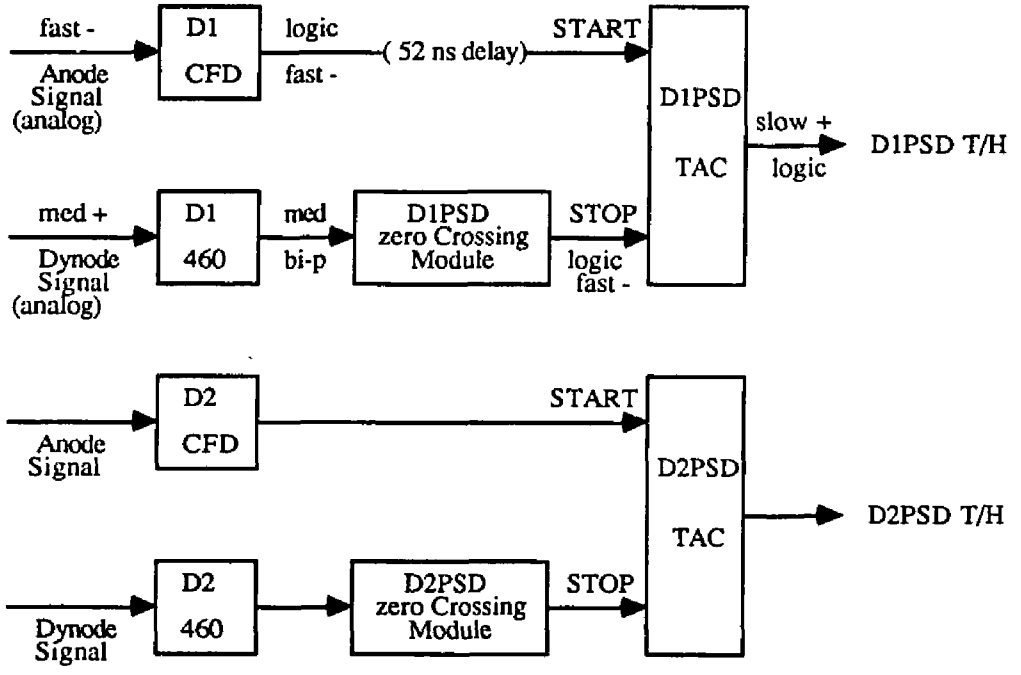

Fig. 3-7: Pulse Shape Discrimination (PSD) Block Diagram

The output of the PSD TAC is sent to the PSD input of T/H module (D1PSD and D2PSD), which is then digitized and stored as the D1PSD and D2PSD parameter of the event (Fig. 3-7).

3.3.4 Shield Pulse Height Measurements

Only dynode signals from shield PMTs are used for analysis as no precise time measurement is performed on the shield pulses. Both PMT signals from the upper shields (US) are fed into a Dual Amplifier Board. Each input signal is divided into a medium speed and a slow signal. Both medium speed signals are then combined and sent to a medium speed summer (Fig. 3-8), which produces two medium speed (MS) outputs. One of these MS outputs is used for cell coincidence. The same thing is done with two PMT signals from the Lower Shields (L.S.) and four PMT signals from Side Shields (S.S.). So, three MS signals for US, LS and SS cell coincidence are produced from the Upper Shield Box (D1A and D1B Shield Box).

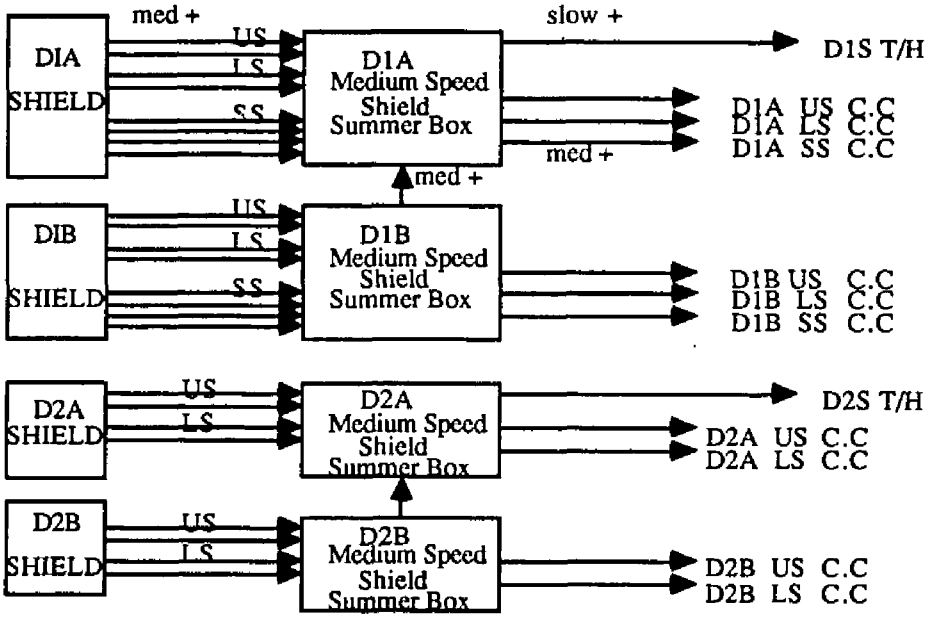

Fig. 3-8: Block diagram of Shield Pulse Height Measurement

All slow speed signals from the Dual Amp. Boards are summed together in a slow summer. The slow sum output from the D1B is summed together with the D1A slow output in a master summer located in the D1A Shield Box. This slow output goes to the D1S input of T/H, then is later digitized and stored as the D1S parameter of the event. The lower detector shield signals are similarly processed in D2A and D2B Shield Boxes, except the side shield signals, as they are not present for lower detectors. The slow output for lower detectors goes to the D2S input of T/H and stored as the D2S parameter of the event.

3.3.5 Coincidence Circuit and Data Acquisition System

The main elements of coincident and data acquisition system are: (1) Cell coincident modules (one for each detector), (2) Master Coincident module, (3) Track and Hold Module , (4) Z80 Standard Bus Computer and (5) IBM PC/XT computer.

In the Cell coincident modules, signals from the main and the shields are compared for coincident criteria driven by software after they pass through their respective thresholds. In master coincidence, signals from all four detectors are compared for coincidence criteria also given by software. If the coincident criteria are met, all eight signals go through the Track and Hold circuit, where their respective levels are held for digitization by ADC, and the event is stored in the IBM PC/XT.

A. Cell Coincidence Circuit

Each of the four detectors D1A, D1B, D2A and D2B have their own cell coincidence modules called D1A cell coincidence module (D1A CC) and so on. Each cell coincidence module has four inputs: Main, US, LS and SS as described in above sections. The SS input is used only for upper detectors D1A and D1B. They are gated by a positive output signal from CFD as described previously. If the input signals are greater than their respective C.C thresholds, and coincidence criteria or "mask" sent by software is met, an output logic pulse is sent to Master Coincidence (MC) module.

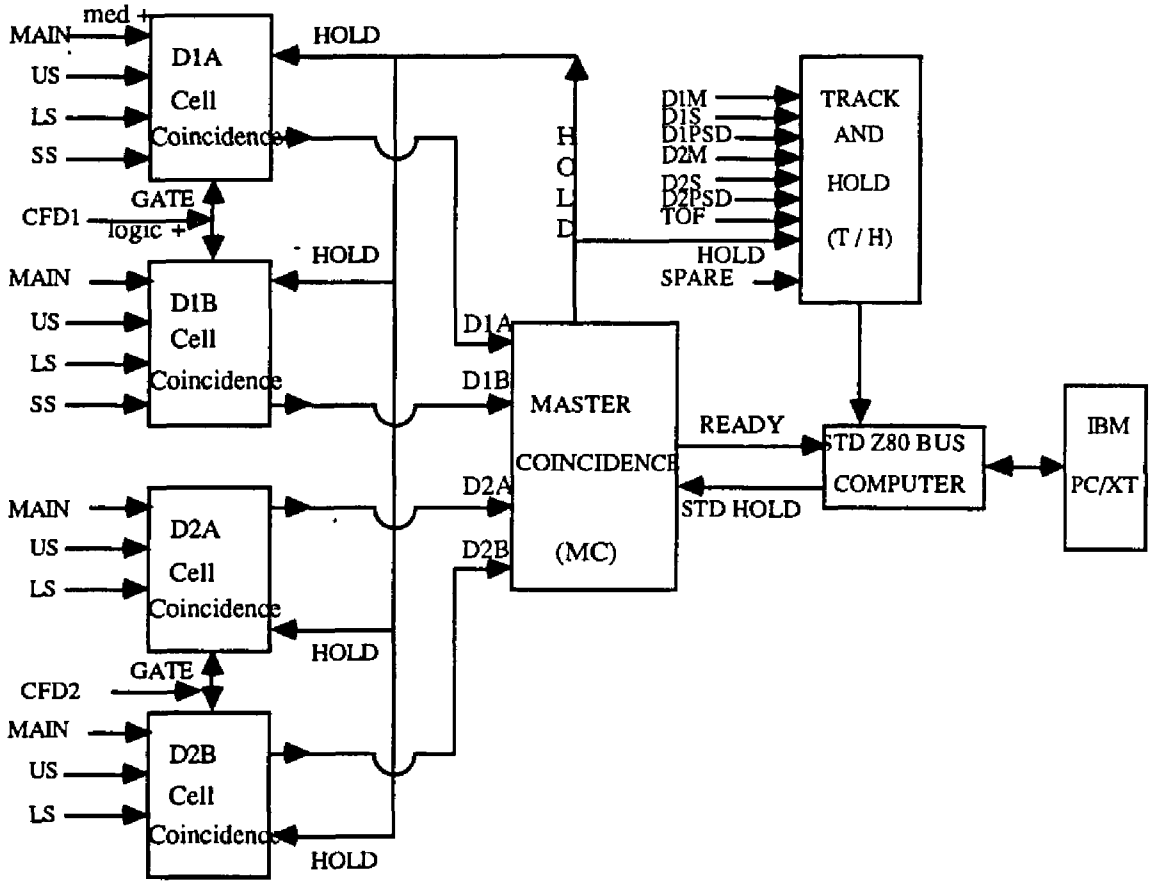

Fig. 3-9 : Block diagram of Coincidence and Data Acquisition circuit

The count rate of incoming pulses to cell coincidence can be observed on an Oretec 772 counter, which counts the pulses for one second coming into the CC and displays it for a second before being reset to count again. By changing the position of Rate Selector on CC module, the count rate for either the main, US, LS, SS or total shield can be observed.

B. Master Coincidence (MC) Circuit

The MC circuit gets logic output signals from the four cell coincidence modules. When the signals from CC modules match with the MC mask sent by the software, a hold and a ready pulse are generated. A hold pulse is sent to the cell coincidence modules so that they do not send anymore signals until the previous ones have been digitized and to the T/H

module to hold the input pulses at their respective levels. A ready pulse is sent to the STD bus, telling it to receive the data from T/H. MC puts a tag on the event depending on which upper and lower detector CC sent the signals.

C. Track and Hold (T/H) Circuit

There are eight input signals to T/H module: D1M, D1S, D1PSD, D2M, D2S, D2PSD, TOF and SPARE. The pressure readings from a precise digital barometer are fed to SPARE input slot. A hold pulse from MC is sent to T/H, where it holds all the eight input analog signals at their respective levels on the STD bus to be digitized and stored on computer. There are two adjustments associated with each T/H input:

1) Zero or Null Adjust: With no input signal, the output from ADC should correspond to channel # 2 or 3. This way the value of the Zero signal or offset is known.

2) Strobe Adjust: The timing of Hold pulse for each input on T/H can be adjusted such that it holds the pulse only at its maximum level, otherwise the values of parameters for the event may not be correct. Since the input signals are not all of the same type, the position where they are held is different for different signals. D1M and D2M are captured at the negative peak of the incoming bipolar signal from 460 Delay Line Amplifier. D1S, D2S, D1PSD, D2PSD and TOF signals are captured at the positive peak of the incoming unipolar pulse. The SPARE input (last input on T/H) captures a DC level at its input. All inputs except the SPARE one are AC coupled, therefore can only accept pulses.

D. Data Acquisition System

The data acquisition system links the telescope with a IBM PC/XT microcomputer through a Z80 Standard (STD) bus, so as to control and receive the data from the telescope. The STD bus receives all the input data from T/H, digitizes them on an Analog to Digital Converter (ADC) board, and sends the data to the IBM PC/XT by serial link, where they are stored on a hard disk. Using the acquisition software, different coincidence criteria between main and shield detectors, control switching (on/off) of different PMTs and also

control LED switching (on/off) in different main detectors can be made. It has a real time data display of histograms for all eight parameters D1M, D1S, D1PSD, D2M, D2S, D2PSD, TOF and Barometric Pressure. The real time display also provides for multiple scatter plots of different parameters. Data are being stored directly on a 10 MB hard disk (software controlled, as data can be accumulated on screen without being stored), and later transferred onto a 60 MB tape cartridge and floppy diskettes. A typical neutron run of 24 hr at Leadville, CO requires space of ~ 1 Megabyte. Details of data collection are given in chapter 5.

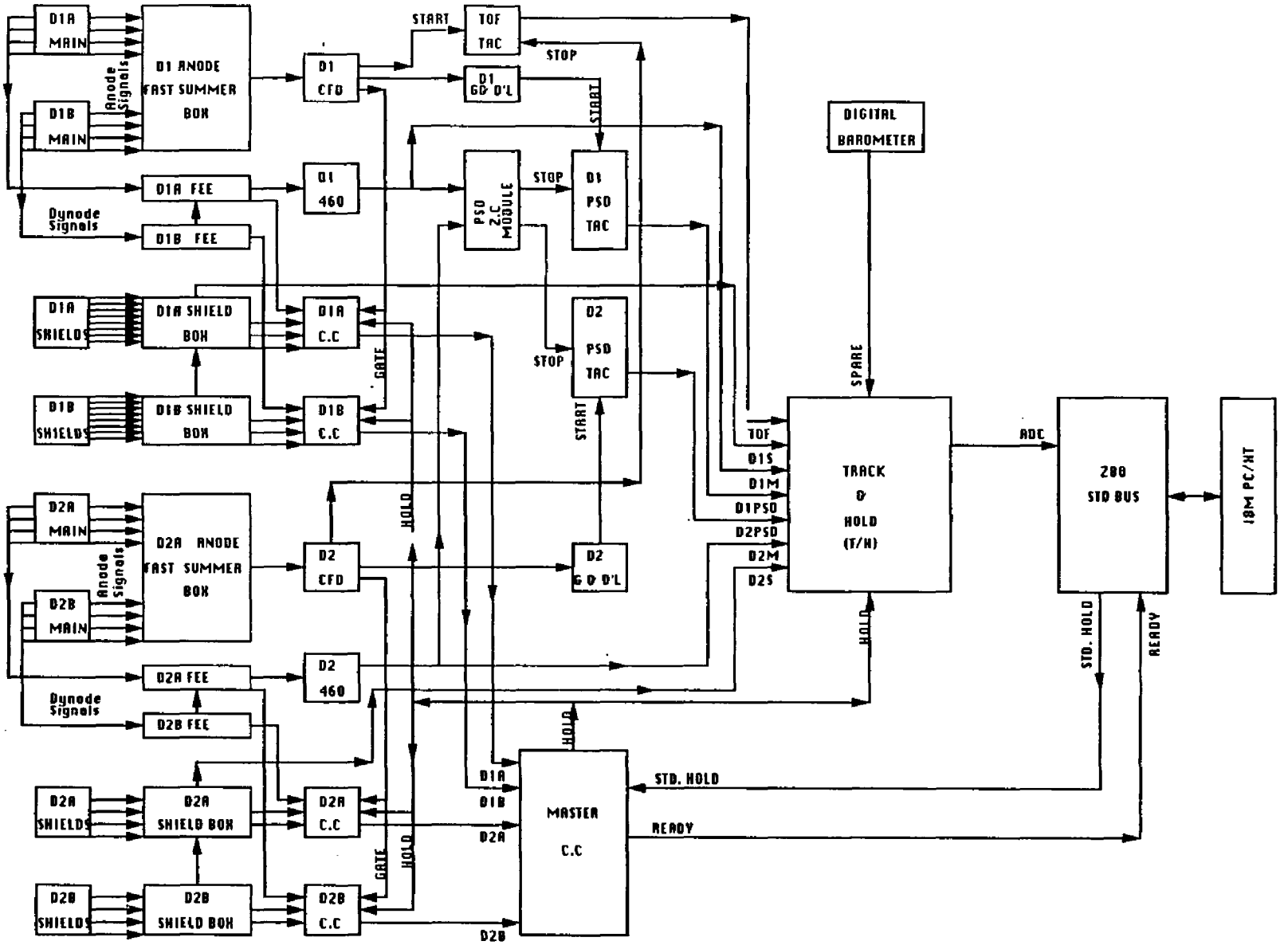

Fig. 3-10 : Block Diagram of the Telescope

CHAPTER 4

CALIBRATION OF THE TELESCOPE

The conversion of raw neutron count rate, as measured by the telescope, into an incident neutron flux as a function of neutron energy and angle requires calibration of the telescope. The Energy calibration consists of the pulse height calibration of the upper and lower main detectors in terms of proton energy (MeV) and the calibration of the time of flight (TOF) in time (ns). The incident neutron energy can then be determined using Eq. (2.1) and Eq. (3.1), i.e. summing the recoil proton ionization in D1 and the recoil neutron energy as measured by TOF. Efficiency measurements are performed to determine the *Response matrix R(E,θ)* of the telescope for the given range of energies and angles, which is then used for deconvolution of the count matrix (in E,θ) to an incident flux spectrum. The calibration was performed at the Indiana University Cyclotron Facility (IUCF) in September 1986.

4.1 IUCF Calibration

The telescope was calibrated at the Indiana University Cyclotron Facility (IUCF) using their neutron production facility. Proton beams at nominal energies of 30, 50, 80 and 135 MeV were directed onto ^{7}Li targets using the beam swinger. The stripper loop was used at 30, 50 and 80 MeV to avoid TOF wrap-around from different beam bursts. A detailed listing of the proton energies are given in Table 4-1. Beams of monoenergetic neutrons produced by the bombardment of protons on the ^{7}Li target (^{7}Li(p,n)^{7}Be) exiting at zero degrees were used for the calibration of the telescope. The unscattered proton beam was swept into a Faraday cup by a beam-dump magnet. For high energies any protons

scattered into the 0° neutron beam were removed by putting a Cu plate in the path of neutron beam at 0°. The telescope was placed horizontally in a wooden hut 43 m away in the zero degree neutron beam direction (see Fig. 4-1). For each given neutron energy, four runs were taken corresponding to four different angles (0, 10, 20 and 30 degree) between the telescope's axis and the direction of incident beam of neutrons. Due to a lack of beam time, the 30 degree run for 30 MeV protons was not done.

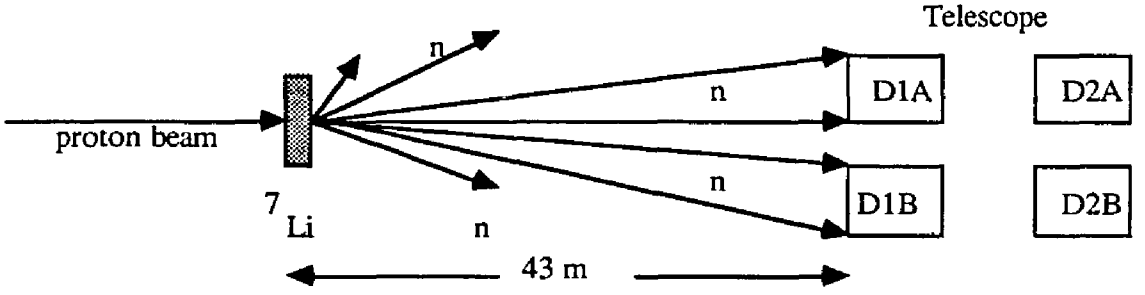

Fig. 4-1: Production of neutrons at IUCF

4.1.1 Production of Monoenergetic Neutrons

Monoenergetic neutrons are produced by the bombardment of protons on a ^{7}Li target.

$$p + {}^7Li \rightarrow n + {}^7Be \qquad Q = -1.646 \text{ MeV.} \qquad (4.1)$$

$$p + {}^7Li \rightarrow n + {}^7Be^* \qquad Q = -2.076 \text{ MeV} \qquad (4.2)$$

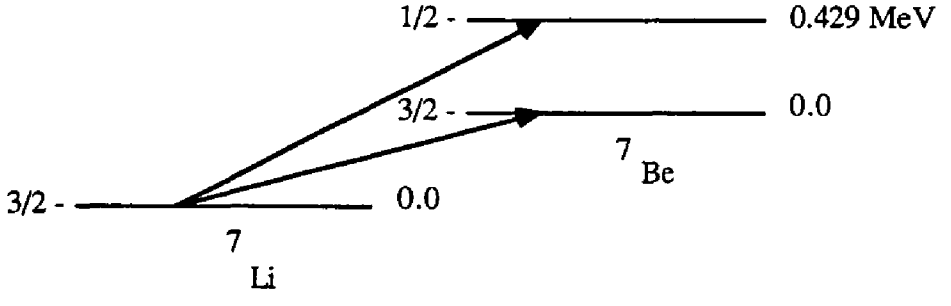

The threshold proton energy for the first reaction (Eq. 4.1) is 1.881 MeV and for the second 2.378 MeV (Beckurts and Wirtz, 1964). In the second reaction (Eq. 4.2), the first excited state of ^{7}Be decays back to the ground state by emitting a gamma ray of 0.429 MeV. Fermi transitions ($\Delta J=0$) dominate the low energy spectra ($E_p < 45$ MeV) and Gamow -Teller ($\Delta J=1$) for $E_p > 100$ MeV (Goodman, 1980). The differential cross-section $d\sigma/d\Omega$ at zero degrees (Rapaport et al., 1989) is taken to be the sum of both the reactions (g.s + 0.431) and is presented in Table 4-1 .

Neutron peaks corresponding to ground and first excited state are only 0.43 MeV apart and cannot be separated since the proton energy loss in the target itself (253 mg/cm^2) due to coulomb interactions with electrons is much larger. The energy loss of incident protons is defined as :

$$\Delta E = \int dE/dx \; dx \qquad R > t$$

or

$$\Delta E = (dE/dx)_o \, t \qquad t << R,$$

where R is the range and $(dE/dx)_o$ is the stopping power for the initial energy of the proton. If the thickness t is a considerable fraction of range, dE/dx cannot be considered constant. So the range R is used in calculating the energy loss ΔE_p :

$$\Delta E_p = (E_p - E_1) \qquad (4.3)$$

where, E_1 is the proton energy corresponding to the range (R - t) in ^{7}Li and E_p is the incident proton energy. The spread in neutron energy due to the thickness of the target is taken to be the same as the proton energy loss (ΔE_p) which is given in Table 4-1. The average neutron energy is taken to be the one corresponding to the ground state transition (Eq. 4.1).

$$E_n(\text{MeV}) = \left(E_p - \frac{\Delta E_p}{2}\right) - 1.646 \text{ MeV}. \qquad (4.4)$$

Table 4-1 : Incident proton beam parameters

Energy of Proton E_p (MeV)	Proton Energy Loss in ^7Li ΔE_p (MeV)	Average Energy of Neutrons E_n (MeV)	Range of neutron energies (MeV)	Cross section $d\sigma(0^o)/d\Omega$ $^7Li(p,n)^7Be$ (mb)
29.7	4.6	25.75	23.45 : 28.05	27
49.9	2.9	46.8	45.35 : 48.25	32
80.1	2.1	77.4	75.85 : 78.95	39
135.8	1.5	133.4	132.15 : 134.65	42

The total number of neutrons produced at zero degrees was calculated as follows:

$$N_n = N_p N_t \frac{d\sigma(0^o)}{d\Omega} \Delta\Omega \qquad (4.5)$$

where, N_n - the total number of neutrons produced at 0° in solid angle $\Delta\Omega$

N_p - the total number of incident protons on the ^7Li target

N_t - total number of ^7Li target nuclei per cm^2

$d\sigma(0^o)/d\Omega$ - differential cross section at 0° for the (g.s + 0.429) $^7Li(p,n)^7Be$ reaction

$\Delta\Omega$ - solid angle subtended by one of the upper detectors of the telescope from the position of the Li target.

The integrated current from the two Faraday cups is converted into pulses (1 kHz corresponding to a beam current integrator full scale (FS) reading) and sent to a scaler which measures beam integrator counts (BIC). The total number of incident protons N_p was calculated using the beam integrator counts (BIC) and the beam current integrator full scale (FS) reading:

$$N_p = BIC \frac{FS(nA)}{1000} \cdot 10^{-9} \cdot \frac{1}{q} , \quad (4.6)$$

where q is the charge of proton in coulombs. The Li target was 253 mg/cm^2 thick, which gives the value of $N_t = 2.17 \times 10^{22}$ nuclei/cm^2. The solid angle $\Delta\Omega = 2.74 \times 10^{-5}$ sr. The values of the total number of neutrons produced (using Eq. 4.6) for different beam runs are given in the Table 4-2.

Table 4-2 : The total number of incident neutrons at the telescope

E_n (MeV)	Beam Angle (θ)	Length of run Δt (sec)	FS (nA)	BIC	No. of protons on the target (corrected for zero beam current) Np ($\times 10^7$)	Total No. of neutrons produced at the target in $\Delta\Omega$ at 0°. N_n	Total number of neutrons incident on the telescope (after attenuation) N
25.75	0	7620	20	2348140	29142200	4678390	3368441
	10	13980	20	4478240	55593550	8924800	6328233
	20	13680	20	4173440	51791800	8314480	5625400
46.8	0	4020	200	531690	65355750	12434951	9574912
	10	3660	200	459990	56492250	10748532	8150633
	20	3600	200	444820	54612500	10390880	7518460
	30	3300	200	363800	44567500	8479662	5654574
77.4	0	3780	60	807350	29963770	6948185	5836475
	10	3120	60	710910	26401720	6122195	5064516
	20	1560	60	320100	11875050	2753660	2173579
	30	3660	60	586580	21694800	5030725	3659658
133.4	0	2340	200	271980	33354000	8329281	5414033
	10	2580	200	306990	37664250	9405652	6020793
	20	2520	200	276690	33893250	8463944	5169779
	30	2520	200	297910	36545750	9126336	5137365

For 133.4 MeV run, a 19 mm thick Cu plate was placed after the ^{7}Li target to stop the escaping protons. Attenuation of the neutron beam in the target was taken into account. The attenuation of neutron beam in the ^{7}Li target itself is quite negligible, ranging from 1 to 2%. On the other hand, the attenuation of the neutron beam in the 43 m of air column is

substantial (10 - 27 %) and is taken into consideration. The attenuation values of the neutron beam at different energies are given in Table 4-3.

Table 4-3 : Transmission Coefficients of the Neutron Beam

Neutron Energy En (MeV)	Transmission Coefficients of the Neutron Beam			
	in ^{7}Li Target	in Cu (19 mm)	in 43 m of air	Total (T)
25.75	0.98	-	0.73	0.72
46.8	0.987	-	0.78	0.77
77.4	0.989	-	0.85	0.84
133.4	0.99	0.725	0.90	0.65

The total number of neutrons incident on the face of upper detectors of the telescope for different beam runs, taking into account the beam attenuation and the solid angle at different angles is given in the last column of Table 4-2.

4.1.2 Data Collection and Analysis Procedure

The telescope was put in the coincidence mode for data collection. Coincidence criteria require an event in either upper main detector and an event in either lower main detector. There were no hardware coincidence criteria put on the shields (except for 133.4 MeV runs), so all types of events are recorded. For 133.4 MeV runs, the shields between the D1A and D2A detectors were in anticoincidence with the main detectors to reject the escaping energetic recoil protons going from D1 to D2.

For each event, eight parameters were recorded; D1M, D1S, D1PSD, D2M, D2S, D2PSD, TOF and SPARE as described in chapter 3. Here the only difference is in the eighth parameter SPARE, which is not barometric pressure but beam time of flight (BTOF). An RF signal from the cyclotron is sent via RG58A cable to the "stop" of the

BTOF time-to-amplitude converter (TAC). When a signal is recorded in the D1, it sends a "start" to the BTOF TAC. The incident neutron energy can then be determined by the BTOF if the channel number corresponding to the gamma flash is known. Otherwise, only the peak beam region can be selected since the spread in beam-time-of-flight can be calculated using the energy loss in the target and the calibration of the BTOF TAC. The spread in BTOF is given in Table 4-4. The range of BTOF channels for 77.4 MeV given in the bracket is for 20 and 30 degree runs.

Table 4-4: Spread in Beam Time of Flight (BTOF)

E_n (MeV)	ΔE_n (MeV)	Δ BTOF (ns)	Δ BTOF (Channel #)
25.75	4.6	53.85	446
46.8	2.9	13.57	650
77.4	2.1	4.51	507 (253)
133.4	1.5	1.36	153

For data analysis, each run was subdivided into four files, corresponding to each of the mini-telescopes (A-A, B-B, A-B and B-A).

A. Event Selection

To get a good signal-to-background ratio, different cuts were imposed on different parameters for event selection as described in section 3.1.2:

1) BTOF criteria - Events with BTOF in the peak region were only accepted. For 46.8 MeV there are two peaks in the BTOF histogram (Fig. 4-2 b). The two peaks are separated by the cyclotron period (33 ns). Both peaks are taken for the analysis as the BIC corresponds to both of them. Stripper loop selection was 1/45, which corresponds to a separation of 1.5 μs between successive beam bursts. Therefore, one of the peaks was an escape peak from the stripper loop.

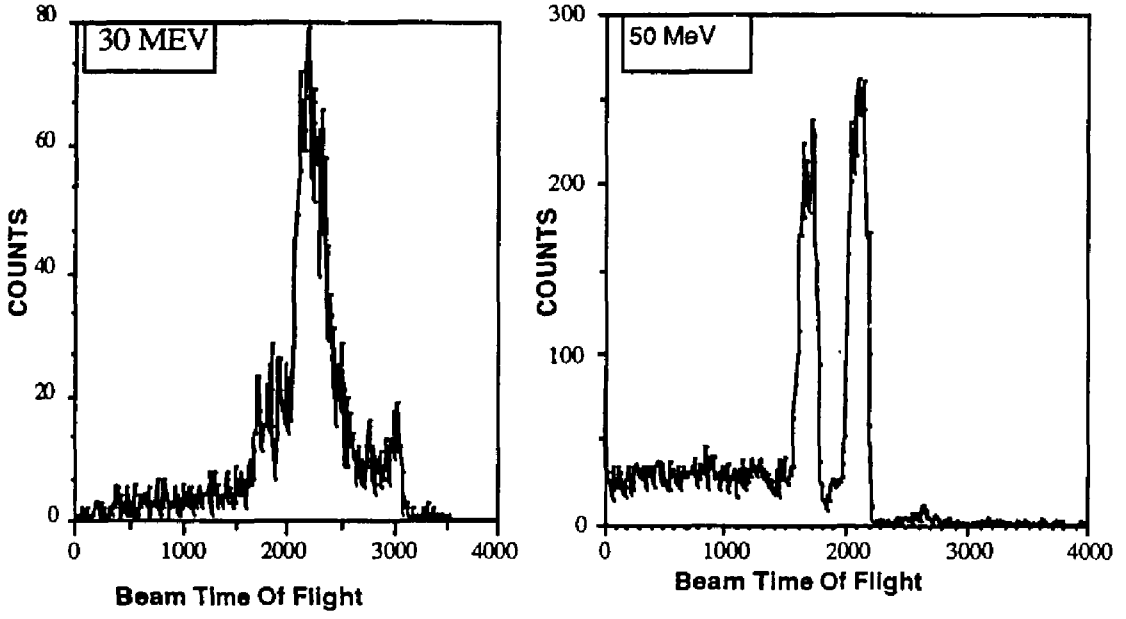

(a) (b)

Fig. 4-2 : Beam Time of Flight (BTOF) histogram; (a) 30 MeV, (b) 50 MeV.

2) Shield criteria - Events depositing energy in the shields (D1S or D2S channels greater than 5, corresponding to energy > 20 keV) are rejected.

3) Neutron TOF criteria : Walk correction for TOF vs D1M (Fig.4-3) was done for each file. After the walk corrections in TOF vs D1M, Gaussian curves were fitted to both upward and downward gammas in the TOF histogram. The zero time-of-flight channel (0 TOF) was taken to be the midpoint between upward and downward gamma TOF peaks (see Fig.4-4).

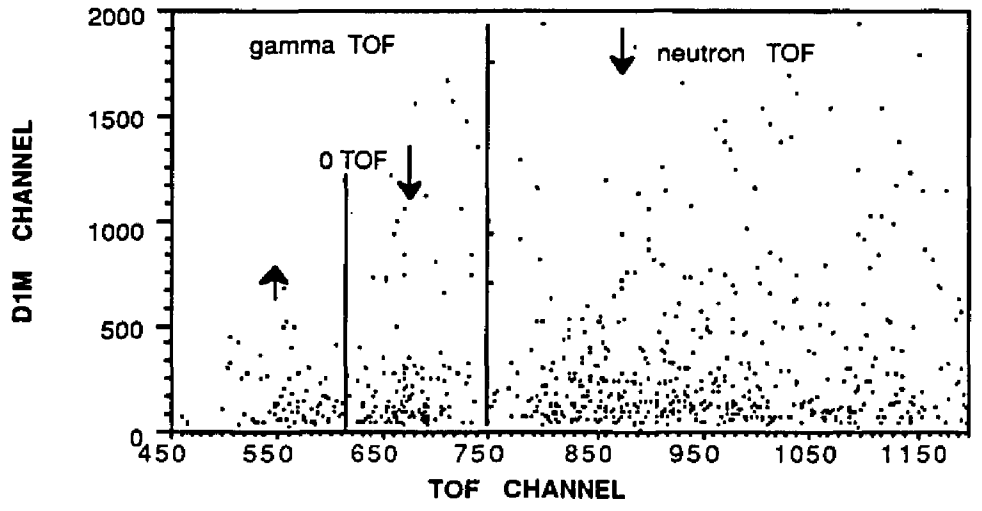

Fig. 4-3 : Walk Corrected TOF vs D1M (for 46.8 MeV run)

Events with gamma TOF are rejected and only downward moving neutron events are accepted for further analysis. The zero TOF reference is used later to calculate the energy of the scattered neutron (Eq. 4.7).

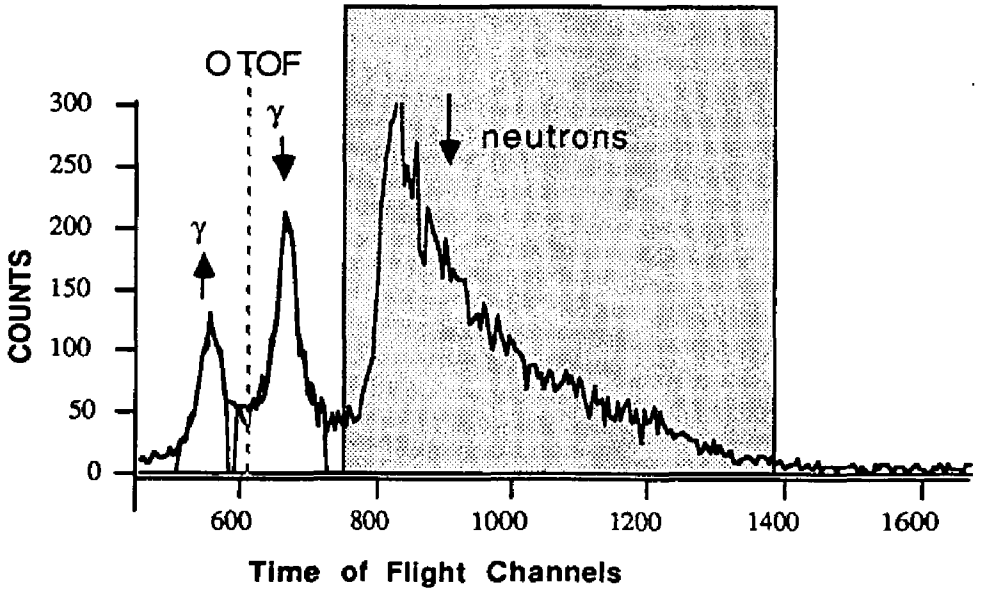

Fig. 4-4 : Histogram of walk corrected TOF (46.8 MeV)

4) Pulse Shape Discrimination Criteria (D1PSD & D2PSD): Walk corrections are done for D1M vs D1PSD (see Fig. 4-5) and for D2M vs D2PSD. Events with gamma (electron) PSD, both in D1PSD and D2PSD, are rejected in the analysis. D2PSD criteria are taken so as to minimize induced gamma ray effects.

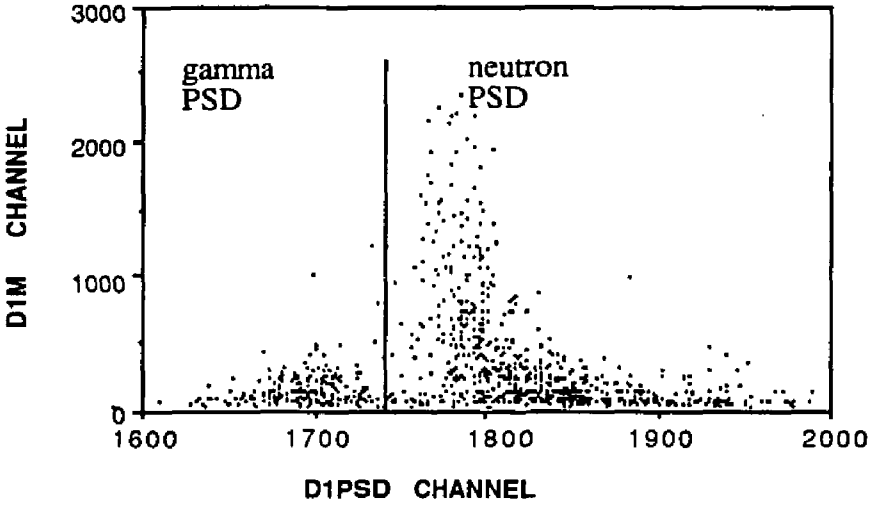

Fig. 4-5: Walk corrected D1PSD vs D1M (46.8 MeV)

5) Threshold Criteria : There is low energy noise present due to electronics cross talk. A hardware threshold (Constant Fraction Discriminator threshold) takes away most of this noise. We have only accepted events which deposit more than 0.5 MeV_{ee} (electron equivalent) energy in both the upper and lower detectors, thus reducing the background rate.

Events after all the cuts have been made are called "good neutron events", and are used for further analysis to estimate the light response function for BC519 and the efficiency of the telescope.

B. Energy Calibration

The time-of-flight (TOF) TAC was calibrated using an electronic pulser and a delay box. TOF channel numbers for different delays were measured. The TOF calibration was determined to be 51 ps/channel (Fig. 4-6).

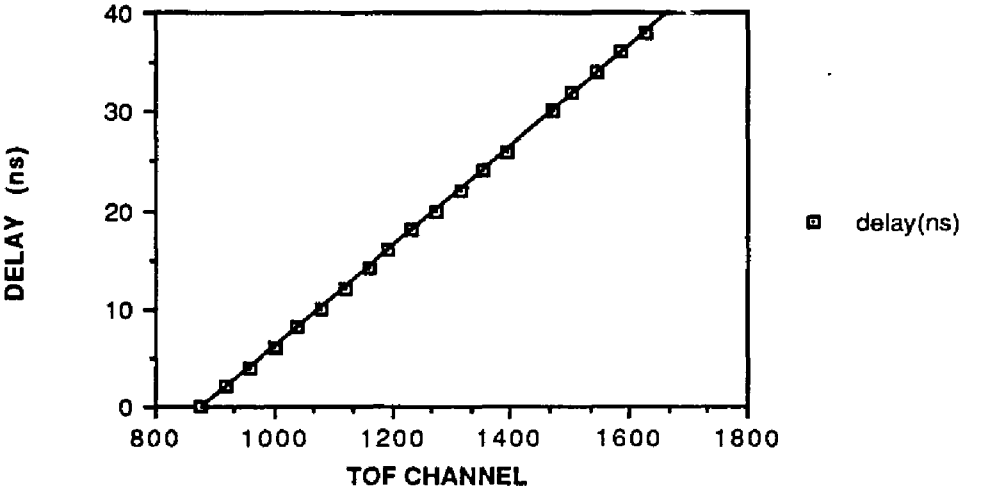

Fig. 4-6 : TOF TAC calibration

The energy of the scattered neutron ($E_{n'}$) for the relativistic case (Eq. 3.1) becomes

$$E_{n'} = m_n c^2 \left(\frac{1}{\sqrt{1 - \left(\frac{(L/c)}{(TOF - 0\,TOF) \times 0.051} \right)^2}} - 1 \right) \qquad (4.7)$$

where TOF is in channel number. The TOF channel number is 0 TOF, for simultaneous events in the upper and lower detectors, which are separated by a distance of L cm and c is the speed of light.

The light response of a scintillator is not a linear function of energy if the energy is deposited by heavily ionizing particles such as protons, deuterons, alphas and heavy recoil nuclei as described in chapter 2. The pulse height response for gamma rays is directly proportional to the energy deposited. Using the calibration of pulse height channels

obtained with radioactive gamma ray sources and cosmic ray muons, the D1 pulse height (D1M) channels were converted to their electron equivalent energy - T_e (MeV_{ee}). In the scatter plot of recoil proton energy in the upper detector (Te) vs scattered neutron energy $E_{n'}$ (Fig. 4-7), region A corresponds to the single elastic scattered events, region B contains multiply scattered elastic events and region C contains carbon interactions.

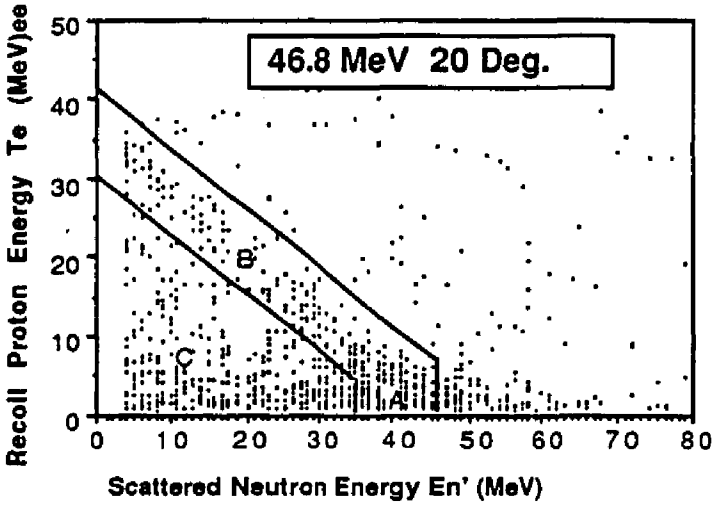

Fig. 4-7: Scatter Plot of Recoil Proton electron equivalent energy Te (MeV)ee vs Scattered neutron energy En'(MeV) for 46.8 MeV 20 deg. run.

Single scatter events from the scatter plots of T_e vs $E_{n'}$ (region A in Fig. 4-7) and the position of the centroid of multiply scattered event distribution (region B in Fig. 4-7) were used to determine the light response function of BC519. We find that proton light output assembled from several IUCF data runs closely follows the light output curve of NE228. In Fig. 4-8 the light response for some of the single elastic scattered events (region A in Fig. 4-7) is superimposed on NE228 light response curve and shows good agreement. The advantage of correlating the response of this scintillator (BC519) to that of NE228 is that the proton light output of NE228 has been well studied at low energies where we have no data.

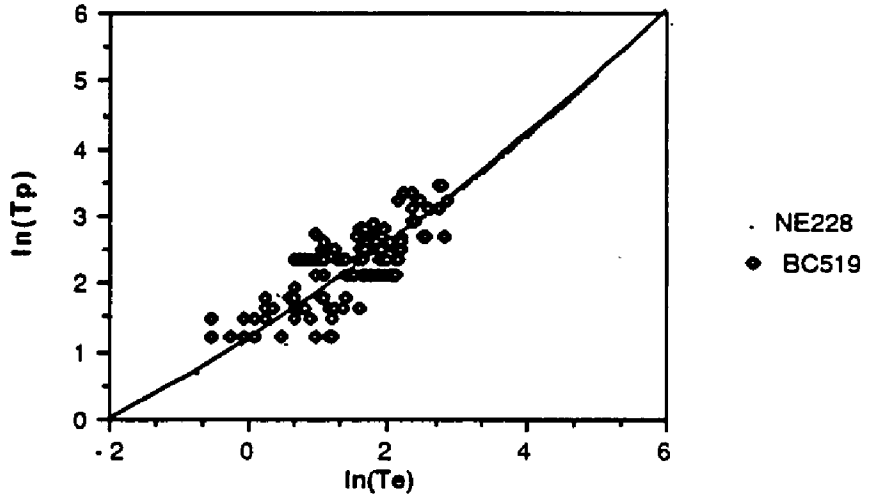

Fig. 4-8 : Light Response of BC519 in comparison to NE228

The light response function for NE228 (Madey et al, 1978) is :

$$Tp = \exp(1.1826 + 0.64691 \ln(Te) + 0.02704 [\ln(Te)]^2), \qquad (4.8)$$

where T_p is the recoil proton energy in MeV and T_e is the electron equivalent energy in MeV that gives the same light output.

As the light response for alphas is different than that for protons, they will contribute to the low energy noise (region C in Fig. 4-7). The PSD separation between protons and alphas is not very good for this scintillator, so this noise cannot be safely rejected.

For the good neutron events (described in section A), the pulse height of upper detectors (D1M) is converted into proton recoil energy (Eq.4.8), and the TOF is converted into the scattered neutron energy (Eq. 4.7.) in order to calculate the total neutron energy (Eq. 2.1) and the scatter angle (Eq. 2.2) of the incident neutron .

C. Resolution Parameters of the Telescope

1) Energy Resolution

The response of the neutron double scatter telescope to a monoenergetic neutron beam is not a δ-function in energy, but shows a definite energy distribution with a broad peak at the incident neutron energy E_o and a continuous background at lower energies (Fig. 4-9). The energy resolution (R) is defined as the full width at half maximum (FWHM) of the peak divided by the location of the peak centroid E_o :

$$R = \frac{FWHM}{E_o}.$$

Semiconductor diode detectors can have an energy resolution <1%, whereas the range for the scintillation detectors is 5-10% (Knoll, 1989). The energy resolution of the telescope is

$$\frac{\Delta E_n}{E_n} = \left(\frac{\Delta E_p + \Delta E_{n'}}{E_n}\right),$$

where ΔE_p is the energy resolution of the upper detector and $\Delta E_{n'}$ is the energy resolution of the scattered neutron. The fluctuations in the signal, which give rise to the broadening of the peak (ΔEp) can be due

a) drift of the signal due to the gain changes of photomultiplier tubes;

b) baseline noise within the detector and the electronics;

c) statistical noise arising from the discrete nature of the measured signal and

d) variations in the detector response over its active volume.

The third factor, the fluctuations due to the statistical noise, is one of the more important factors in the energy resolution. The statistical noise arises from the fact that the charge Q generated within a PMT by a scintillation is not a continuous variable but represents a discrete number of charge carriers (number of electrons emitted at the photocathode). It is assumed that the formation of each charge carrier is a Poisson process, so that if the total number of charge carriers is N, a standard deviation $\sigma = \sqrt{N}$ characterizes the inherent

statistical fluctuation in that number. As the light response of the scintillator is a linear function of electron equivalent energy T_e, then $\sigma \propto \sqrt{T_e}$.

The energy resolution of the scattered neutron is determined both by the uncertainty in the distance measurements (ΔL) and by the uncertainty in the time of flight measurements,

$$\frac{\Delta E_{n'}}{E_{n'}} = 2\left(\frac{\Delta L}{L} + \frac{\Delta t}{t}\right),$$

where L is the distance travelled by the neutron in time t. The uncertainty ΔL in the distance L is due to the finite thickness of the detectors. Δt is the uncertainty in the TOF measurements due to the electronics. It was measured to be < 2 ns (FWHM for the gamma peak). For the low energy scattered neutrons, the major factor in the energy resolution is due to the uncertainty in the distance (~ 28%), but as the energy of the scattered neutron increases, TOF resolution starts playing a larger role (TOF ~ 6 ns for a scattered neutron of energy 100 MeV).

The energy resolution for 46.8 MeV incident neutrons at an angle of 20 deg. is estimated to be ~ 28 % (Fig. 4-9) from IUCF measurements.

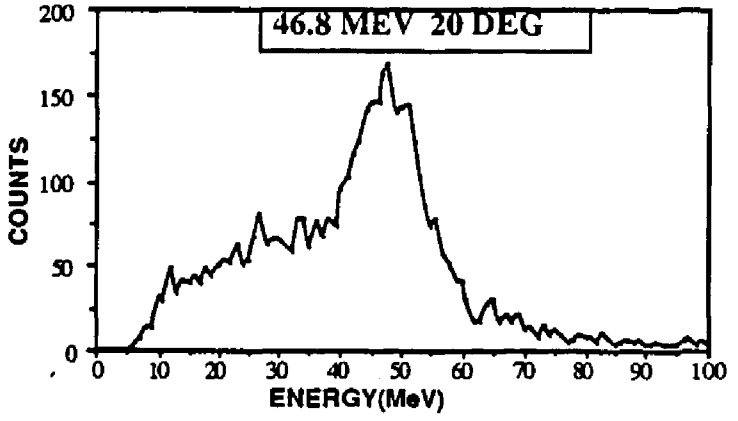

Fig. 4-9: Energy Resolution from IUCF calibration for 46.8 MeV 20 degree run, integrated for all scatter angles.

2) Angular Resolution

The direction of a incident neutron can be determined to lie on the surface of a cone centered on the scattered neutron direction. As the scattered neutron direction is given by the interaction location in the upper and lower detector, spatial resolution within each detector volume will largely determine the angular resolution. In our case, we can only determine the interaction within the confines of the detector, which will already give an uncertainty of $\pm$ 8 deg. for a vertical mini-telescope. We assume the calculated scatter angle to be the zenith angle within the uncertainty of the detector volume.

The scatter angle is determined from the energy and TOF measurements. Therefore, the energy resolution will also determine the angular resolution of the telescope. The angular HWHM for 46.8 MeV neutron, incident at an angle of 20 degrees is measured to be ~ 5 degrees (Fig. 4-10).

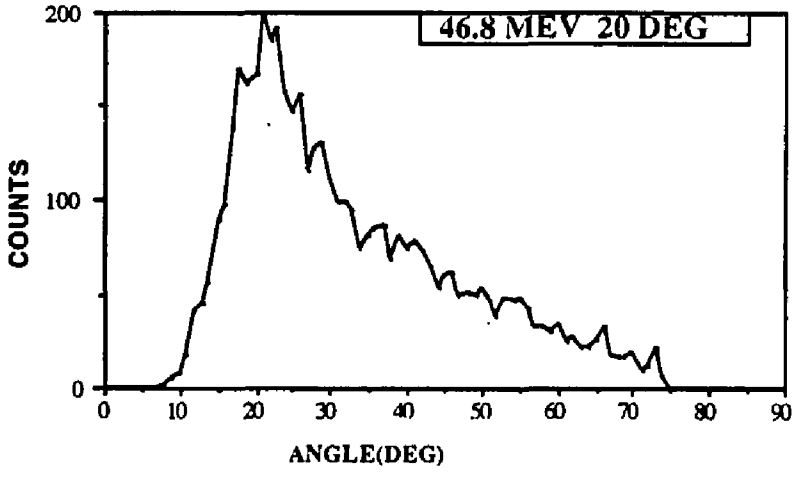

Fig. 4-10: Angular Resolution of the telescope for 46.8 MeV and 20 deg. run.

4.1.4 Efficiency Measurements

The efficiency of the telescope $\varepsilon(E_n,\theta)$ is defined as the ratio of the number of detected neutrons (n) to the number of neutrons (N) incident on the telescope. The

efficiency is a function of neutron's energy (E_n) and its angle of incidence (θ)with respect to the telescope axis,

$$\varepsilon(E_n,\theta) = \frac{n}{N}. \qquad (4.9)$$

After all the cuts have been made as described in the section A and energy calibrations applied to the data, a uniform noise was evident in the D2M vs. En' scatter plots for scattered neutron energies < 4 MeV. Therefore, an additional cut was imposed on the scattered neutron energy, which rejected events where $E_{n'} < 4$ MeV. The incident neutron's calculated energy vs scatter angle is plotted in Fig. 4-11 for the 46.8 MeV, 20 degree run. The events were then binned into energy and angle bins for the efficiency determination.

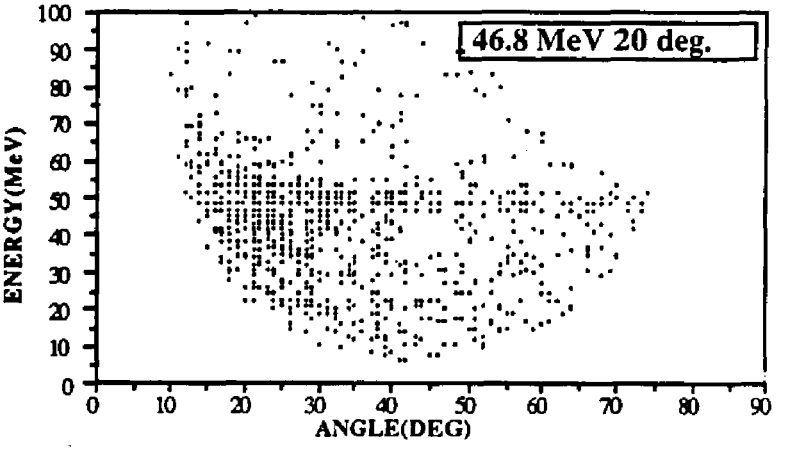

Fig. 4-11: Scatter Plot of calculated energy vs calculated scatter angle for 46.8 MeV and 20 deg. run.

Efficiency matrices in energy and angle bins for 20 deg runs are given in Table 4-5 (for 25.8 MeV), Table 4-6 (for 46.8 MeV), Table 4-7 (for 77.4 MeV) and in Table 4-8 (for

133.4 MeV). The highlighted cells indicate the bin of incident neutrons. Only statistical errors are taken into account as their contribution is maximum compared to the others.

Table 4-5: Efficiency Matrix for 25.8 MeV and 20 deg. run (A-A)

Angle (deg.)	Efficiency · 10^-4					
	Energy bins (MeV)					
	10≤ E< 20	20 ≤ E<40	40 ≤E<60	60≤E<100	100≤E<170	170≤E<200
0≤θ< 5	0	0	0	0	0	0
5≤θ<15	0	0.01±0.01	0.0±0.01	0	0	0
15≤θ<25	0.08±0.01	1.02±0.04	0	0	0	0
25≤θ<35	0.36±0.03	0.79±0.04	0	0	0	0
35≤θ<45	0.32±0.02	0.38±0.03	0	0	0	0
45≤θ<55	0.17±0.02	0.28±0.02	0	0	0	0
55≤θ<65	0	0.22±0.02	0	0	0	0
65≤θ<75	0	0.03±0.01	0	0	0	0
75≤θ<85	0	0	0	0	0	0
85≤θ<90	0	0	0	0	0	0

Table 4-6: Efficiency Matrix for 46.8 MeV and 20 deg. run (A-A)

Angle (deg.)	Efficiency × 10^-4					
	Energy Bins (MeV)					
	10≤ E< 20	20 ≤ E<40	40 ≤E<60	60≤E<100	100≤E<170	170≤E<200
0≤θ< 5	0	0	0	0	0	0
5≤θ<15	0	0	0.08±0.01	0.14±0.01	0.04±0.01	0
15≤θ<25	0.01±0.01	0.49±0.03	1.32±0.04	0.22±0.02	0.06±0.01	0.01±0.01
25≤θ<35	0.15±0.01	0.48±0.03	0.73±0.03	0.09±0.01	0.07±0.01	0.01±0.01
35≤θ<45	0.21±0.02	0.28±0.02	0.34±0.02	0.10±0.01	0.04±0.01	0
45≤θ<55	0.16±0.01	0.21±0.02	0.21±0.02	0.08±0.01	0	0
55≤θ<65	0.03±0.01	0.18±0.02	0.16±0.01	0.03±0.01	0	0
65≤θ<75	0	0.05±0.01	0.14±0.01	0.01±0.01	0	0
75≤θ<85	0	0	0	0	0	0

85≤θ<90	0	0	0	0	0	0

Table 4-7: Efficiency Matrix for 77.4 MeV and 20 deg. run (A-A)

Angle (deg.)	Efficiency × 10^-4					
	Energy Bins (MeV)					
	10≤ E< 20	20 ≤ E<40	40 ≤E<60	60≤E<100	100≤E<170	170≤E<200
0≤θ< 5	0	0	0	0	0	0
5≤θ<15	0	0	0	0.03±0.01	0.01	0
15≤θ<25	0	0.03±0.01	0.13±0.02	0.26±0.03	0.02±0.01	0
25≤θ<35	0.01±0.01	0.06±0.02	0.08±0.02	0.14±0.03	0.02±0.01	0
35≤θ<45	0.03±0.01	0.05±0.02	0.05±0.02	0.06±0.02	0.01±0.01	0
45≤θ<55	0.02±0.01	0.02±0.01	0.04±0.01	0.06±0.02	0	0
55≤θ<65	0.01±0.01	0.03±0.01	0.03±0.01	0.02±0.01	0	0
65≤θ<75	0	0.01±0.01	0.02±0.01	0.02±0.01	0	0
75≤θ<85	0	0	0	0	0	0
85≤θ<90	0	0	0	0	0	0

Table 4-8: Efficiency Matrix for 133.4 MeV and 20 deg. run (A-A)

Angle (deg.)	Efficiency x 10^-4					
	Energy Bins (MeV)					
	10≤ E< 20	20 ≤ E<40	40 ≤E<60	60≤E<100	100≤E<170	170≤E<200
0≤θ< 5	0	0	0	0	0	0
5≤θ<15	0	0	0	0.03±0.01	0.06±0.01	0
15≤θ<25	0	0	0.03±0.01	0.08±0.01	0.11±0.01	0.01±0.01
25≤θ<35	0.01±0.01	0.02±0.01	0.02±0.01	0.04±0.01	0.10±0.01	0.01±0.01
35≤θ<45	0.01±0.01	0.01±0.01	0.02±0.01	0.05±0.01	0.05±0.01	0
45≤θ<55	0.01±0.01	0.01±0.01	0.02±0.01	0.05±0.01	0.04±0.01	0
55≤θ<65	0.01±0.01	0	0.01±0.01	0.03±0.01	0.01±0.01	0
65≤θ<75	0	0.01±0.01	0.01±0.01	0.04±0.01	0	0
75≤θ<85	0	0	0	0	0	0

85≤θ<90	0	0	0	0	0	0

The Response Matrix elements in the 15 to 25 degree interval for 20 deg runs are shown below in Table 4-9.

Table 4-9: Response function in energy for 20 deg.(A-A)

Energy (MeV)	Efficiency ε (ΔE,Δθ) x 10^-4			
	20 ≤ E < 40	40 ≤ E < 60	60 ≤ E < 100	100 ≤ E<170
20 ≤ E < 40	1.02±0.04	0	0	0
40 ≤ E < 60	0.49±0.03	1.32±0.04	0.22±0.02	0.06±0.01
60 ≤ E ≤100	0.03±0.01	0.13±0.02	0.26±0.03	0.02±0.01
100 ≤ E<170	0	0.03±0.01	0.08±0.01	0.11±0.01

For the 46.8 MeV 20 deg. run, we normalize the efficiency matrix to the incident (ΔE, Δθ) bin (40 to 60 MeV bin in energy and 15 to 25 deg. in angle) so as to compare the fraction of events spilling over into the other energy and angle bins (see Table 4-10). This helps in comparing the measured efficiency with the response function calculated by Monte Carlo methods as described in the following section.

Table 4-10: Normalized 46.8 MeV 20 deg. run (A-A)

Angle (deg.)	Efficiency x 10^-4					
	Energy Bins (MeV)					
	10≤ E< 20	20 ≤ E<40	40 ≤E<60	60≤E<100	100≤E<170	170≤E<200
0≤θ< 5	0	0	0	0	0	0
5≤θ<15	0	0	0.06±0.01	0.11±0.01	0.03±0.01	0
15≤θ<25	0.01±0.01	0.37±0.03	1.0±0.06	0.17±0.02	0.05±0.01	0.01±0.01
25≤θ<35	0.11±0.01	0.36±0.03	0.55±0.04	0.07±0.01	0.05±0.01	0
35≤θ<45	0.16±0.02	0.21±0.02	0.26±0.02	0.08±0.01	0	0
45≤θ<55	0.12±0.01	0.16±0.02	0.16±0.02	0.06±0.02	0	0
55≤θ<65	0.02±0.01	0.14±0.02	0.12±0.01	0.02±0.01	0	0

65≤θ<75	0	0.04±0.01	0.11±0.01	0	0	0
75≤θ<85	0	0	0	0	0	0
85≤θ<90	0	0	0	0	0	0

Efficiency measurements from the other vertical mini-telescope B-B are similar to those of the A-A telescope and the values for the corresponding energy and angle bins are shown in the Fig. 4-12 for all beam angles. The inclined mini-telescopes (A-B and B-A) are corrected for solid angle difference from the vertical cells and their values are also plotted in Fig. 4-12. The axis of inclined telescopes is ~ 35 deg. off the vertical axis, so the angle with respect to the neutron beam will differ. For A-B these values are 35, 45, 55 and 65 deg., while for B-A they are 35, 25, 15 and 5 degrees.

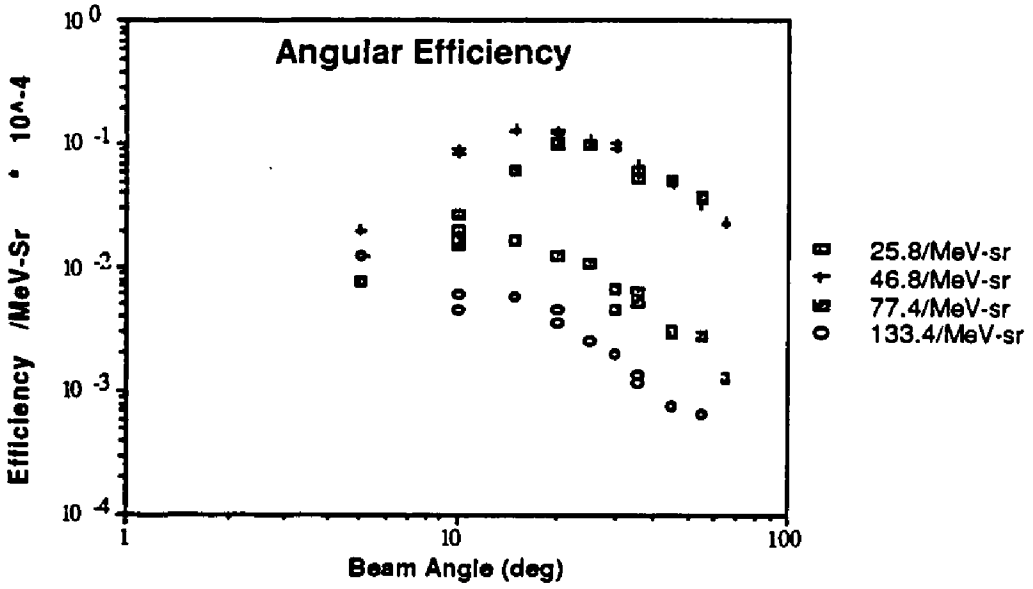

Fig. 4-12: Efficiency from all the mini-telescopes as a function of angle between the incident neutron beam direction and the telescope axis.

The efficiency is low for angles less than 20 deg. because of the 2 MeV proton equivalent energy threshold. Lowering the threshold will increase the efficiency for these angles. The agreement between the various mini-telescopes is good for any given energy.

4.2 Monte Carlo Calculation

A modified Monte-Carlo code based on the original neutron code of Stanton (1971) and a Monte Carlo Code of O'Gorman from IBM corporation (1990) were used to calculate the efficiency and response of the telescope. Monte Carlo calculations provide greater flexibility in determining the response of the telescope for any energy and angle distribution.

In the calculations using the modified Stanton code, energy, zenith angle and total number of incident neutrons were given as initial parameters of the calculation. Only double scattered events are recorded, for one vertical mini-telescope. Both n-p scattering and n-C scattering reaction (elastic and inelastic) are included in the code. Neutrons can undergo multiple scattering with the maximum number of scatters in both D1 and D2 being controlled. The average number of multiple scatters was found to be ~ 2. Attenuation of the incident and scattered neutron beam due to the shields and the aluminium walls of detector is taken into account in the code. Interactions giving rise to gammas are rejected, as in our data analysis procedure. Gamma TOF and gamma PSD signals in D1 and D2 are rejected. Threshold criteria are also imposed, similar to those made in hardware at IUCF (T_e = 0.5 MeV). Energy deposited from each reaction is converted into its electron equivalent energy and then summed within any given detector. The light response function for NE228 (Madey et al. 1979)is used to convert the light output from BC519 into the recoil proton energy. As alphas are not rejected in the data analysis due to poor PSD resolution, alphas are included here contributing to low energy noise. The code was run for 1 million input neutrons for various energies and angles. The total energy of the incident neutron and its scatter angle were calculated using the recoil proton energy in D1 and the scattered neutron energy (Eq. 2.1 and Eq. 2.2). Events were then binned in the energy vs. angle bins as

with the IUCF data analysis. Results for 20 deg. runs are compared with the IUCF measurements and are shown in Fig. 4-13. Plotted are the diagonal elements of this response matrix.

The code produced by O'Gorman (1990) simulates the full configuration of the telescope which includes the inclined telescopes. Incident neutrons can be either monoenergetic from a given direction simulating a beam or can conform to a distribution in energy and angle. This method was used for flux calculation, which is described in chapter 5. Monoenergetic beams with the same energy resolution as IUCF (see Table 4-1) were used in the calculations. Results for 20 deg. runs are compared with other measurements in Fig. 4-13. Correction for attenuation by passive telescope components were performed after the computer calculations.

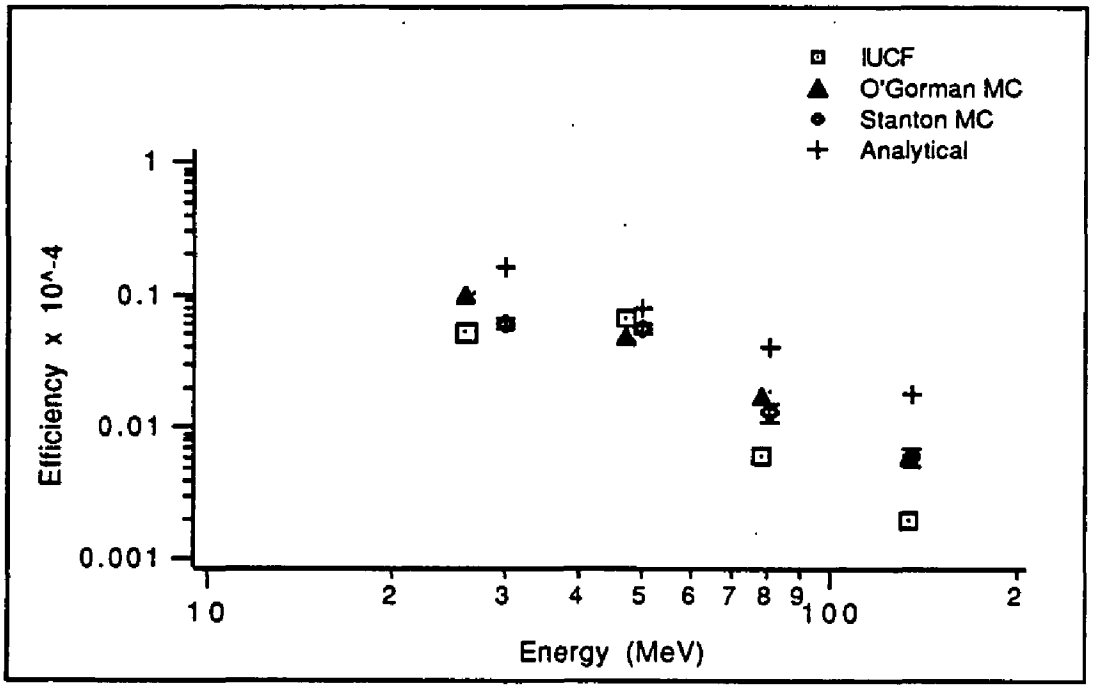

Fig. 4-13: Efficiency for 20 deg. runs in single (E, θ) bin corresponding to the input beam from the IUCF calibration , Monte Carlo Calculations and analytical calculations.

The normalized response for 46.8 MeV run at 20 deg. is shown in Table 4-11. The shapes or distribution of the response of the telescope agrees with the IUCF measurements (Table 4-10) taking into account the high accidental rate at IUCF, which was ~ 1 count/sec.

Table 4-11: Normalized Response for 46.8 MeV 20 deg.from O'Gorman's Monte Carlo calculations (A-A)

Angle (deg.)	Efficiency x 10^-4 Energy Bins (MeV)					
	10≤ E< 20	20 ≤ E<40	40 ≤E<60	60≤E<100	100≤E<170	170≤E<200
0≤θ< 5	0	0	0	0	0	0
5≤θ<15	0	0	0.31±0.07	0.02±0.01	0.01±0.01	0
15≤θ<25	0.01±0.01	0.21±0.06	1.00±0.18	0.02±0.01	0	0
25≤θ<35	0	0.34±0.08	0.43±0.09	0.01±0.01	0	0
35≤θ<45	0.01±0.01	0.25±0.06	0.06±0.03	0.02±0.01	0	0
45≤θ<55	0.05±0.02	0.36±0.08	0.03±0.02	0.01±0.01	0	0
55≤θ<65	0.05±0.02	0.22±0.06	0.02±0.01	0	0	0
65≤θ<75	0	0.08±0.03	0.02±0.01	0	0	0
75≤θ<85	0	0	0	0	0	0
85≤θ<90	0	0	0	0	0	0

The efficiency of the telescope can be approximately calculated analytically by finding the probabilities of the neutron interaction in the upper and lower detectors. The results of the analytical calculations (20 deg) for only single n-p elastic scattering (both in the upper and in the lower detector) with all the attenuations in the shields, aluminium and in the scintillator are also plotted in Fig. 4-13. These analytical estimates are, as a rule, overestimates of detector efficiencies.

The IUCF measurements agree in magnitude with the Monte Carlo calculations for 25.75 MeV and 46.8 MeV but are lower for 77.4 MeV and 133.4 MeV by a factor of two. At higher energies the count rate for the telescope was high and dead time problems arising from an underestimated software configuration probably reduced the number of detected

events by an unknown amount. The accidental rate at IUCF was also quite high ~10%, which does not correspond to the accidental rate in field measurements (~1 - 2%). We conclude that the O'Gorman Monte Carlo calculations agree quite well with our calibration data in shape and can be used in estimating the neutron flux.

CHAPTER 5

OBSERVATIONS AND ANALYSIS PROCEDURE

Ground level atmospheric neutron measurements were done at three different locations in U.S.A: Leadville, Colorado; Boulder, Colorado, Mt. Washington and Durham, New Hampshire. These locations were chosen so that we could have different altitudes for similar rigidity values. Both measurements in Colorado were performed inside buildings, where the temperature and humidity were controlled. The Durham and Mt. Washington measurements were performed inside a truck modified to control temperature and humidity. At all locations, the pressure was continuously recorded by a precision digital barometer. The temperature was recorded at the start and at the end of each run . The efficiency of the neutron double scatter telescope is low and the intrinsic flux of neutrons is also low, therefore measurements at each location were done for at least 10 days. In Durham, which is at sea level, measurements were done for one month. Specifications for each site are described in section 5.2.

5.1 Data Collection Procedure

Before each neutron run, the gains of the Photomultiplier tubes (PMTs) for each detector were measured using radioactive gamma ray sources (^{60}Co, ^{88}Y, ^{241}Am/Be). Naturally occurring gamma ray emitting isotopes (^{40}K, ^{228}Th), which are products of radioactive decay of uranium and its daughters were also used for the calibration. Specifications of the radioactive gamma ray sources are given in the Table 5-1. Light emitting diodes (LEDs) in each detector were also used for a quick check of individual PMTs. Power to the LEDs and PMTs was controlled by software. Cosmic ray muons were

also used in the energy calibration to obtain a high energy point (~ 22 MeV_{ee}). Muons are minimum ionizing particles which deposit 2 MeV/g-cm^2 in the detectors. Muon runs were also used for TOF and PSD walk corrections.

Table 5-1: Radioactive Gamma ray Sources

Sources	Half-life	Energy of the gamma ray (MeV)
^{60}Co	5.27 y	1.117 1.332
^{88}Y	106.6 d	0.896 1.836
^{40}K	1.28×10^9 y	1.461
^{208}Tl (from ^{228}Th)	3 m (1.9 y)	2.614
$^{241}Am/Be$	433 y	4.43

The telescope can be operated in many coincident modes as described in chapter 3. To check PMT gains, it was operated in the *singles mode*, i.e. non-coincident events occurring in either of the detectors were recorded. For *muon runs*, the telescope was operated in the *coincident mode* i.e. the hardware requires a coincidence between any upper and lower detectors as well as fulfilling the coincidence requirement of the upper shields of the upper detectors and the lower shields of the lower detectors. The flux of cosmic ray muons is much higher than the flux of neutrons at the ground level. Therefore, for the *neutron runs* the upper shield of the upper detector and the lower shield of the lower detector were in anticoincidence with the main detectors in order to reject cosmic ray muons. The gamma ray background was not eliminated by the hardware, but is rejected in the analysis by using TOF and PSD as described in the section 5.3.

Each run was carried out for ~ 24 hrs or more. After each run, the PMTs gains were again checked. All files were stored on floppy diskettes and a 60 MB cartridge tape. In the data analysis those runs with large fluctuations in temperature or pressure were ignored .

5.2 Observation Sites

The neutron measurements discussed here were performed at Leadville, Colorado; Boulder, Colorado; Mt.Washington, New Hampshire and Durham, New Hampshire. The geophysical parameters of each observation site are given in the Table 5-2. Vertical cutoff rigidity values are calculated using geomagnetic field coefficients (Smart and Shea, 1987). For our measurememnts, we have used their calculated values for 1985.

Table 5-2: Data on Observation sites

Site	Altitude (m)	Atmospheric depth (mb)	Geographic		Geomagnetic		Cutoff Rigidity (GV)
			latitude	longitude	latitude	longitude	
Leadville	3109	691	39.10N	106.20W	48.05N	43.93W	2.97
Boulder	1655	835	40.01N	105.17W	48.89N	43.00W	2.90
Mt. Washington	1850	817	44.16N	71.18W	55.77N	2.33W	1.43
Durham	24	1010	43.08N	70.56W	54.57N	1.71W	1.61

Leadville, Colorado

Leadville, a former mining town, is located at an altitude of 10200 ft (~ 3 km) in central Colorado. The telescope was placed in a small building with brick walls and a wooden roof. As the measurements were taken in winter, snow was regularly removed

from the roof. This was necessary because snow attenuates the neutron flux. The temperature was maintained inside the building to within $\pm$ 4° F. Observations were taken from 18 to 28 of February and from 3 to 7 June 1987. The average barometric pressure was 691 mb and the average temperature was 74° F. A total of 251 hr (~ 10.5 days) of data were collected (excluding the gamma ray calibration runs). The average rate of raw events in the neutron mode for the full telescope was 0.6 counts/sec (muon rate is ~ 5 counts/sec). Only ~ 3% of the raw events were good neutron events used for analysis. For either vertical mini-telescope, the neutron count rate was ~ 4.4×10^{-3} counts/sec. The count matrix for the Leadville runs is tabulated in Table 5-3.

Boulder, Colorado

Boulder is situated at a height of 5430 ft (~ 1.6 km) at the base of the Rocky Mountains in Colorado. The telescope was set up inside a single story building with a corrugated steel roof. Temperature was maintained at 72° F and the average barometric pressure was 835 mb. Data were collected from 13 July until 19 August 1987. A total of 832 hr (~34 days) of data were collected. The average raw data rate for neutron runs was ~ 0.4 counts/sec for the full telescope, which was ~ 33% less than Leadville. For vertical mini-telescopes the good neutron count rate was ~ 1.4×10^{-3} neutrons/sec, ~ 2% of the raw events. The count matrix for Boulder is given in Table 5-4.

Mt.Washington, New Hampshire

Mt. Washington summit is at a height of 6072 ft (1.85 km) in the White mountains of New Hampshire. The telescope was placed in a rented truck. The truck was insulated and the temperature inside was regulated. The truck was parked in an open space away from the main summit buildings. Data were collected from 27 August until 18 of September 1987. The average pressure was 817 $\pm$ 8 mb and the temperature was maintained at 72° F.

We had problems with power cable which had shut the air conditioner had shut off. The temperature variations for those runs was ~ 30° F and they are not used for analysis. We also had problems with the high voltage supply, which caused large variations in the gain of Photomultiplier tubes. Therefore, only part of the data set is used for analysis which was error free. A total of ~ 200 hr (~ 8 days) of data for one vertical telescope (B) was used for analysis. The average raw count rate for full telescope was 0.4 counts /sec. For vertical minitelescope the good neutron count rate was ~ 2.01×10^{-3} neutrons /sec (~ 1% of the raw events). The count matrix for Mt. Washington is given in Table 5-5.

Durham, New Hampshire

Durham, New Hampshire is located near sea level. Here, the telescope was placed inside a rented truck. The truck was insulated and temperature was maintained using a thermostatically controlled heater, air conditioner and a dehumidifier. It was parked away from large masses in order to minimize the effect of scattered neutrons. The elevation is 80 ft (24.4 m). Data were collected from 20 September until 19 October 1987, for a total of 617 hr (~ 26 days). The average raw count rate for neutron runs was ~ 0.2 counts/sec, roughly 3 times less than the Leadville raw count rate. The good neutron count rate for vertical minitelescopes was ~ 0.4×10^{-3} counts/sec and was ~ 1% of the raw events. The count matrix for Durham is given in Table 5-6.

5.3 Data Analysis Procedure

The data analysis procedure for field runs was performed in a similar way as the IUCF data analysis. Each neutron run was corrected for walk in TOF and PSD vs Pulse height (see Fig. 5-1 and 5-2).

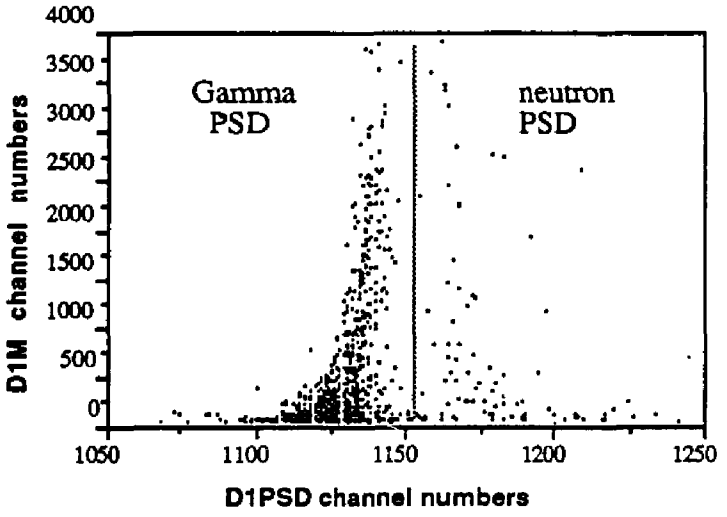

Fig. 5-1: Walk corrected D1PSD vs D1M for Leadville runs.

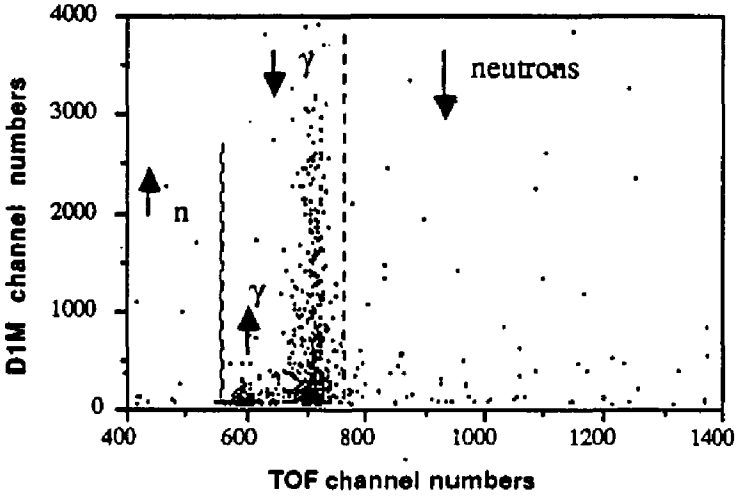

Fig. 5-2: Walk corrected TOF vs D1M for Leadville runs.

In the TOF histogram (Fig. 5-3), upward and downward moving gamma rays were fitted to Gaussian curves to obtain the TOF peak channel number. 0 TOF is taken to be the midpoint between upward and downward moving gamma ray peaks.

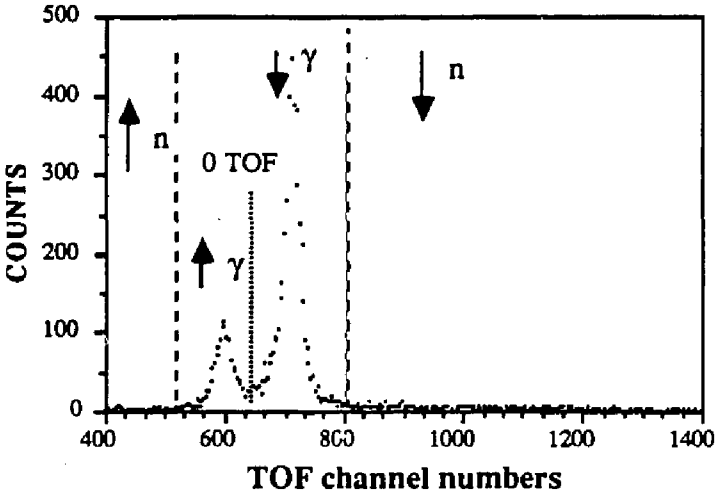

Fig.5-3: Histogram of walk corrected TOF for Leadville runs.

The background count rate for the neutron runs was reduced by applying the following criteria in data analysis:

(1) All events depositing energy larger than the noise level (E > 20 keV) in the upper or the lower shields of either of the detectors were rejected;

(2) All upward moving events (neutrons and gamma rays) and downward moving gamma rays were rejected;

(3) All events having gamma PSD in either the upper or the lower detectors were also rejected.

After all the cuts, the pulse height in the upper detector was converted into the proton recoil energy equivalent (Eq. 4.8) and the TOF into the scattered neutron energy (Eq. 4.7) by applying the appropriate calibration values. The total energy of the incident neutron and its scatter angle is then calculated using Eq. 2.1 and Eq. 2.2. The scatter plot of the calculated neutron energy and the calculated scatter angle is shown in Fig. 5-4.

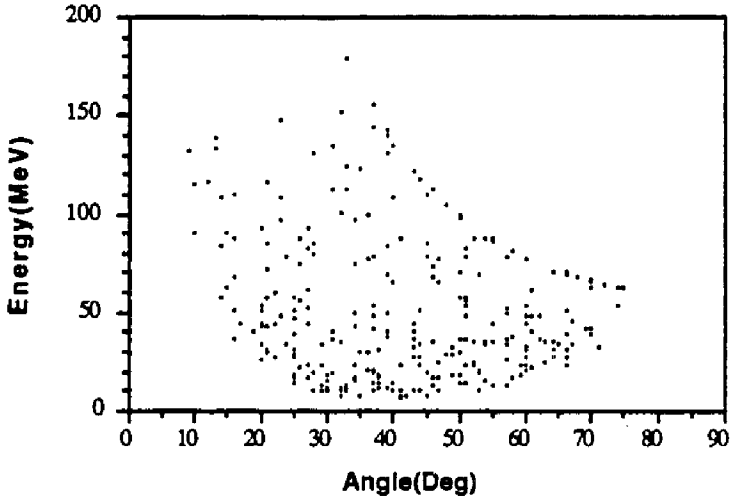

Fig. 5-4: Calculated neutron energy vs scatter angle of neutrons.

Events were binned into energy and scatter angle bins. Events from all the runs for a particular location are summed together to obtain statistics. We call the results the *counts matrix* which is then used to calculate the neutron flux as described in the following section. Count matrices for both the vertical mini-telescopes (A-A and B-B) were summed together, as their individual count matrices were similar. The count rate difference between the A-A and B-B telescopes was ~ 4%.The count matrices are given below for different observation sites.

Table 5-3: Leadville count matrix for both the vertical mini-telescopes ($\Delta t \sim 7$ days)

Angle	Energy bins (MeV)					
(deg.)	10≤E≤20	20≤E<40	40≤E<60	60≤E<100	100≤E<170	170≤E<200
0≤θ<5	0	0	0	0	0	0
5≤θ<15	0	0	20	71	56	0
15≤θ<25	14	179	177	248	113	0
25≤θ<35	219	317	202	213	122	12
35≤θ<45	311	326	205	191	116	1
45≤θ<55	286	284	174	209	26	0
55≤θ<65	85	311	150	116	0	0
65≤θ<75	0	97	112	66	0	0
75≤θ<85	0	0	3	4	0	0
85≤θ<90	0	0	0	0	0	0

Table 5-4: Boulder count matrix for both the vertical mini-telescopes ($\Delta t \sim 27$ days)

Angle	Energy bins (MeV)					
(deg.)	10≤E≤20	20≤E<40	40≤E<60	60≤E<100	100≤E<170	170≤E<200
0≤θ<5	0	0	0	0	0	0
5≤θ<15	0	0	20	78	74	0
15≤θ<25	6	201	193	274	149	0
25≤θ<35	218	387	260	300	181	15
35≤θ<45	375	374	237	263	181	0
45≤θ<55	379	380	206	308	25	0
55≤θ<65	125	359	191	205	0	0
65≤θ<75	0	112	192	104	0	0
75≤θ<85	0	0	0	0	0	0
85≤θ<90	0	0	0	0	0	0

Table 5-5: Mt.Washington count matrix for the B vertical mini-telescope ($\Delta t \sim 8$ days)

Angle	Energy bins (MeV)					
(deg.)	10≤E≤20	20≤E<40	40≤E<60	60≤E<100	100≤E<170	170≤E<200
0≤θ<5	0	0	0	0	0	0
5≤θ<15	0	0	7	31	6	0
15≤θ<25	12	61	40	49	11	0
25≤θ<35	86	92	48	43	28	0
35≤θ<45	84	96	44	58	42	0
45≤θ<55	61	94	49	67	19	0
55≤θ<65	25	102	43	68	0	0
65≤θ<75	0	35	18	48	0	0
75≤θ<85	0	0	0	3	0	0
85≤θ<90	0	0	0	0	0	0

Table 5-6: Durham count matrix for both the vertical mini-telescopes ($\Delta t \sim$ 26 days)

Angle	Energy bins (MeV)					
(deg.)	10≤E≤20	20≤E<40	40≤E<60	60≤E<100	100≤E<170	170≤E<200
0≤θ<5	0	0	0	0	0	0
5≤θ<15	0	0	9	21	19	0
15≤θ<25	8	93	50	51	31	0
25≤θ<35	73	120	64	74	35	2
35≤θ<45	113	101	60	64	47	0
45≤θ<55	93	100	52	70	22	0
55≤θ<65	29	109	51	70	0	0
65≤θ<75	0	31	38	53	0	0
75≤θ<85	0	0	0	3	0	0
85≤θ<90	0	0	0	0	0	0

5.4 Flux Calculation Procedure

The telescope measurements give only the neutron count matrix as described in the above section. This count matrix C is the convolution of telescope's inherent response function R and the incident flux distribution F. The response of the telescope is not a delta function in energy or a delta function in angle, i.e. incident neutrons at a given energy and angle $F(E_i,\theta_j)$ give rise to counts in different energy and angle bins - $C(E_k,\theta_l)$, where E is the incident neutron energy and θ is the incident neutron zenith angle. Therefore, the neutron counts $C(E_k,\theta_l)$, measured at an energy E_k and at an angle θ_l is due to the contributions from all the other incident neutrons at different energies E_i and angles θ_j :

$$C(E_k,\theta_l) = \sum_{i,j} F(E_i,\theta_j) \cdot R(E_k,\theta_l ; E_i,\theta_j) \qquad (5.1)$$

where,

$C(E_k,\theta_l)$ The neutron counts measured at an energy E_k in an energy interval of ΔE and at an angle θ_l in a solid angle $d\Omega$ in time dt.

$F(E_i,\theta_j)$ The incident flux of neutrons with energy E_i in an energy interval of ΔE and at an angle θ_j in a solid angle $d\Omega$ in time dt on a surface area dA .

$R(E_k,\theta_l ;E_i,\theta_j)$ The Response of the telescope at an energy E_k and at an angle θ_l due to the neutrons of energy E_i incident at an angle θ_j on the telescope.

If the entire Response matrix is known, then it is theoretically possible to solve equations of type (5.1) for all the F_{ij} elements. This process is called *spectrum deconvolution* or *spectrum unfolding*. Two main problems arise in the unfolding process : (1) The response function is measured experimentally only for a few discrete energies and angles and; (2) due to the statistical nature of calibration and field measurements, uncertainties will propagate through the unfolding calculation and give rise to corresponding variances in the calculated energy spectrum. Unless a large number of counts are collected over the spectrum range of interest, these statistical uncertainties can result in large errors in the derived spectrum.

Due to the above mentioned uncertainties, an exact set of solutions F_{ij} cannot be obtained. Instead, approximate solutions are sought, which give a best estimate of the spectrum. Two methods are described below:

(a)

This method is based on finding a minimum in the weighted sum of residuals

$$\varepsilon^2 = \sum_{i,j} W_{ij}\left(C_{ij} - \sum_{k,l} R_{ijkl}\, F_{kl}\right)^2 \qquad (5.2)$$

where the weighting factors W_{ij} are often taken to be inversely proportional to the statistical variance of each data point. The indices i, k refer to the energy and the indices j, l refer to the angles. To reduce the effects of statistical uncertainties, some form of *data smoothing* is required, in which an average over a number of adjacent channels is taken, i.e. over an energy and over an angle interval. To avoid loss of energy and angular resolution, the

interval over which the smoothing is carried out must be less than the corresponding interval over which the response function changes significantly.

The flux of neutrons was assumed to be a power law in energy and having an angular dependence of the form $(\cos\theta)^n$:

$$\overline{F(E,\theta)} = \frac{F(E,\theta)}{d\Omega.\, dE.\, dt.\, dA} = F_0.\, E^{\alpha}.\, (\cos\theta)^n \qquad (5.3)$$

where F_o is the normalizing constant and $F(E,\theta)$ is the differential neutron flux at an energy E and at an angle θ. Both α and n can be varied for a minimum χ-square fitting.

(b)

The following method is based on finding an integrated Response function for the telescope in the total range of interest (both in energy and angle). It yields correct values for the flux only when the assumed incident spectrum agrees with the calculated spectrum, but the dependence on the input spectral shape is weak.

Using the Monte Carlo instrument model, the response of the telescope is predicted from an input spectrum of the form $E^{\alpha} \cos^{n}\theta$ in the ranges 10-200 MeV and 0°-90°. The incident flux as well as resultant simulated counts were binned in the same manner as the real data producing both an incident neutron and a count matrix. We define an "efficiency" quantity ε_{ij} to be the element by element ratio of the simulated events and the assumed incident neutron flux, i.e.

$$\varepsilon_{ij} = \frac{C_{ij}}{F_{ij}}.$$

This composite or integral "efficiency" can then be used as a multiplicative factor to convert the real counts C_{ij} into a real estimated flux F_{ij}. The resultant values F_{ij} are not strongly dependent upon the values of α and n, therefore allowing a rapid convergence between the assumed incident flux and the estimated flux in an iteration scheme. This method was

successfuly used by Ryan et al. (1979) and Ait-Oumar (1989) to calculate fluxes for atmospheric gamma rays and neutrons, respectively. We find the flux solution from this method to be much better behaved than those produced by the spectrum deconvolution method.

CHAPTER 6

RESULTS AND DISCUSSION

The ground level atmospheric neutron flux in the energy range of 10 to 170 MeV and in the zenith angle range from 15 to 45 degrees was evaluated using the count matrices and the integrated response function of the telescope as described in the previous chapters. Variations in the secondary cosmic ray intensity due to geomagnetic effects was discussed in chapter 1. One of the major geophysical effects on the secondary cosmic ray intensity is called the *barometric effect* or equivalently the altitude dependence of the cosmic ray intensity. The barometric coefficient or the e-folding depth of the atmosphere for neutrons is not entirely independent of the latitude coefficient (Dorman, 1987). Therefore, comparison of altitude variations in the neutron flux is performed over a small range of rigidity values. Similarly, the rigidity effect should be studied over a small range of altitudes. These criteria are satisfied for the four measurements discussed here.

6.1 Altitude Dependence

The barometric effect was initially believed to be pure absorption due to the amount of matter traversed by secondary cosmic rays with increasing atmospheric pressure. It was proposed that the atmospheric attenuation is affected by three factors: (1) absorption, (2) the decay of pions and muons and (3) the generation of new secondaries with increasing atmospheric pressure. In the first 100 g/cm^2 of the atmosphere i.e. above the Pfotzer maximum, the generation of secondaries dominates

absorption and the total cosmic ray flux grows with increasing depth. Below the Pfotzer maximum, at a depth of h g/cm^2, the vertical intensity I is given as :

$$I = I_0 \exp(- h/\lambda)$$

$$\beta = \frac{1}{I}\frac{\partial I}{\partial h} = -\frac{1}{\lambda},$$

where β is the barometric coefficient and λ is the e-folding depth for a given cosmic ray component.

For ground level neutrons of any energy the e-folding depth or the neutron attenuation coefficient was found by Hess et al. (1959) to be 155 g/cm^2 and by Tajima et al.(1967) to be 158.7 g/cm^2. For very high energies E ~ 230 GeV, the attenuation coefficient was found by Ashton et al. to be 127±15 g/cm^2. The attenuation length as calculated by Flückiger et al.(1977) was 128 g/cm^2. The barometric coefficient used by Morishita and Pomerantz (1987) for the neutron monitor located at south pole was -1.030 % / mmHg, which is equivalent to an e-folding depth of 129 g/cm^2. We have found from our measurements in the energy range of 10 to 170 MeV, the neutron attenuation length to be $\lambda = (127 \pm 32)$ g/cm^2 at a vertical cutoff rigidity (R_C) range from 2.90 to 2.97 GV and $\lambda = (119 \pm 25)$ g/cm^2 at 1.43 to 1.61 GV (see Fig. 6-1).

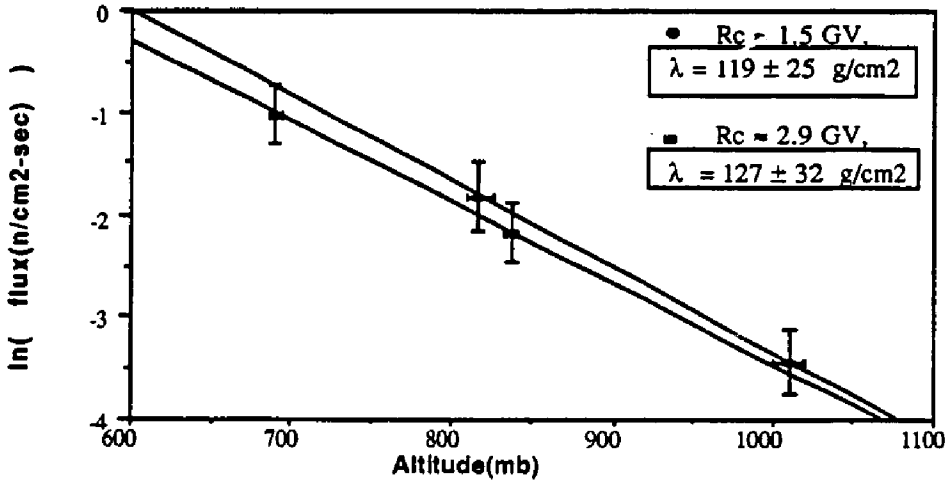

Fig.6-1: The altitude dependence of the neutron flux integrated over upper hemisphere and 10 -170 MeV.

6.2 Rigidity Dependence

Since there are no direct measurements of ground level neutron fluxes at different latitudes, we compare our data with neutron monitor data. Several atmospheric neutron flux measurements in the upper atmosphere (~ 5 mb) at different latitudes have been made (Jenkins et al.,1970; Preszler et al., 1974, 1976; Bhatt et al., 1983, 1986) with the results being used to normalize ground level neutron fluxes to that at $\lambda = 41^{o}$ N geomagnetic latitude (Preszler et al., 1974). We have found that the vertical cutoff rigidity correction factor is different (weaker) for ground level neutrons compared to that of upper atmospheric neutrons. This is to be expected as the most energetic primaries responsible for most high energy ground level neutrons are least affected by changes in rigidity. In Fig.6-2, the neutron monitor data of Moraal et al.(1989) over a wide range of rigidity is shown. The neutron monitor data are best fit by an expression: $N = N_0[1 - \exp(-\alpha R_C^{-k})]$ (where N is the counting rate at vertical cutoff rigidity R_C and N_0, α, k are regression coefficients (Moraal et al., 1989; Dorman et al., 1970), but it is clear that the rigidity dependence is weak below 10 GV. The upper atmosphere points are those of Bhatt et al.(1983,1986), Ait Ouamer et al.(1988) and Preszler et al.(1974, 1976). The ratio of total neutron fluxes at different latitudes to 0.4 GV (Koga et al., 1990) are also plotted in Fig. 6-2. The vertical cutoff rigidity can vary with time on the order of 14% in 30 years (Durham, New Hampshire) and these secular changes in the geomagnetic field are maximum in the Atlantic Ocean and contiguous land areas (Smart et al., 1987). We have used the 1985 geomagnetic survey values for our measurements but the rigidity values used for upper atmospheric measurements made at different times can have some uncertainity in them. Although, the latitude range of our data set is only 1.5 GV, we still observe a weak rigidity dependence (~ 21 %). Latitude correction using data from albedo neutrons (Ait-Ouamer et al., 1988) will give a change of ~ 36% in the same rigidity range. Ground level neutron flux measurements at locations of higher and lower vertical cutoff rigidity are

required to better determine the rigidity dependence. However, on the basis of our data and the neutron monitor data, we conclude that the latitude or the rigidity dependence for neutrons in the upper atmosphere is different from that for ground level neutrons, the rigidity dependence is weaker for the ground level neutrons.

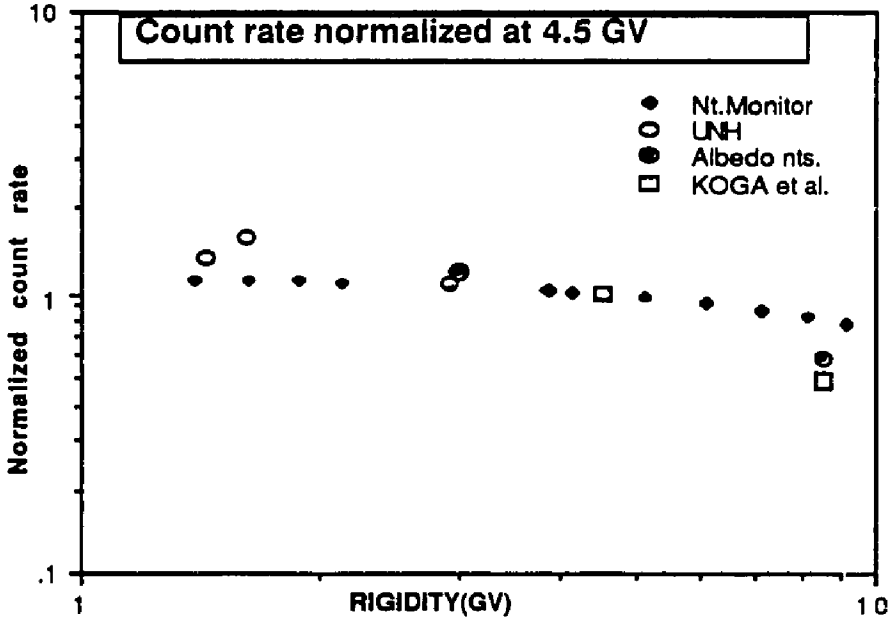

Fig.6-2: The latitude dependence of neutron count rate normalized at 4.5 GV. The points designated as Albedo nts.are those of Bhatt et al.(1983,1986), Ait Ouamer et al.(1988) and Preszler et al.(1974, 1976) for upper atmosphere.

6.3 Angular Distribution

Our results are restricted to the zenith angle range of 15 to 45 degrees. Our data show a $(\cos\theta)^{n}$ dependence with $n = 2.6 \pm 0.2$. In the energy range of 50 -100 MeV, Preszler et al.(1974) also found a $\cos^3\theta$ dependence for ground level neutrons at geomagnetic latitude of 48° N. The neutron flux as a function of $\cos\theta$ for all angle and energy bin is shown in Figures 6-3 to 6-6. The integrated spectra over the range 20 to 170 MeV are shown in Fig. 6-7.

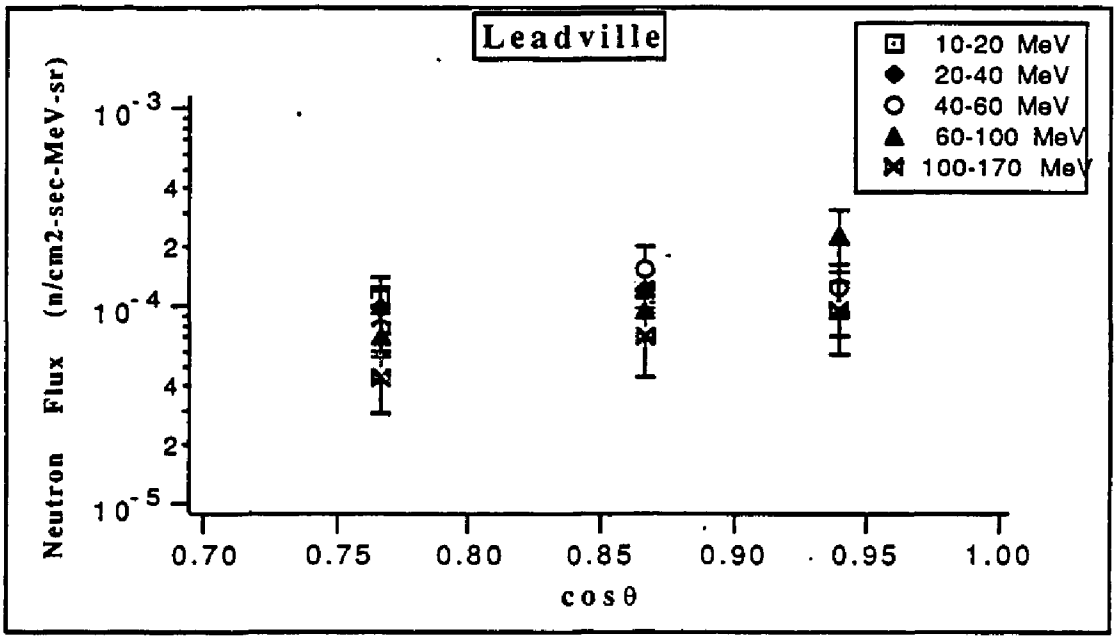

Fig. 6-3: The angular distribution of neutron flux at Leadville, Colorado.

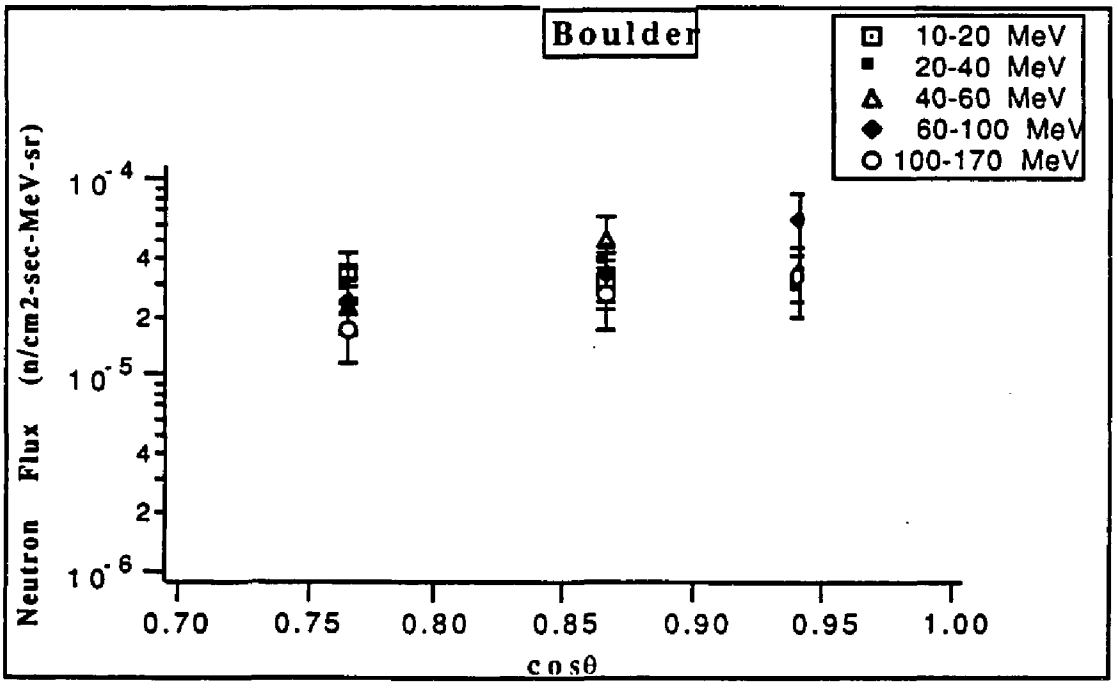

Fig. 6-4: The angular distribution of neutron flux at Boulder, Colorado.

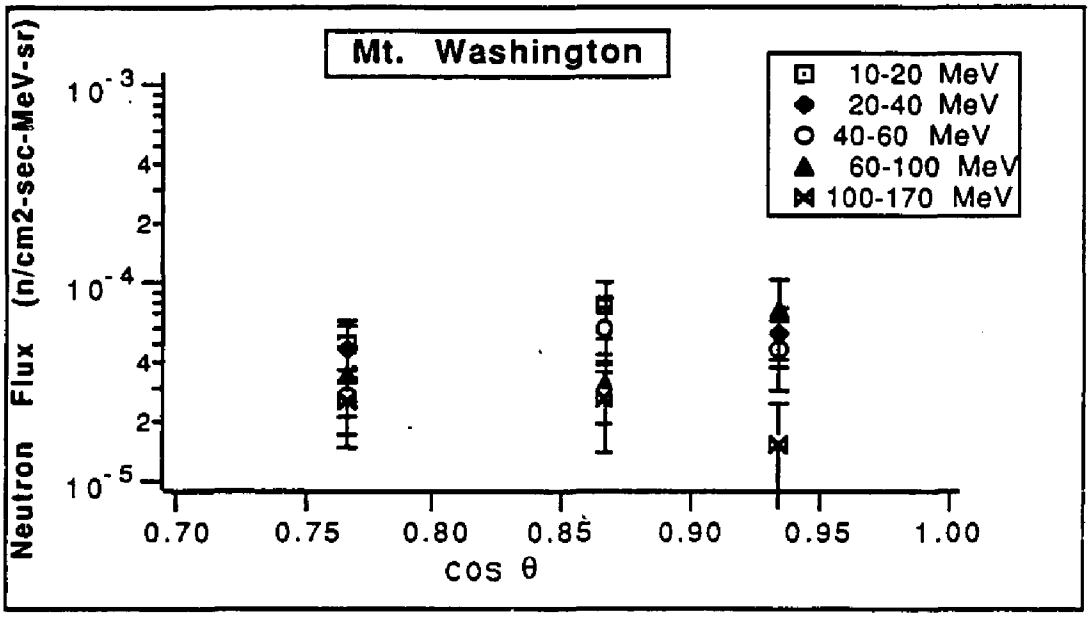

Fig. 6-5: The angular distribution of neutron flux at Mt. Washington, New Hampshire.

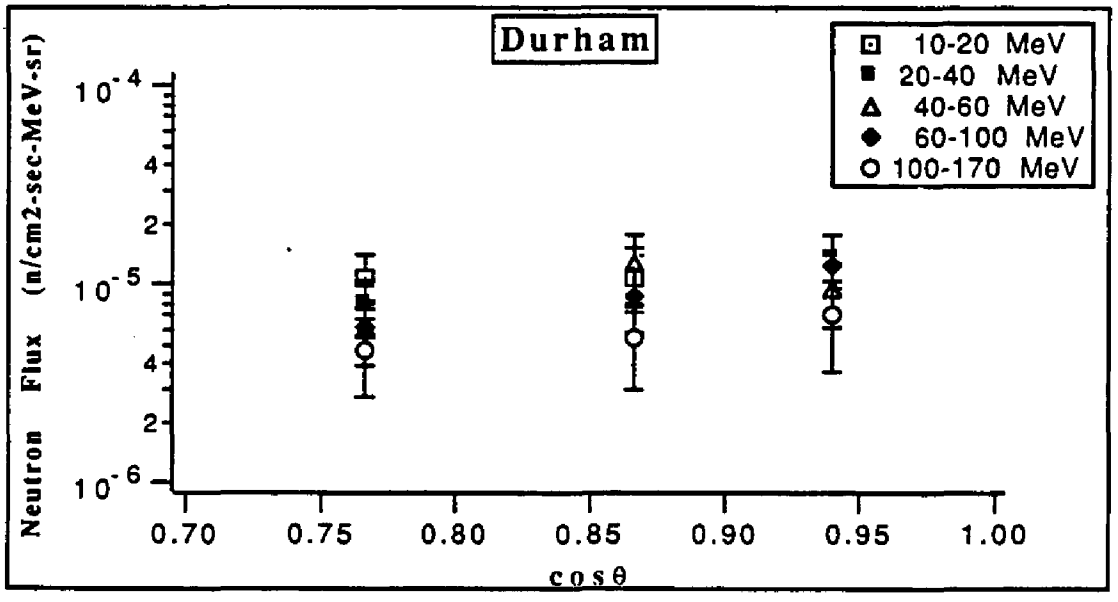

Fig.6-6: The angular distribution of Neutron flux at Durham, New Hampshire.

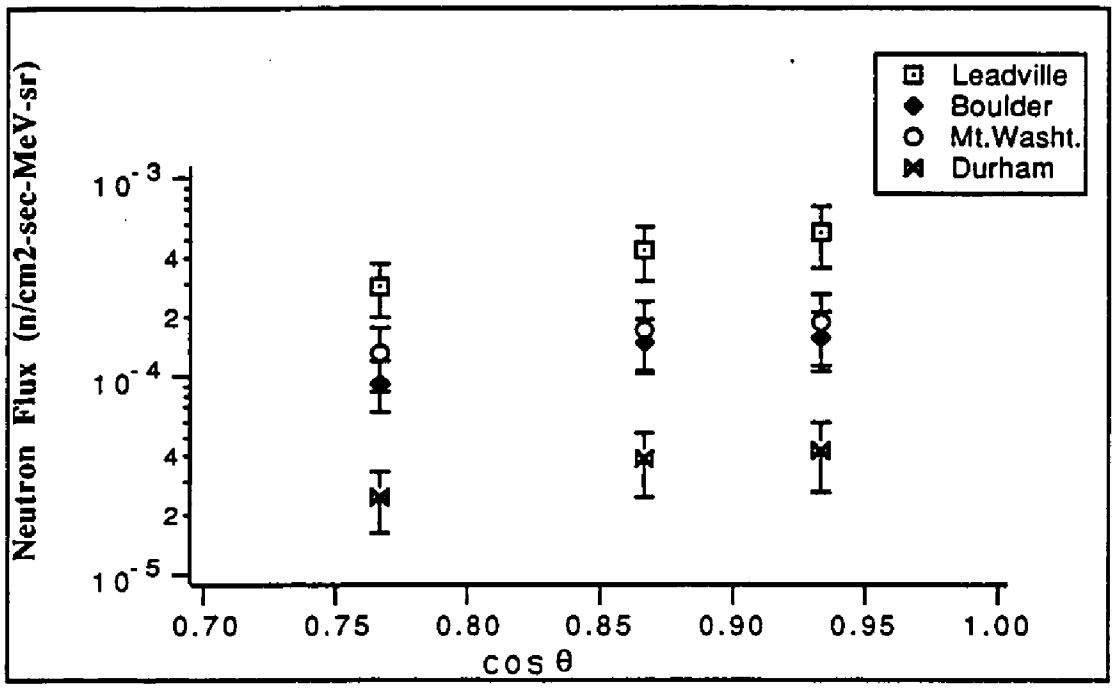

Fig6-7: The angular distribution of neutron flux integrated from 20-170 MeV for all observation sites.

6.4 Energy Distribution

The neutron energy distribution is shown in the Fig. 6-8 for Leadville, Fig. 6-9 for Boulder, Fig. 6-10 for Mt.Washington and in Fig. 6-11 for Durham.The integrated flux over 2π (using data from 25-45 degrees) for all observation sites as a function of neutron energy is shown in Fig. 6-12. The energy spectrum from 10 to 60 MeV tends to be flat at all locations and then slowly falls off as $E^{-\alpha}$ at higher energies with $\alpha = 0.6 \pm 0.1$. The one power law fit to all the data points from 10 to 170 MeV gives $\alpha = 0.28 \pm 0.10$ with 60% probability from χ^2 analysis, while the probability for two different slopes is 99%. As the statistics of the Mt.Washington data are not good due to problems during data collection (see chapter 5), we do not consider the slightly softer spectrum below 50 MeV to be significant. We have used our latitude corrections to normalize the Durham sea level 4π flux values to 41° N geomagnetic latitude (4.5 GV)

in order to compare with other measurements (see Fig. 6-13).

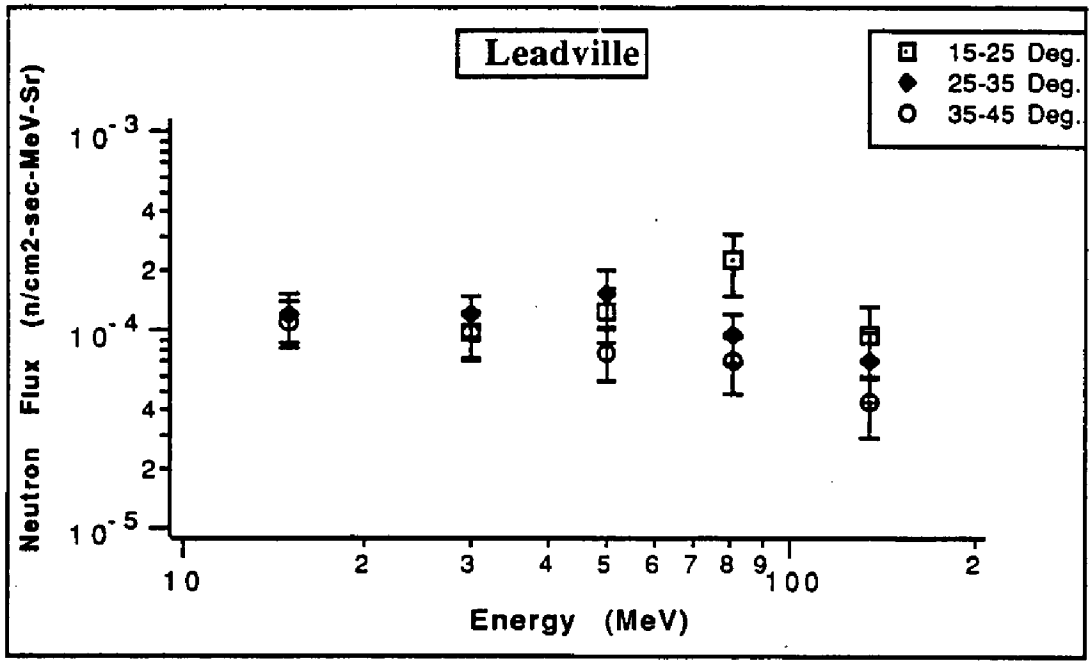

Fig. 6-8: The Differential flux of ground level neutrons at Leadville, Colorado.

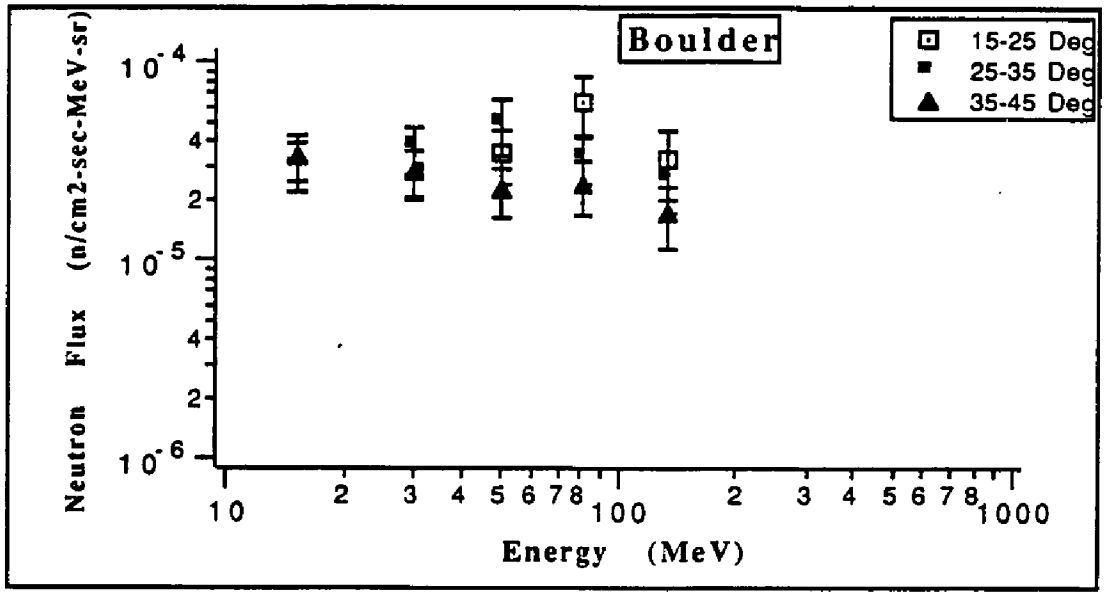

Fig. 6-9: The ground level neutron differential flux at Boulder, Colorado.

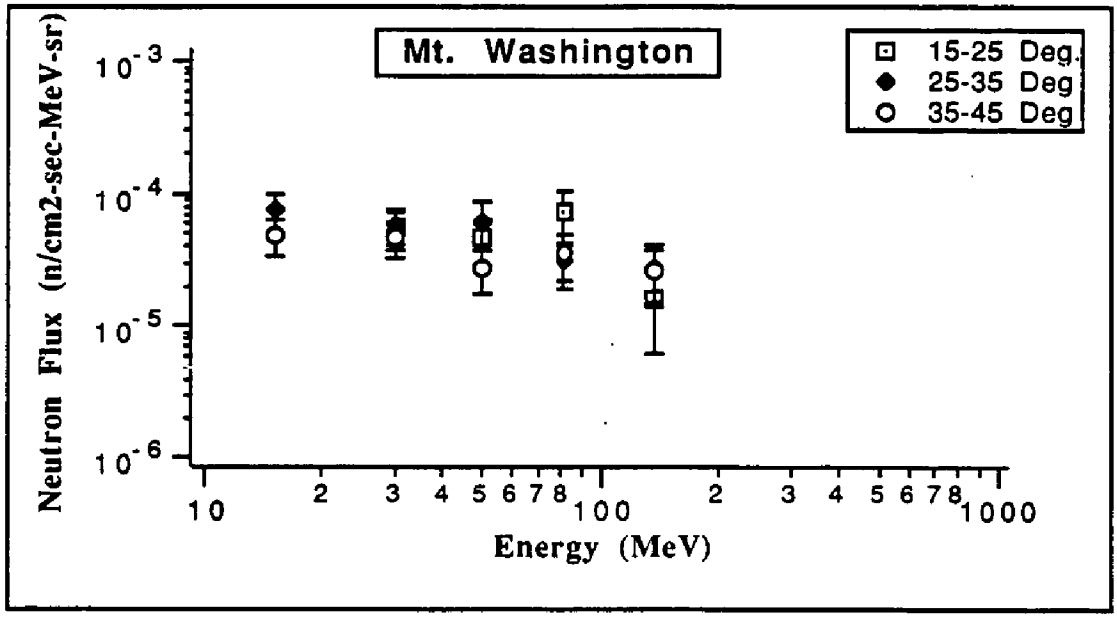

Fig. 6-10: The differential ground level neutron flux at Mt.Washington, New Hampshire

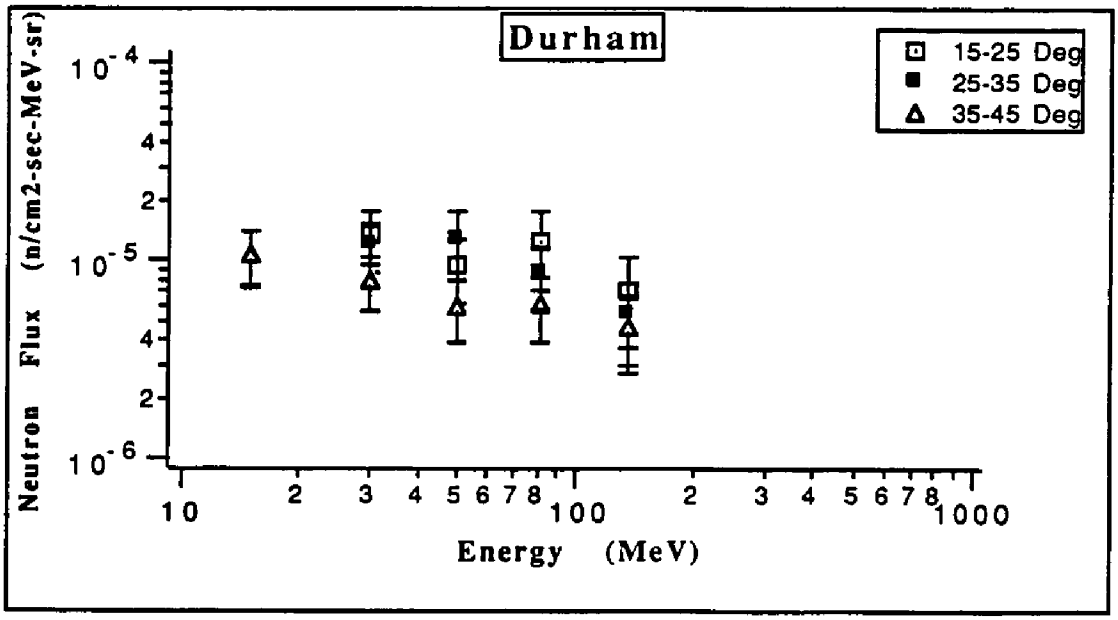

Fig. 6-11: The differential ground level neutron flux at Durham, New Hampshire.

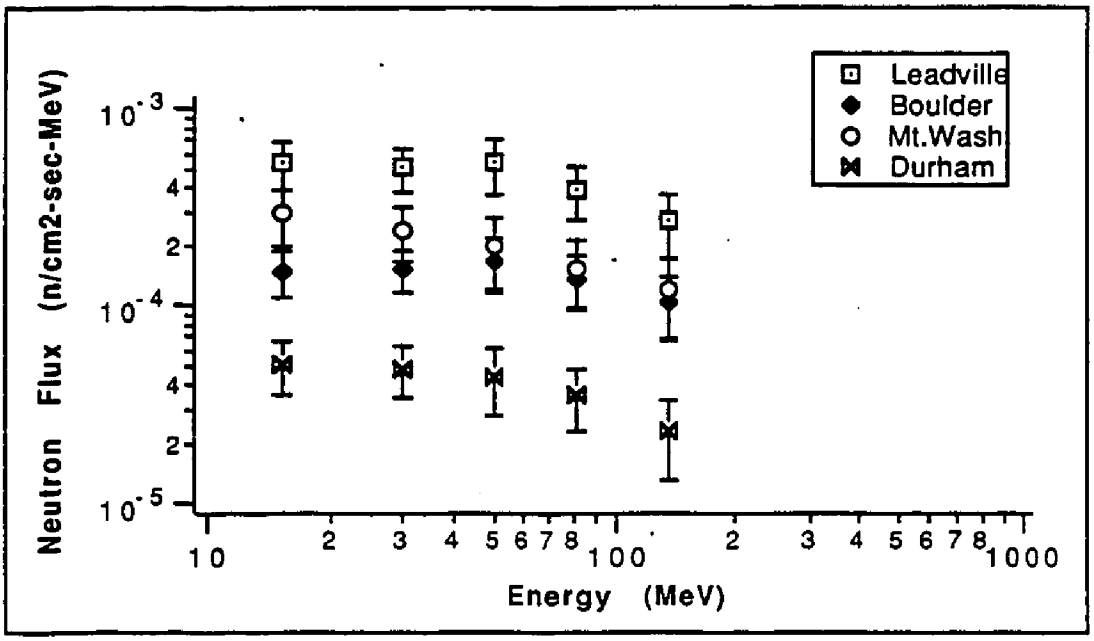

Fig. 6-12: The 2π integrated neutron flux at Leadville and Boulder in Colorado and at Mt. Washington and Durham in New Hampshire.

The flat spectrum in the 10 - 100 MeV energy range was first modeled by Armstrong et al.(1973) from their Monte Carlo calculations. The Preszler et al.(1974) measurements at Cape Girardeau, Missouri in 1972 also showed the presence of a flat spectrum for the 4π integrated flux (Fig. 6-13). All the values given in this graph have been normalized to 41°N geomagnetic latitude (R = 4.5 GV) using correction of Jenkins et al. (1970), which is ~0.67 for 48°N and ~2.0 for 25° N. As described in section 6.2, this correction best applies to neutrons in the upper atmosphere. The smaller rigidity dependence of ground level neutrons means that fluxes obtained from low latitudes (25°N) measurements are overestimated and those from high latitudes (48°N) are underestimated. We have plotted our sea level values using both latitude correction factors, i.e., Jenkins et al.(1970) and these measurements. Our data agree with Armstrong's calculated spectrum both in shape and in magnitude.

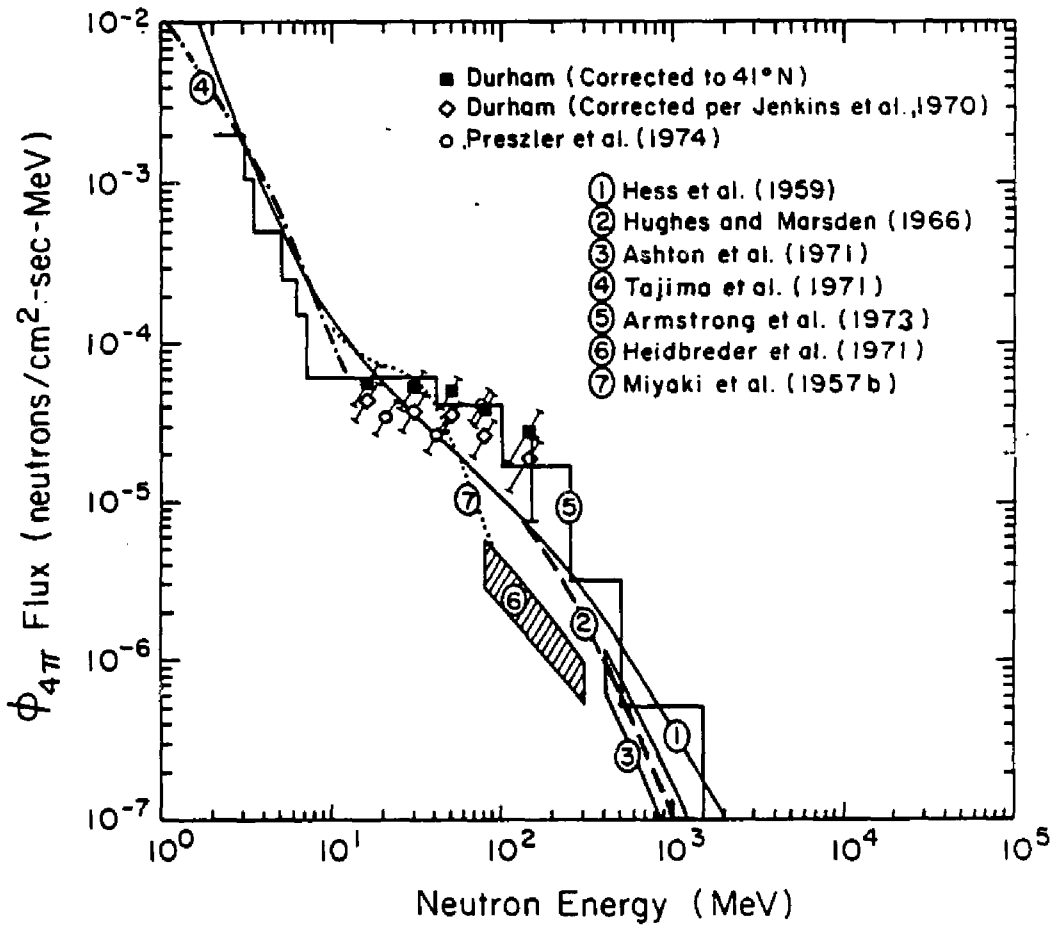

Fig. 6-13: The omnidirectional sea level neutron flux (from Preszler et al., 1974).

It is important that the shape of neutron spectrum departs from a diffusion spectrum of type E^{-1} in the energy range < 50 MeV. This is likely due to different processes which could either act as sinks or sources. In Fig. 6-14 we show the reciprocal of neutron mean free path as a function of energy. The plataeu from 5 MeV to 50 MeV is due to the high total cross-section of neutrons by nitrogen and oxygen nuclei in the atmosphere. The attenuation in this range is less than half the value at 1 MeV. This plus the fact that though the knock-on process there are many neutrons produced in the range of 10-50 MeV means that the measured atmospheric neutron spectrum in this range should be relatively hard.

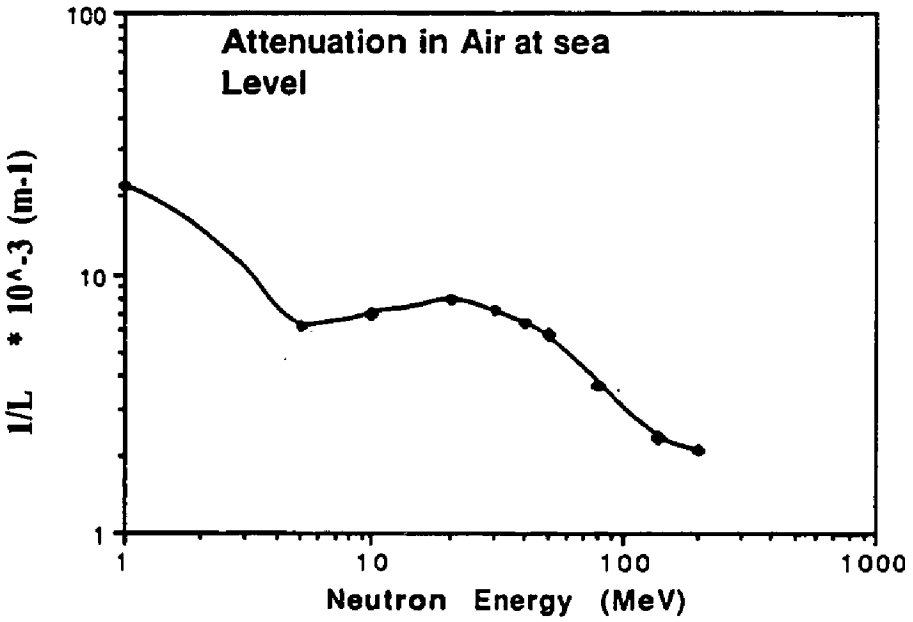

Fig. 6-14: Neutron Attenuation in air at sea level.

CONCLUSIONS

Ground level atmospheric neutrons in the energy range of 10 to 170 MeV and in the zenith angle range of 15 to 45 degree have been measured by the UNH double scatter telescope. Atmospheric neutrons are produced by the interaction of cosmic rays with the earth's atmosphere. The main production mechanism of neutrons in this energy range is by knock-on neutrons.

The measurements were made in 1987 at four different locations in U.S.A, at two different altitudes for two similar rigidity values: Leadville (691 mb) and Boulder (835 mb), Colorado at 2.97 - 2.90 GV; Mt.Washington (817 mb) and Durham (1010 mb), New Hampshire at 1.43 to 1.61 GV. Measurements were taken in a temperature controlled environment.

Only ~1-3% of raw data are good neutron events after applying all the restrictions for background reduction. The differential flux spectrum integrated over 20 - 170 MeV range for all sites shows a $\cos^n \theta$ dependence with $n = 2.6 \pm 0.2$. This agrees with measurements of Preszler et al. (1974). The energy distribution for differential flux as well as for integrated flux over upper hemisphere shows a flat distribution from 10 to 60 MeV and falls of as $E^{-0.6\pm0.1}$ from 60 to 170 MeV. The neuton count rate from the upper hemisphere integrated from 10 - 170 MeV for Leadville is $0.36 \pm 29\%$ neutrons/cm^2-sec; for Boulder, $0.11 \pm 29\%$; for Mt. Washington, $0.16 \pm 35\%$ and for Durham, $0.03 \pm 31\%$. The average altitude attenuation coefficient or the e-folding depth from all the locations was found to be $\lambda = (122 \pm 20)$ g/cm^2. We found that the latitude correction of Jenkins et al.(1970) used for upper atmospheric neutrons is larger than that for ground level neutrons. In our rigidity range of 1.43 GV to 2.97 GV, the difference between the two corrections represents a reduction in the fluxes by ~ 30% when correcting from 54.6° N to 41° N.

Measurements over a wider latitude range at similar atmospheric depths are needed to establish a good latitude correction factor for ground level neutrons.

We found the UNH neutron double scatter telescope to be quite rugged and reliable after being dismantled and shipped to many different locations. Because of these features it can be used to extend the survey reported here.

LIST OF REFERENCES

Ait-Ouamer, F., A. D. Zych and R. S. White, Atmospheric neutrons at 8.5 GV cutoff in the southern hemisphere, *J. Geophys. Res., 93*, 2499, 1988.

Allkofer, O. C., and P. K. F. Grieder, Cosmic Rays on Earth, *Physics Data, Nr.25-1,* Fachinformationszentrum Energie . Physik . Mathematik GmbH, 1984.

Anghinolfi , M., G. Ricco., P. Corvisiero, and F. Masulli, The response function of organic scintillators to fast neutrons, *Nucl. Instr. and Meth., 165*, 217, 1979.

Armstrong, T. W., K. C. Chandler, and J. Barish, Calculations of neutron flux spectra induced in the earth's atmosphere by galactic cosmic rays, *J. Geophys. Res., 78*, 2715, 1973.

Ashton, F., N. I. Smith, J. King, E.A. Mamidzhanian, Energy spectrum of neutrons in the sea level cosmic radiation, (*Proc. 11th Int. Conf. on Cosmic Rays, Budapest,1969) Acta Physica Acad. Sci. Hung., 29, suppl. 3*, 25, 1970.

Ashton, F., H. J. Edwards, and G. N. Kelly, The spectrum of cosmic ray neutrons at sea level in the range 0.4-1.2 GeV, *Proc. Phys. Soc. London Gen., 4*, 352, 1971.

Beckurts, K. H., and K. Wirtz, Neutron Physics, *Springer-Verlag, New York Inc.*, 1964.

Bhatt, V. L., Neutron high energy spectra at 5 mbar near the geomagnetic equator, *J. Geophys. Res., 81*, 4603, 1976.

Bhatt, V.L., Neutron high energy spectra at seven different depths in the atmosphere from 0 to 40 mbar near the geomagnetic equator, *J. Geophys. Res., 88*, 4941, 1983.

Bhatt, V.L., Altitude and Latitude effects of atmospheric neutrons, *J. Geophys. Res., 91*, 8971, 1986.

Biermann, L.V., O. Haxel, and A. Schluter, Neutral ultrastrahlung von der son, *Z. Naturforschg., 6a*, 47, 1951.

Birks, J.B., The theory and practice of scintillation counting, *Pergamon Press*, 1964.

Bózoki, G., E. Fenyves, N. Ahababyan, B. Betev, Ch. Christov, J. Georgiev, and S. Kavlakov, Inelastic n-p cross sections at about 100 and 130 GeV, (*Proc. 11th Int. Conf. on Cosmic Rays , Budapest, 1969*) *Acta Physica Acad. Sci. Hung., 29, Suppl. 3*, 201, 1970.

Brooke, G., and A. W. Wolfendale, The momentum spectrum of cosmic ray protons

near sea level in the momentum range 0.6 - 150 GeV/c, *Proc. Phys. Soc. London, 83,* 843, 1964.

Burbidge, G.R., The extra-galactic contribution to the primary cosmic-ray flux, *Phil. Trans. Roy. Soc. London, A277,* 481, 1974.

Burchuladze, A. A., S. V. Pagava, P. Povinec, G. I. Togonidze, and S. Usacev, Radiocarbon variations with the 11-year solar cycle during the last century, *Nature, 287,* 320 , 1980.

Cecil, R. A., B. D. Anderson, and R. Madey, Improved predictions of neutron detection efficiency for hydrocarbon scintillators from 1 MeV to about 300 MeV, *Nucl. Instr.and Meth., 161,* 439, 1979.

Cerineo, M., K. Ilakovac, I. Slaus, and P. Tomas, Capture of 14.4 MeV neutrons by protons and deuterons, *Phys. Rev., 124,* 1947, 1961.

Cokinos, D., and E. Melkonian, Measurement of the 2200 m/sec neutron-proton capture cross section, *Phys. Rev.(C), 15,* 1636, 1977.

Chupp, E. L., D. J. Forrest, J. M. Ryan, J. Heslin, C. Reppin, K. Pinkau, G. Kanbach, E. Rieger, and G. H. Share, A direct observation of solar neutrons following the 0118 UT flare on 1980 june 21, *Ap. J.(Letters), 263,* L95, 1982.

Chupp, E. L., Forrest, D. J., Share, G. H. Kanbach, G. Debrunner, and E. Fluckiger, Solar Neutrons from the impulsive flare on 1982 june 3 at 1143 UT, *Proc. 18th Int. Cosmic Ray Conf.(Bangalore), 10,* 334, 1983.

Dorman, L. I., S. G. Fedchenko, L. V. Granitsky, and G. A. Rische, Coupling and barometer coefficients for measurements of cosmic ray variations at altitudes of 260-400 mb, *Acta Phys. Acad. Sci. Hung., 29(suppl.2),* 233, 1970.

Dorman, L. I., Geomagnetic and Atmospheric effects in primary and secondary cosmic rays. Cosmogeneous nuclei, *Proc. 20th.Int. Cosmic Ray Conf.(Moscow), 8,* 186, 1987.

Flückiger, E., Angewandte Physik und Andere Domänen, Monte-carlo-simulation der nukleonenspektren der kosmischen strahlung in der atmosphäre, *Helv. Phys. Acta, 49,* 743, 1976.

Flückiger, E., Theoretical spectra of cosmic ray neutrons in the atmosphere for the energy range 50 MeV $\leq$ E $\leq$ 100 GeV, *Proc. 15th Cosmic Ray Conf. (Plovdiv), 4,* 144, 1977.

Forbush, S. E., On world-wide changes in cosmic-ray intensity, *Phys. Rev., 54,* 975, 1938.

Fraunfelder, H.,and E. M. Henley, Subatomic Physics, *Prentice Hall Inc., New Jersey,* 1974.

Gai, M., S. L. Rugari, R. H. France, B. J. Lund, Z. Zhao, A. J. Davenport, H. S. Isaacs,and K. G. Lynn, Upper limits on neutron and γ-ray emission from cold fusion, *Nature, 340,* 29, 1989.

Galli, M., G. C. Castagnoli, M. R. Attolini, S. Cecchini, T. Nanni, G. E. Kocharov, V. A. Vasiliev, and A. N. Konstantinov, The 20 year cycle of solar activity in ^{14}C and ^{10}B (Before and during Maunder minimum), *Proc. 20th Int. Cosmic Ray Conf. (Moscow), 4*, 284, 1987.

Goodman, C.D., The (p,n) reaction at intermediate energies , *The (p,n) reaction and the nucleon - nucleon force, edited by C. D. Goodman, Plenum Press, NY*, 1980.

Heidbreder, E., K. Pinkau, C. Reppin, and V. Schönfelder, Measurements of the distribution in energy and angle of high-energy neutrons in the lower atmosphere, *J. Geophys. Res., 76*, 2905, 1971.

Hess, W. N., H. W. Patterson, R. Wallace, and E. L. Chupp, Cosmic-ray neutron energy spectrum, *Phys. Rev., 116*, 445, 1959.

Hess, W. N., E. H. Canfield, and R. E. Lingenfelter, Cosmic ray neutron demography, *J. Geophys. Res., 66*, 665, 1961.

Hughes, E. B., and P. L. Marsden, Response of a standard IGY neutron monitor, *J. Geophys. Res., 71*, 1435, 1966.

Jenkins, R. W., J. A. Lockwood, S. O. Ifedili, and E. L. Chupp, Latitude and altitude dependence of the cosmic ray albedo neutron flux, *J. Geophys. Res., 75*, 4197, 1970.

Jory, F. S., Influence of geomagnetic quadrupole fields upon cosmic-ray intensity, *Phys. Rev., 102*, 1167, 1956.

Kanbach, G., C. Reppin, and V. Schönfelder, Support for Crand theory from measurements of Earth albedo neutrons between 70 and 250 MeV, *J. Geophys. Res., 79*, 5159, 1974.

Knoll, G. F., Radiation Detection and Measurement, *2nd Ed., John Wiley & Sons, Inc, New York*, 1989.

Koga, R., S. D. Pinkerton, G. M. Frye, Jr., A. Owens, B. V. Denehy, O. Mace, and J. Thomas, Comparisons of atmospheric neutrons measured at 4.5 and 8.5 GV, *Proc. 21st Int. Cosmic Ray Conf. (Adelaide), 7*, 100, 1990.

Light, E. S., M. Merker, H. J. Verschell, R. B. Mendell, and S. A. Korff, Time dependent worldwide distribution of atmospheric neutrons and of their products, 2. Calculation, *J. Geophys. Res., 78*, 2741, 1973.

Lingenfelter, R. E., and R. Ramaty, High energy nuclear reactions in solar flares, *High Energy Nuclear Reactions in Astrophysics, Ed. by B.S.P. Shen, W.A. Benjamin Inc., New York*, 1967.

Lockwood, J. A., and A. R. Calawa, On the barometric pressure coefficient for cosmic ray neutrons, *J. Atm. and Terres. Phys., 11*, 23, 1957.

Lockwood, J. A., Neutron Measurements in space, *Space Sci. Rev., 14*, 663, 1973.

Lockwood, J. A., C. Chen, L. A. Friling, and R. N. Onge, Energy spectrum and flux of high energy neutrons at balloon altitudes, *J. Geophys. Res., 81*, 6211, 1976.

Lockwood, J. A., L. Hsieh, L. Friling, C. Chen, and D. Swartz, Atmospheric neutron and gamma ray fluxes and energy spectra, *J. Geophys. Res., 84*, 1402, 1979.

Longair, M. S., High Energy Astrophysics, *Cambridge University Press, New York,* 1981.

Madey, R., F. M. Waterman, A. R. Baldwin, J. N. Knudson, J. D. Carlson, and J. Rapaport, The response of NE-228A, NE-228, and NE-102 scintillators to protons from 2.43 to 19.55 MeV, *Nucl. Instr. and Meth., 151*, 445, 1978.

Marion, J. B., and J. L. Fowler, Fast Neutron Physics , Part II, *Interscience Publishers, Copyright by John Wiley & Sons Inc.*, 1963.

McLane, V., C. L. Dunford, and P. F. Rose, Neutron Cross Section Curves, Vol. 2, *Copyright by Academic Press, Inc., San Diego,* 1988.

Miyake, S., K. Hinotani, and K. Nunogaki, Intensity and energy spectrum of fast neutrons in cosmic radiation, *J. Phys. Soc. Jap., 12*, 113, 1957*a*.

Miyake, S., K. Hinotani, I. Katasumata, and T. Kaneko, Cosmic ray nuclear interactions in nitrogen gas, *J. Phys. Soc. Jap., 12*, 845, 1957*b*.

Moraal, H., M. S. Potgieter, and P. H. Stoker, Neutron Monitor Latitude Survey of cosmic ray intensity during the 1986/1987 solar minimum, *J. Geophys. Res., 94*, 1459, 1989.

Nakayama, K., E. F. Pessoa, and R. A. Douglas, A modified version of the Monte carlo computer code for calculating neutron detection efficiencies, *Nucl. Instr. and Meth.*, 190, 555, 1981.

O'Gorman, T. J., A Monte Carlo Code for calculating neutron telescope efficiencies, (private communication), 1990.

Phillips, F. M., B. D. Leavy, N. O. Jannik, D. Elmore, and P. W. Kubik, The accumulation of cosmogenic chlorine-36 in rocks: a method for surface exposure dating, *Science, 231*, 41, 1986.

Preszler, A. M., G. M. Simnett, and R. S. White, Earth albedo neutrons from 10 to 100 MeV, *Phys. Rev. Lett., 28*, 982, 1972.

Preszler, A. M., G. M. Simnett, and R. S. White, Angular distributions and altitude dependence of atmospheric neutrons from 10 to 100 MeV, *J. Geophys. Res., 79*, 17, 1974.

Preszler, A. M., S. Moon, and R. S. White, Atmospheric neutrons, *J. Geophys. Res., 81*, 4715, 1976.

Rapaport, J., C. C. Foster, L. D. Goodman, L. A. Goulding, L. N. Taddeucci, D. T. Horen, B. R. Sugarbaker, C. Gaarde, J. Larson, J. A. Kar, F. Petrovich, and

M. J. Threapleton, (p,n) reaction on Li isotopes from protons of energy 60 to 200 MeV, (to be published), 1990.

Rindi, A., C. B. Lim, and T. S. Cinotti, (n,p) elastic scattering: A fitting expression for the differential cross sections in the energy range between 22.5 and 400 MeV, *UCRL- 20295, UC-34 Physics, TID-4500 (57th Ed.)*, 1970.

Rochester, G. D., and K. E. Turver, Cosmic rays of ultra-high energy, *Contemp. Phys., 22*, 425, 1981.

Rumbaugh, L. H., and G. L. Locher, Neutrons and other heavy particles in cosmic radiation of the stratosphere, *Phys. Rev., 49*, 855, 1936.

Simpson, J. A., Neutrons produced in the atmosphere by the cosmic radiations, *Phys. Rev., 83*, 1175, 1951.

Simpson, J.A., *Semaine d'Etude sur le Probleme du rayonment cosmique dans l'espace interplanetaire (Vatican: Pontifica Academia Scientiarium)*, 323, 1963.

Simpson, J.A., Introduction to the galactic cosmic radiation, *Composition and Origin of Cosmic Rays, Ed. M. M. Shapiro, NATO ASI Series*, 1982.

Simpson, J.A., Elemental and Isotopic Composition of the galactic cosmic rays, *Ann. Rev. Nucl. and Particle Phys. (Annual Reviews, Inc., Palo Alto, Calif.), Vol.33*, 1983.

Singer, S. F., Radiation belt and trapped cosmic ray albedo, *Phys. Rev. Lett., 1*, 181, 1958.

Smart, D. F., M. A. Shea, and L. C. Gentile, Vertical cutoff rigidities calculated using the estimated 1985 geomagnetic field coefficients, *Proc. 20th Int. Cosmic Ray Conf.(Moscow), 4*, 204, 1987.

Stanton, N. R., Ohio State University, COO-1545-92, 1971.

Tajima, E., M. Aduchi, T. Doke, S. Kubota, and M. Tsukuda, Spectrum of cosmic ray produced neutrons, *J. Phys. Soc. Jap., 22*, 355, 1967.

Toptygin, I. N., Cosmic Rays in interplanetary magnetic fields, *D.Reidel Publishing Company, Dordrecht, Holland,(Kluwer Academic Publishers, MA, U.S.A)*, 1985.

Webber, W. R., Lockwood, J. A., Characterisitcs of the 22-year modulation of cosmic rays as seen by neutron monitors, *J. Geophys. Res., 93*, 8735, 1988.

White, R.S., High-energy proton radiation belt, *Rev. Geophys., 11*, 595, 1973.

Wolfendale A.W., The Primary radiation: a brief review, *in Cosmic rays at ground level, Ed. A. W. Wolfendale, Published by The Institute of Physics, London, and by the American Institute of Physics, New York*, 1973.

Ziegler, J. F., and W. A. Lanford, Effect of cosmic rays on computer memories, *Science, 206*, 776, 1979.

Ziegler, J. F., and W. A. Lanford, The effect of sea level cosmic rays on electronic devices, *J. Appl. Phys., 52,* 4305, 1981*a*.

Ziegler, J. F., The background in detectors caused by sea level cosmic rays, *Nucl. Instr. and Meth., 191*, 419, 1981*b*.

Ziegler, J. F., The effect of concrete shielding on cosmic ray induced soft fails in electronic systems, *IEEE Trans. on Electron Devices, 28,* 560, 1981*c*.